Modeling and Processing Near-Surface Seismic Scattering in Multicomponent Data: An Approach Based on Elastic Wave Modeling and Polarization Filtering

Ivan Javier Sánchez Galvis

This dissertation is submited for the degree of *Doctor en Ingeniería*

Advisor: PhD. Daniel Alfonso Sierra Bueno

Titular Professor, Universidad Industrial de Santander.

Advisor: PhD. William Mauricio Agudelo Zambrano

Senior Geophysicist, ECOPETROL S.A.

Universidad Industrial de Santander

Facultad de Ingenierías Fisicomecánicas

Escuela de Ingenierías Eléctrica, Electrónica y de Telecomunicaciones

Bucaramanga

2024

Dedicatoria

Para mi esposa Mayra:

"Porque tu estima sobrepasa largamente a la de las piedras preciosas. Fuerza y honor son tu vestidura." Proverbios 31:10 y 25.

y para mi hijo Felipe:

"He aquí, herencia de Jehová son los hijos; cosa de estima el fruto del vientre. Como saetas en mano del valiente, así son los hijos habidos en la juventud." Salmos 127:3-4

Los amo profundamente.

Acknowledgments

I am deeply grateful to my advisors, Professor Daniel Sierra and PhD. William Agudelo, for their dedication in refining each of the ideas and for guiding me in every decision throughout this work.

I extend my gratitude to my friends and colleagues at UIS, especially Professor Carlos Niño and Jheyston Serrano. I also appreciate the collaboration of the Master's students I worked with, Anderson Páez and Holguer Quintero.

A special thank you goes to Professor Daniel Trad, who supervised my internship at the University of Calgary. His recommendations were highly valuable in advancing my work in GPU programming, both for elastic modeling and the Radon transform.

I am also thankful for the friendships I formed at CREWES, particularly Ziguang Su, Mariana Lume, and Paloma Fontes, who made my stay in Canada incredibly welcoming.

I also wish to express my sincere appreciation to each of the thesis evaluators. Their reviews and recommendations improved the quality of this research.

Lastly, I want to mention that this work was carried out within the framework of the Agreement *"Acta No. 27 del Convenio de Cooperación Tecnológica 5222395"* between Universidad Industrial de Santander and Ecopetrol S.A.- Centro de Innovación y Tecnología. The funding for the thesis development was made possible by Minciencias. Additionally, the funding for the research internship in CREWES-University of Calgary was provided by the Emerging Leaders in the Americas Program (ELAP) from Global Affairs Canada.

Table of Contents

List of Figures

List of Tables

Resumen

Título: Modelado y Procesamiento de Dispersión Sísmica Cercana a la Superficie en Datos Multicomponente: Un Enfoque Basado en el Modelado de Ondas Elásticas y Filtrado de Polarización. [*]

Autor: Ivan Javier Sánchez Galvis [**]

Palabras Clave: Cercano a la superficie, Modelado de ondas elásticas, Dispersión sísmica, Datos multicomponentes, Filtro de polarización, Autoencoder.

Descripción: Esta tesis presenta un conjunto de estrategias para modelar y procesar el ruido causado por la dispersión sísmica cercana a la superficie (NSS, *Near-surface Seismic Scattering*) en datos sísmicos multicomponente. Para lograr esto, se implementó un enfoque sistemático que incluyó el modelado numérico de la propagación de ondas elásticas 3D en medios heterogéneos cercanos a la superficie con topografías irregulares que emulan escenarios del mundo real. Para mitigar las complejidades computacionales y mejorar la precisión del modelado, se desarrolló un solucionador de ondas elásticas 3D acelerado por GPU. Utilizando dicho solucionador, se introdujo una estrategia para simular la separación NSS y comprender mejor el ruido sísmico terrestre y contribuir al avance de tal ruido. Se creó un filtro de polarización multiestación para la separación de tipos de ondas, mejorando la calidad de los datos sísmicos de tres componentes (3C) submuestreados, especialmente en presencia del ruido NSS. Finalmente, se aplicaron técnicas de aprendizaje automático para la atenuación automática de NSS, lo que mejoró la calidad de los datos sísmicos. El rendimiento de estas estrategias se probó a través de varios experimentos con datos reales y sintéticos, conduciendo a un progreso significativo en

---

[*] Tesis de Doctorado

[**] Facultad de Ingenierías Físico-Mecánicas. Escuela de Ingenierías Eléctrica, Electrónica y de Telecomunicaciones. Director: Daniel Alfonso Sierra Bueno, Doctor en Ingeniería Biomédica.
Codirector: William Mauricio Agudelo Zambrano, Doctor en Geofísica.

la atenuación del ruido NSS en datos sísmicos terrestres.

Abstract

Title: Modeling and Processing Near-Surface Seismic Scattering in Multicomponent Data: An Approach Based on Elastic Wave Modeling and Polarization Filtering [*]

Autor: Ivan Javier Sánchez Galvis [**]

Keywords: Near-surface, Elastic wave modeling, Seismic scattering, Multicomponent data, Polarization filter, Autoencoder.

Description: This thesis presents a set of strategies for modeling and processing noise caused by near-surface seismic scattering (NSS) in multicomponent seismic data. To achieve this, a systematic approach was implemented which included numerical modeling of 3D elastic wave propagation in heterogeneous near-surface media with irregular topographies emulating real-world settings. To address computational complexities and improve modeling accuracy, a GPU-accelerated 3D elastic wave solver was developed. Using such solver, a strategy for simulating NSS separation was introduced, leading to a better understanding of land seismic noise which contributes to the advancement of near-surface noise attenuation techniques. A multi-station polarization filter was created to improve wave type separation, enhancing undersampled three-component (3C) seismic data quality, especially in the presence of NSS noise. Finally, machine learning techniques were applied for automatic NSS attenuation leading to significant noise reduction and seismic data quality enhancement. The performance of these strategies was tested through various experiments with real and synthetic data, conducting to significant progress in attenuating NSS noise in land seismic data.

---

[*] Doctoral Thesis

[**] Facultad de Ingenierías Físico-Mecánicas. Escuela de Ingenierías Eléctrica, Electrónica y telecomunicaciones. Director: Daniel Alfonso Sierra Bueno, Doctor en Ingeniería Biomédica.
Codirector: William Mauricio Agudelo Zambrano, Doctor en Geofísica.

Introduction

Seismic imaging of complex structures in mountainous areas poses a significant challenge in land seismic exploration. The scattered waves, generated by a heterogeneous near-surface and rough topography, considerably interfere with the phase and amplitude of the recorded signal. This obscures the body wave reflections from deep structures Regone et al. (2017). In seismic reflection surveying, these scattered waves are treated as coherent noise, as they only contain information about the shallow structure that the model used for interpreting the data does not include. Consequently, seismic migration and inversion can be substantially affected if this Near-surface Seismic Scattering (NSS) is not properly removed during the filtering stage.

In complex acquisition areas such as foothills, the upcoming body wave from deeper structures is scattered by near-surface heterogeneities, decreasing the quality of the signal carrying information of interest. Scattering also impacts Rayleigh waves, resulting in a high-energy ground roll cone that masks the weaker body wave reflections.

To illustrate this, Figure 1 presents three-shot gathers acquired in a Foothill region. The shot gather from the flat area exhibits Rayleigh waves with a uniform behavior within a certain velocity range, which can be effectively removed using $f-k$ filtering. However, the other two shot gathers from the mountainous region show most of the energy trapped and scattered in the near-surface, making body-wave reflections difficult to observe. In these circumstances, traditional filtering methods fail to accurately eliminate NSS noise from seismic

shot gathers due to frequency overlap with reflections.

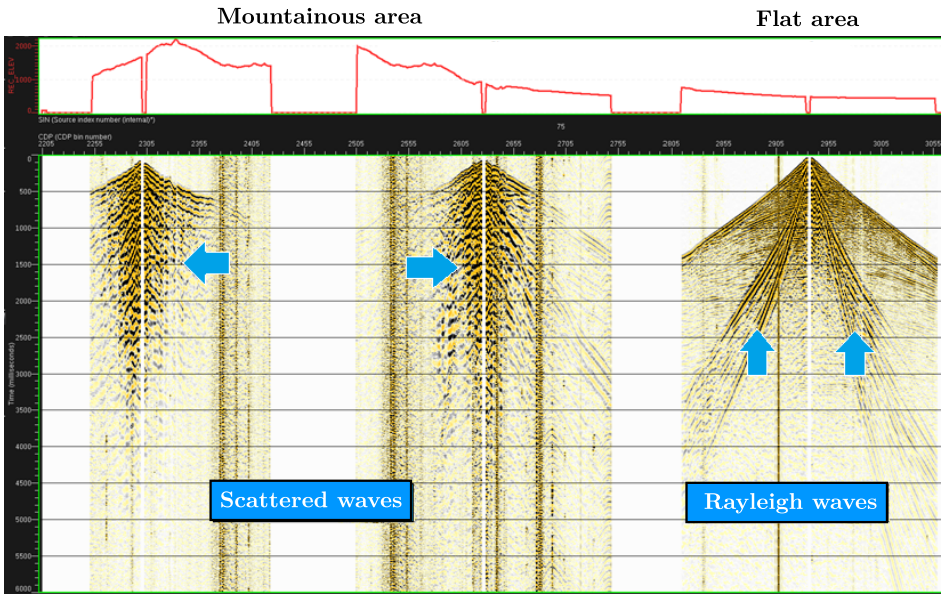

Figure 1. Scattered waves in foothills acquisition area. Courtesy of Ecopetrol S.A.

Given that frequency information is insufficient to separate scattering noise, additional information is required. Multicomponent data offer the advantage of utilizing polarization information to distinguish between wave types (Bale et al., 2013). Such polarization and multicomponent data can be used to identify new domains for facilitating the separation of the NSS noise and the signal. As an example, the vectorial information can be incorporated into the filtering process through the calculation of polarization attributes (Sánchez-Galvis et al., 2016). However, it is crucial that any representation of the multicomponent data ensures the vectorial fidelity of the seismic wave modes.

Thesis statement

This thesis addresses the research question: **How can the quality of seismic images be improved when data are contaminated with near-surface scattering noise?** To answer this question, I first propose to model elastic wave propagation in complex near-surface models to generate realistic synthetic data with different types of NSS. Subsequently, polarization methods and machine learning workflows will be designed to attenuate NSS noise in multicomponent data. The objectives of this thesis are presented below:

Main Objective.

- To develop strategies based on elastic wave propagation, polarization methods, and machine learning, to model and process the near-surface scattering noise in multicomponent seismic data.

Specific Objectives.

- To generate synthetic seismic data with realistic scattering by 3D elastic wave modeling in complex near surface media.
- To remove scattering noise from multicomponent seismic shot gathers implementing a workflow based on polarization methods and machine learning.
- To evaluate the performance of the designed scattering-noise removal workflow with synthetic and real seismic data.

Thesis organization and main contributions

This thesis is divided into two parts: modeling and processing, as detailed in Figure 2.

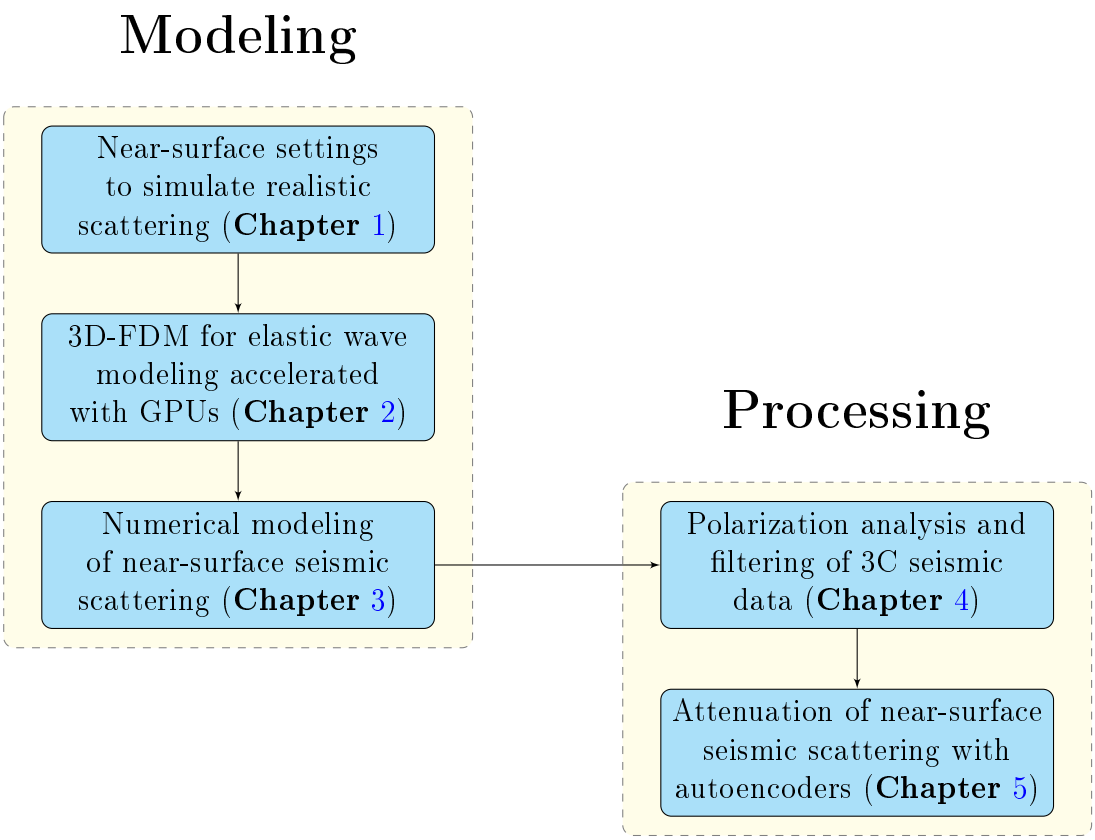

Figure 2. Thesis organization.

The modeling part, comprised of three chapters, focuses on the generation of realistic noisy synthetic data through 3D finite-difference elastic wave propagation. Chapter 1 presents the limitations of the current SEAM phase II Foothills model, particularly its restricted representation of near-surface heterogeneity and a low-velocity layer. The chapter underlines the need for more comprehensive models that can accurately capture scattered surface wave

energy in seismic simulations in mountainous onshore regions. Chapter 2 introduces a novel 3D solver, PMFD3D-GPU, designed for GPU acceleration to handle the computational complexities of modeling seismic wave propagation in intricate terrains. This solver employs an unstructured index array representation to accommodate complex near-surface models, proving to be both highly efficient in computational speed and accurate when compared to established solvers. In Chapter 3, the partitioned domain method (PDM) is presented to augment NSS modeling accuracy. Utilizing two stages of elastic wave modeling to generate synthetic seismic data, this method effectively models NSS, thereby contributing to a better understanding of land seismic noise and fostering the development of new attenuation techniques.

The processing part of the thesis encompasses two chapters and concentrates on designing methods and workflows to attenuate NSS in multicomponent shot gathers. Chapter 4 introduces a novel two-step method, the 3C Frequency-Slowness Polarization Filter (3C-FSPF), for polarized wave type separation in seismic data. It addresses the limitations of existing polarization filter techniques and demonstrates potential for enhancing the quality of 3C seismic data, particularly in regions with complex near-surface structures and spatial undersampling. The filter was evaluated using a real 3C shot gather obtained from seismic data collected in the Middle Magdalena Valley in Colombia, demonstrating the ability of the 3C-FSPF to successfully separate different types of waves in the ground roll cone. Finally, Chapter 5 extends the work of Chapter 4 by introducing machine learning workflows to automate the NSS attenuation process. Leveraging autoencoders, this method shows promise

in reducing NSS noise and enhancing the quality of deeper reflections in 3C seismic data. This contributes to the wider field of exploration geophysics. Future research will aim to validate these methods with real data and refine the techniques further using a more diverse range of training datasets.

The main contributions of this thesis are:

1) Development of a GPU-accelerated 3D solver for elastic wave modeling in media with irregular topography. Compared to CPU implementations, this solver substantially lowers computational costs enabling more realistic and detailed seismic simulations even in areas with complex near-surface structures.

2) A novel strategy for accurate near-surface seismic scattering (NSS) modeling was designed. This strategy permits the generation of synthetic data with or without NSS, leading to a more profound understanding of land seismic noise and aiding in the development of innovative noise attenuation methods.

3) An innovative multi-station polarization filter was created for wave type separation in 3C seismic data. This filter, which makes use of tailored functions from elliptical spectra in the frequency-slowness domain, showed excellent performance. Its effectiveness was validated using both synthetic and real data, providing significant improvements to the quality of undersampled seismic data, particularly those acquired in areas with complex near-surface structures.

4) Machine learning workflows were implemented for the processing of multicomponent seismic data. Through the incorporation of machine learning techniques, the process

of NSS attenuation was automated. This approach greatly mitigates NSS noise and enhances the quality of deeper reflections in 3C seismic data, suggesting a promising path for further enhancements in seismic data processing.

CHAPTER 1. Simulation of near-surface seismic scattering on mountainous onshore areas: understanding the ground roll "energy cone"

1.1. Abstract

Accurately simulating seismic surface waves on complex land areas is essential for understanding the propagation of seismic waves. The SEAM phase II Foothills model, proposed by the SEG Advanced Modeling Consortium, is a comprehensive effort to understand seismic wave propagation in foothills areas. However, despite including rough topography, alluvial sediments, and complex geological structures, synthetic data from the SEAM consortium do not reproduce the qualitative characteristics of scattering energy that is generally interpreted as the ground roll energy cone on shot records of real data.

Simulating scattering in a near-surface elastic model in mountainous areas must include three elements: (1) rough topography and bedrock, (2) low-velocity layer, and (3) small-scale heterogeneities (approximately Rayleigh wavelength size). The SEAM Foothills model integrates only the first element and partially the second. In this chapter, the heterogeneous near-surface is examined as a random medium characterized by two parameters: the average size of the heterogeneities and fractional fluctuation. The effect of each parameter on the synthetic data, and its similarity to real data collected in a foothills region in Colombia, is analyzed.

This study indicates the necessity of incorporating the low-velocity layer and small-scale distributed heterogeneities in the shallow section of the SEAM model to achieve synthe-

tic data with realistic scattered surface wave energy. As a result, it highlights the importance of recognizing the limitations of existing models, as well as the requirement for more inclusive models, to accurately simulate near-surface seismic scattering in complex land areas.

1.2. Introduction

In the last two decades, the geophysics community has become aware of the importance of a detailed near-surface model to understand the complexity and richness of the recorded wavefield. The near-surface commonly consists of a soil column and low-velocity, unconsolidated, heterogeneous, and weathered layers of rock (Yilmaz, 2015). Most seismic sources are on the surface or a few meters below it, completely or partially contained in this near-surface layer. The near-surface has generally low velocities so that most of the seismic energy is trapped at this layer that acts as a natural waveguide.

Dispersion, scattering, and attenuation are important surface wave propagation phenomena controlled by the near-surface properties. Dispersion of surface waves is commonly produced by vertical velocity variations in the soil column that cause each frequency component of the wavefront to travel at a different phase velocity. Normally, dispersion curves of surface waves are inverted to estimate one-dimensional S-wave velocity profiles of the near-surface (Xia et al., 1999; Socco and Strobbia, 2004). Scattering of surface waves is the irregular and diffuse dispersion of energy caused by near-surface heterogeneities that act as secondary sources during the wave propagation. Depending on the type of heterogeneity, the scattering can include body-to-body, body-to-surface, surface-to-body, and surface-to-surface wave scattering (Levander, 1988). Heterogeneous near-surface includes rough topo-

graphy, irregular bedrock, and localized scatterers. Rough topography and irregular bedrock are commonly included in the design of velocity models to compute synthetic data, while localized scatterers are rarely included in the near-surface model. According to Stork (2020), very small-scale heterogeneities in the near-surface on the scale of 0.5-10 meters can produce high levels of scattered energy because the surface wavelength is about 1-10 meters in the top 10-30 m of the earth, where S-wave velocities are about 100-200 m/s, for high frequency energy in the range of 20-80 Hz. The third property, attenuation of surface waves, is produced by fluids in pores in the near-surface acting as a low-pass filter affecting strongly high-frequency wave motion. For this work, seismic waves are modeled as elastic waves so that attenuation is not considered.

An accurate simulation of seismic waves in mountainous areas requires a numerical method to model elastic wave propagation in complex areas. Surface topography and curvilinear interfaces are the principal challenges to be faced because most of the numerical solution generates spurious values by the staircase adaptation of the grid in irregular interfaces. Several numerical methods have been developed to improve the accuracy and performance of the modeling in such conditions. Some of the most relevant numerical methods are rectangular finite-difference (Robertsson, 1996; Hayashi et al., 2001; Cao and Chen, 2018), curvilinear finite-difference (Tessmer and Kosloff, 1994; Hestholm and Ruud, 1998; de la Puente et al., 2014), finite-elements, such as the spectral element method (Komatitsch et al., 1999; Komatitsch and Tromp, 1999; Peter et al., 2011), and the discontinuous Galerkin method (Monk and Richter, 2005). However, the accuracy of surface wave modeling depends not only on

the numerical method to solve the elastic wave equation but also on the velocity model.

The near-surface model must include the following three elements to simulate the "ground roll energy cone": (1) rough topography, (2) low-velocity layer, and (3) significant small-scale heterogeneities that act as scatterers. Despite that, most of the near-surface velocity models designed to study seismic wave propagation do not fulfill all the conditions that make complex surface wave propagation. For instance, The SEG Advanced Modeling (SEAM) phase II foothills model includes the element (1) and partially the element (2), with 350 m/s minimum S-wave velocities and mean ratio between P-wave and S-wave velocities of approximately 1.8.

This study of this chapter proposes an approach to the elements (2) and (3) by incorporating a low-velocity surface layer with a high ratio between P-wave and S-wave velocities, along with a random media model that represent the heterogeneities in a modified version of the near-surface of the SEAM Foothills model. A comparison is made between synthetic data recorded on a modification of the SEAM model and real data acquired in a foothills area in Colombia, equivalent to the SEAM model. This comparison serves to underscore the significance of the heterogeneous near-surface in reproducing the surface waves behavior of real data within the synthetic data.

1.3. Data and models

Synthetic surface waves in associated to SEAM foothills model are compared to real data acquired in a foothills area in Colombia. Data and models used in the study are presented below:

1.3.1. SEAM phase II foothills model. The SEAM Phase II Foothills model was designed by the SEAM Consortium (Society of Exploration Geophysicists Advanced Modeling) between 2011 and 2016 to understand the complexity of seismic wave propagation in mountainous onshore areas, particularly in the Andean foothills (Oristaglio, 2013; Regone et al., 2017). The model covers a horizontal extent of approximately 14.5 by 12.5 km and a depth extent of 11 km, with an elevation map taken from an area in the Llanos foothills in Colombia (see Figure 3). The P-wave velocities in the model range from approximately 500 to 4956 m/s, the S-wave velocities from approximately 350 to 2854 m/s, and the density from approximately 1.7 to 2.7 Mg/m3. This model is ideal for studying the effects of complex geological structures on seismic wave propagation. However, synthetic data computed on this model do not exhibit the complex characteristics of the ground roll energy cone observed on real shot records. Therefore, several shot gathers in the synthetic data were meticulously examined and one with a ground roll cone closely resembling that observed in real shot gathers was chosen. Reciprocally, real shot gather most similar to the synthetic one was also selected for further analysis.

1.3.2. Numerical modeling validation. The purpose of our study is to compute synthetic data with realistic surface wave behavior by modifying the near-surface of the SEAM Foothills model. Synthetic data on the modified models are computed using a solver named PMFD3D-GPU, which will be introduced in chapter 2. This solver is a rectangular finite-difference code that uses the parameter-modified method introduced by

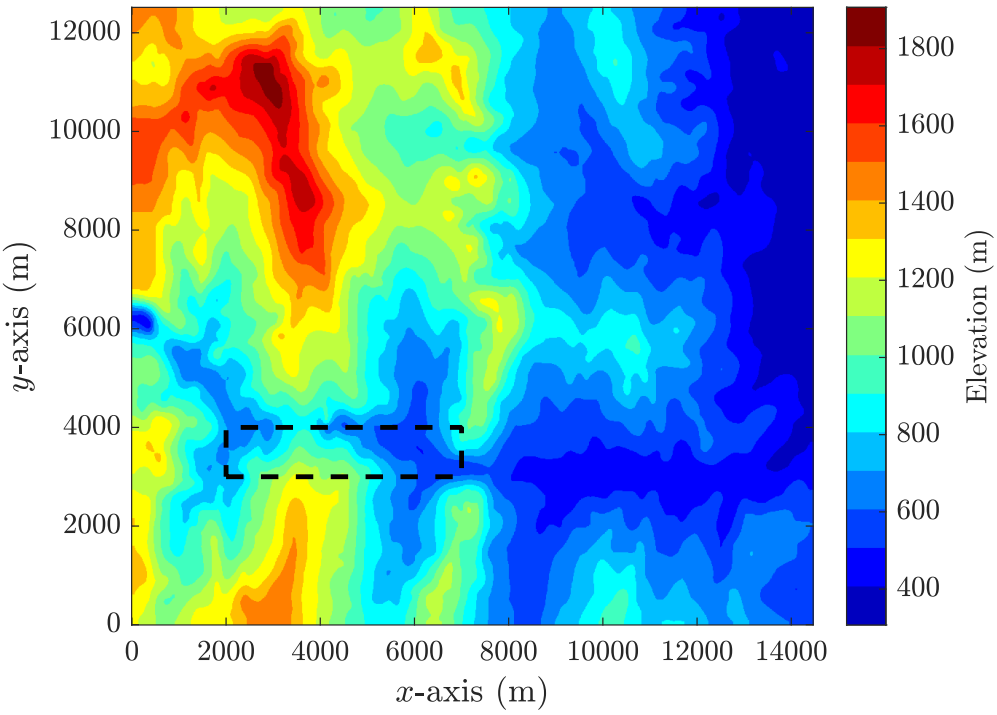

Figure 3. Elevation map of the SEAM phase II foothills model. The selected portion of the model (highlighted by the black-dashed box) is from 2000 to 7000 m in the x-axis, from 3000 to 4000 m in the y-axis, and from 1600 to 4000 m in the z-axis.

Cao and Chen (2018) to solve the free-surface condition for irregular topography.

The SEAM Consortium computed synthetic seismic data by using the spectral-element solver SPECFEM 3D (Komatitsch and Tromp, 2002; Peter et al., 2011). Seismic sources were imposed as vertical component point forces at the surface, simulating an ideal Vibroseis source with a 40 Hz Klauder wavelet (Oristaglio, 2013).

The solver is validated by comparing a representative shot gather generated by SPECFEM 3D to a shot gather produced by PMFD 3D. To calculate synthetic data using PMFD 3D, a segment of the SEAM model that spans 5000 m x 1000 m x 2400 m is chosen, with velocities varying from 500 to 4800 m/s and density ranging from 1.85 to 2.6 Mg/m3. The

black-dashed box in Figure 3 indicates the portion of the model selected for this work. It spans from 2000 to 7000 m on the x-axis, from 3000 to 4000 m on the y-axis, and from 1600 to 4000 m on the z-axis. Figure 4(a) shows a 3D view of the P-wave velocity model for a portion to the SEAM, while Figure 4(b) shows a 2D section at 3500 m on the y-axis.

The PMFD 3D solver requires a spatial sampling of 15 grid points per minimum wavelength to accurately resolve surface waves. The original model is specified on a grid with cubic cells measuring 10 m on each side. Linear interpolation is utilized to resample the model on cubic cells measuring 2.5 m on each side. In these simulations, seismic sources are imposed as normal-stress point forces, emulating an ideal explosive source with a 10 Hz Ricker wavelet.

For the modeling, the source is located at 2750 m on the x-axis and 3500 m on the y-axis, and the receivers are placed along the 3500 m stretch of the y-axis, from 2050 m to 5500 m, and at 50 m intervals on the 3500 m stretch of the x-axis. Some similarities are observed between the shot gathers generated by using SPECFEM 3D and PMFD3D-GPU, observed in Figures 5(a) and 5(b), respectively. The first arrivals are quite similar, as well as the surface wave behavior. There is a reduction in amplitude for traces between 3450 m and 3750 m on the x-axis, caused by the impedance contrast of the high-velocity outcrop highlighted in Figure 4(b). However, some differences can be noted in the shot gathers. It appears that, for PMFD 3D, more energy is trapped at the surface, and a minor energy of reflections is recorded.

Two sources of uncertainty exist in the validation process. The source wavelet differs

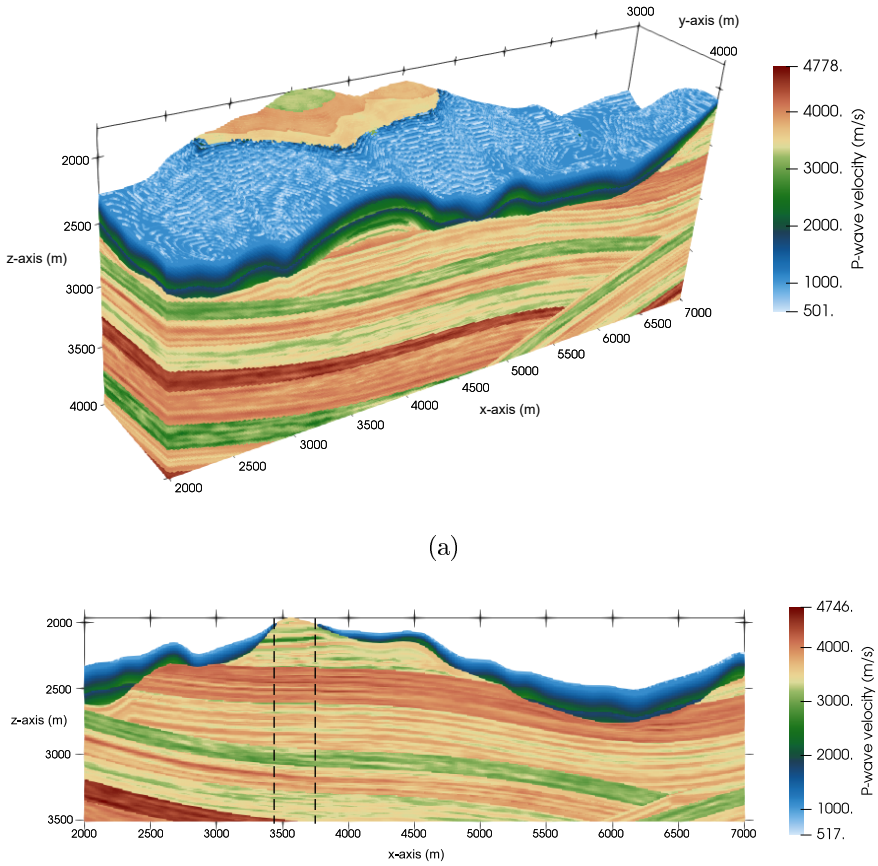

Figure 4. P-wave velocity variations in the portion of the SEAM phase II foothills model used to analyze the surface waves behavior. (a) 3D view of the model. (b) 2D section at 3500 m in the y-axis. The dashed lines highlight a high-velocity outcrop between 3450 m and 3750 m in the x-axis.

for each solver, and for PMFD3D-GPU, only a portion of the model is used, while the SEAM Consortium employed the entire model for SPECFEM3D. Despite these uncertainties, the focus remains on the surface wave behavior of the synthetic data. Figures 5(c) and 5(d) present the dispersion image for each shot gather. It is observed that the dispersion curves of the fundamental and higher modes of the Rayleigh waves bear significant similarity, showing that PMFD3D-GPU can accurately resolve the surface waves.

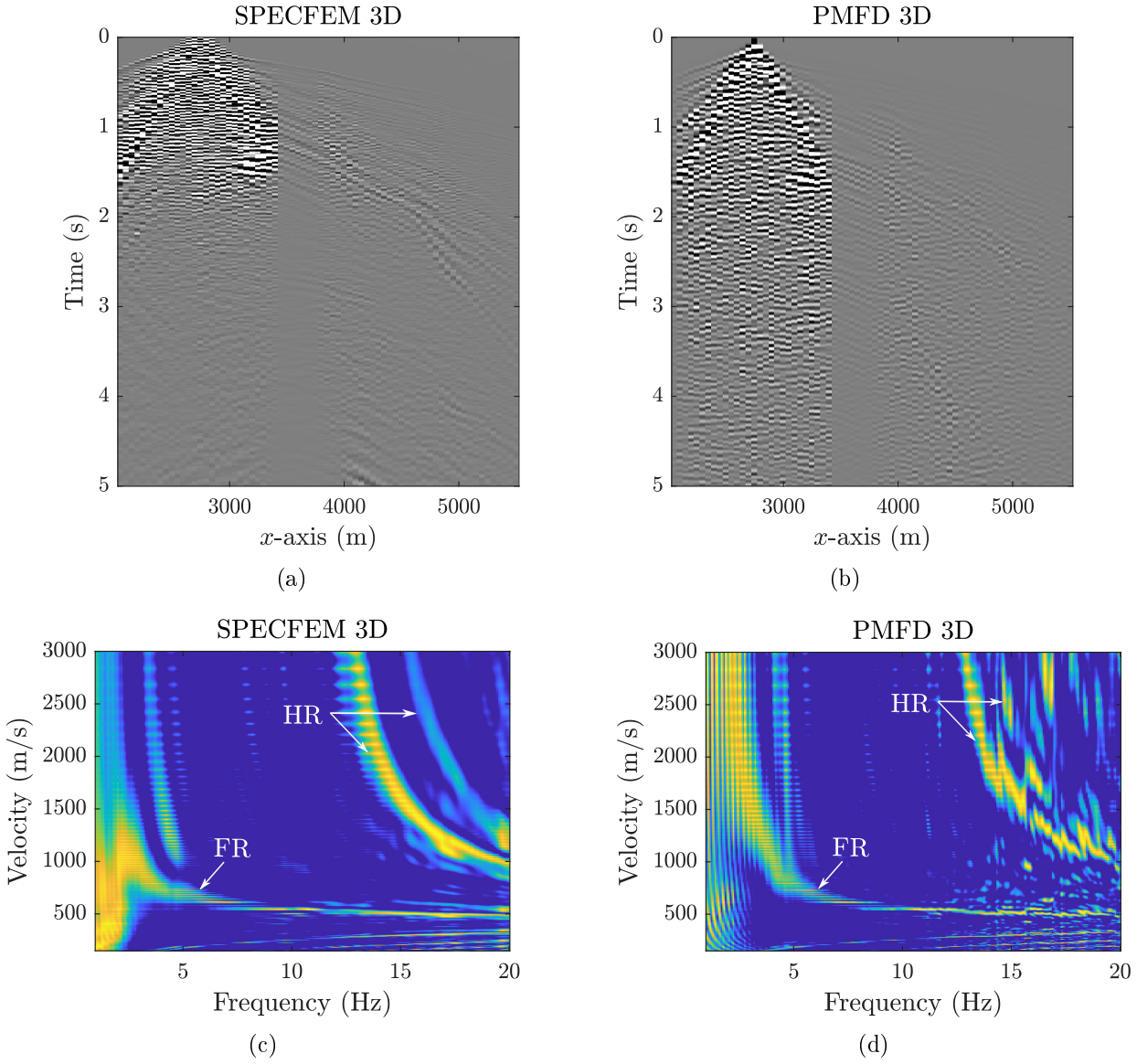

Figure 5. Synthetic data recorded on the SEAM Foothills model. (a) Shot gather generated by using the spectral finite-elements solver (SPECFEM 3D). (b) Shot gather generated by using the parameter modified finite-difference method (PMFD 3D). (c) The dispersion image from (a). (d) The dispersion image from (b).

1.3.3. Real data in the Colombian Foothills. This study utilizes a real dataset gathered from the Llanos Foothills of Colombia, whose topography matches that

of the SEAM Phase II Foothills model. Figure 6 indicates the acquisition area for the real data. A representative shot gather is selected to facilitate a comparison between the real and synthetic data (Figure 9(a)). Traces between 4600 m and 4750 m along the x-axis exhibited noise and were nullified during a preprocessing step. Figure 7(a) displays the locations of the source and receivers for both the real and synthetic data corresponding to the selected shot gather. Despite the shot and receivers not being precisely in the same location, they are sufficiently close for surface wave analysis, and the elevation structure of the receivers is almost identical (Figure 7(b)).

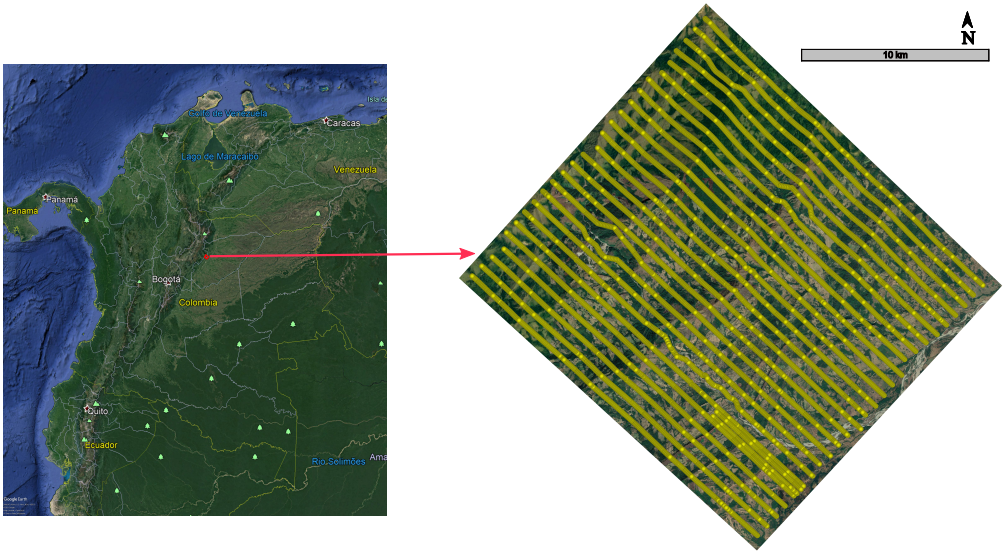

Figure 6. The geographic area of the real data acquisition in the Llanos Foothills of Colombia, South America. Location of the receivers are represented by yellow points.

1.4. Modification of the near surface in the SEAM phase II foothills model:

This section elaborates on the modifications introduced to the near-surface of the SEAM Foothills model with the aim to generate more complex surface waves in the synthetic data. Two key modifications are contemplated for this objective. Firstly, the inclusion of a

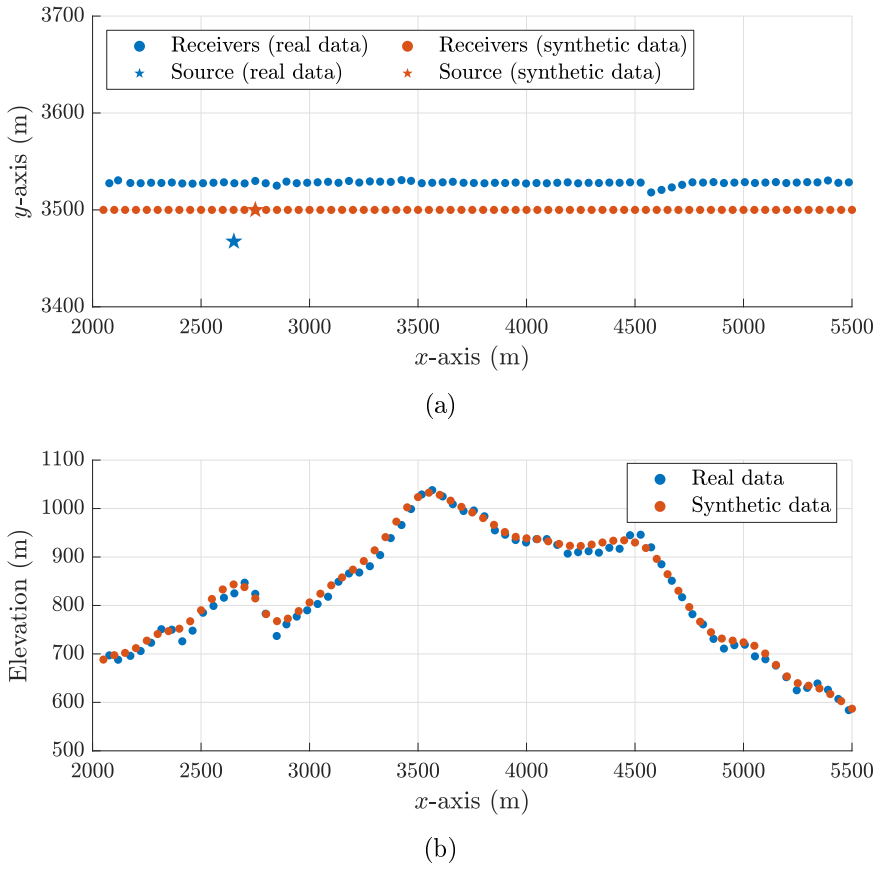

Figure 7. Acquisition geometry for the real and synthetic data of the selected shot gather. (a) Location of receivers and source in the x-axis and y-axis. (b) Elevation of receivers.

low-velocity layer in the near-surface, and secondly, the implementation of a perturbation to that layer through a random heterogeneous medium. To distinguish each model, the following acronym will be utilized:

- P-SEAM: Portion of the original SEAM Foothills model presented in Figure 4.
- LV-SEAM: First modification of the P-SEAM model by including a low-velocity layer in the near-surface.
- RHLV-SEAM: Second modification of the P-SEAM model by including a low-velocity

layer in the near-surface and perturbing that layer by using a random heterogeneous medium.

Details about each modification are presented below.

1.4.1. Low-velocity surface layer. A portion was extracted from the P-SEAM model where P-wave and S-wave velocities are below 1500 and 830 m/s, respectively. This extracted segment is attributed with background P-wave and S-wave velocities of 1400 and 400 m/s, respectively. These velocities are chosen to be higher than those referenced by Stork (2020) because utilizing lower velocities would necessitate smaller discretization sizes for numerical modeling, thereby increasing the computational cost. Nonetheless, the V_P/V_S ratio was maintained at 3.5, aligning with the near-surface models used in the simulations documented in Yilmaz (2015). Table 1 shows the elastic parameter information for the near-surface of the low-velocity layer SEAM model (LV-SEAM).

Table 1
Elastic near-surface parameters for the low-velocity layer SEAM model (LV-SEAM).

V_P (m/s)	V_S (m/s)	ρ (Mg/m^3)	V_P/V_S	Maximum thickness (m)
1400	400	1.85	3.5	110

1.4.2. Random heterogeneous near-surface model. The low-velocity layer incorporated in the initial modification is perturbed with a random medium for each elastic parameter in the following manner:

$$
\begin{aligned}
V_P &= V_{P0} + \delta V_P(\mathbf{x}), \\
V_S &= V_{S0} + \delta V_S(\mathbf{x}), \\
\rho &= \rho_0 + \delta\rho(\mathbf{x}),
\end{aligned}
\tag{1}
$$

where $\mathbf{x}$ is the coordinate in the random heterogeneous media, $\delta\rho$, δV_P and δV_S denotes the variation of density, and $P-$ and $S-$ wave velocities, respectively. Subscript zero denotes a homogeneous background medium. The background medium parameters are presented in Table 1.

In this study, we establish a proportionality relationship between P-wave and S-wave velocities and density to simplify the characterization of the medium. As suggested by Maeda et al. (2008), we assume the following proportionality:

$$
\xi(\mathbf{x}) = \frac{\delta V_P(\mathbf{x})}{V_{P0}} = \frac{\delta V_S(\mathbf{x})}{V_{S0}} = \frac{1}{\chi_0}\frac{\delta\rho(\mathbf{x})}{\rho_0}. \tag{2}
$$

Here, ξ represents the fractional fluctuation of the parameters, and χ_0 is a constant that captures the linear relationship. We calculate the value of χ_0 using the Birch law (Birch, 1961), which relates P-wave velocity and density. In our study, we adopt $\chi_0 = 0.04$, which is derived from the equation $V_P = 3.05\rho - 1.87$, with a reference background P-wave velocity of $V_{P0} = 1400$ m/s.

In heterogeneous stationary random media, the fractional fluctuation can be charac-

terized by using an Autocorrelation Function (ACF) (Sato et al., 2012).

$$R(\mathbf{x}) = \langle \xi(\mathbf{y}+\mathbf{y}), \xi(\mathbf{x}) \rangle \,, \tag{3}$$

which gives a statistical measure of the spatial scale and the magnitude of medium heterogeneity. There are several types of ACFs of random media that can be assumed in seismic wave propagation (Gaussian, exponential, and van Karman). In this study, it is assumed the Gaussian , which is defined as follows:

$$R(\mathbf{x}) = \epsilon^2 e^{-|\mathbf{x}|^2/a^2}, \tag{4}$$

where a is the correlation length (average size of the heterogeneities), and ϵ is the root mean square of the fractional fluctuation. Details about how to compute a realization of a random fractional fluctuation from a specific ACF can be found in (Sato et al., 2012). Figure 8(a) shows an example of a RHVL-SEAM model, which contains a random heterogeneous near-surface perturbed with the fractional fluctuation realization of Figure 8(b). The realization is generated with the Gaussian ACF with $a = 36.8$ m and $\epsilon = 0.2$.

1.5. Parametric analysis of the heterogeneous random near-surface model

The primary objective of the parametric analysis is to examine the impact of the parameters a and ϵ on the synthetic data. Elastic wave modelling is performed across six distinct realizations of the RHLV-SEAM model. For the first three models, $\epsilon = 0.2$ is set, and three varying values of a are used, functioning as a proportion of the Rayleigh wavelength

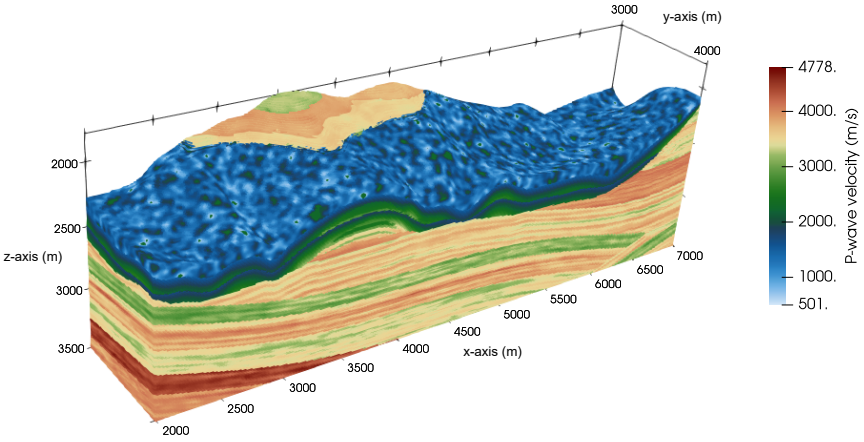

(a)

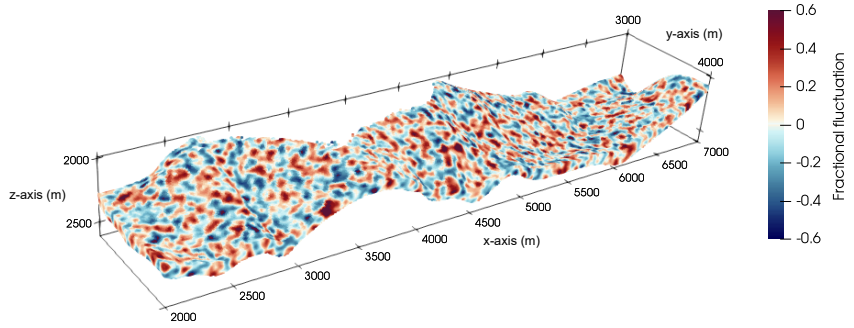

(b)

Figure 8. Modification of the elastic parameters in the shallow part of the portion of the SEAM phase II foothills model. (a) 3D P-wave velocity variations of the model perturbed by a random heterogeneous near-surface. (b) A fractional fluctuation realization used to perturb the elastic parameters at the near-surface. This realization is generated with a Gaussian ACF with $a = 36.8$ m and $\epsilon = 0.2$.

$a = (0.5\lambda_R, \lambda_R, 2\lambda_R)$. The Rayleigh wavelength is calculated by $\lambda_R = 0.92V_{S0}/f_c$, where f_c represents the central frequency of the wavelet source. With $V_{S0} = 400$ m/s and $f_c = 10$ Hz, the Rayleigh wavelength is $\lambda_R = 36.8$ m. For the remaining three models, $a = \lambda_R$ is set and three different values of fractional fluctuations $\epsilon = (0.05, 0.1, 0.2)$ are utilized.

The corresponding shot gathers for the real and synthetic data are displayed in Figure

9. The shot gather of real data exhibits complex surface waves with a high level of scattered energy (Figure 9(a)). On the contrary, the synthetic shot gather recorded on the P-SEAM exhibits a more homogeneous behavior of the surface waves, even body-wave reflections events can be visually identified within the ground roll cone (Figure 9(b)). The shot gather recorded on LV-SEAM shows a slower velocity of the Rayleigh wave closer to the real data and clearly different from the data recorded on the P-SEAM model. The shot gathers from the six different realizations of the RHLV-SEAM model are displayed from Figure 9(d) to Figure 9(i). In these shot gathers, we observe an evident increase of the scattering energy compared with the data recorded on the P-SEAM and LV-SEAM models. Further, there is a gradual increase in the scattering energy as ϵ increase and a gets closer to the Rayleigh wavelength.

One of the most used domains to analyze surface waves is the dispersion image in the frequency-phase velocity domain. This domain is generally computed when the shot location is in the same line of receivers. For the synthetic data, the source is located at the same receivers' line while in the real acquisition the shot location is about 50 m of perpendicular distance offline (Figure 7(a)). This distance can be neglected relative to the 2750 m of maximum offset. Figure 10 shows the dispersion images for the corresponding shot gather panels in Figure 9. For the real dispersion image, the fundamental mode of the Rayleigh wave FR and a higher mode of Rayleigh wave HR are identified (Figure 10(a)).

We observe that the fundamental mode is not discernible for frequencies higher than 5 Hz, while the higher mode appears between 16 and 18 Hz. Synthetic data recorded on the

P-SEAM model shows that the dispersion image contains continuous curves spanning the entire frequency range for both the fundamental and higher modes (Figure 10(b)). Figure 10(c) displays a shift in the curves for the fundamental and higher modes due to the lower velocity in the LV-SEAM model. Additionally, patches of energy can be identified at frequencies exceeding 15 Hz. These patches of energy are interpreted as Rayleigh waves scattering (SR), as the synthetic data computed on the LV-SEAM model exhibits shorter Rayleigh wavelengths that are more susceptible to scattering with topographical variations.

These blotches of scattered energy are more noticeable in the dispersion image from data recorded on the RHLV-SEAM models. Figures 10(d) to 10(f) illustrate the impact of the correlation length, a. The fundamental mode in all cases is no longer easily identifiable. The influence of the parameter ϵ can be observed in Figures 10(g) to 10(i). It can be noted that the larger the parameter ϵ, the greater the scattering energy, which complicates the identification of dispersion curves for the fundamental and higher modes of Rayleigh waves.

1.6. Discussion

The numerical experiments show that the modifications performed on the SEAM Foothills model allow computing synthetic data with more complex surface waves behavior. This complex behavior corresponds to the scattering energy produced by the topographic variations and the heterogeneities included in the near-surface. The scattering is a phenomenon that strongly depends on the relative length scale between the heterogeneity size and the seismic wavelength. If the heterogeneity size is large compared to the seismic wavelength, then the scattering energy is mainly concentrated in the axis of the propagation ray path

and can be considered as reflection and refraction instead of scattering. On the other hand, If the heterogeneity size is small compared to the seismic wavelength, then the scattering becomes approximately isotropic with energy that vanishes as the medium behaves like a homogeneous solid. According to Aki and Chouet (1975), the scattering effects are strongest when the heterogeneity size is comparable with the seismic wavelength.

In the first modification, a low-velocity layer is incorporated at the near-surface. This facilitates the generation of shorter Rayleigh wavelengths that demonstrate greater susceptibility to scatter with the topographic variations of the P-SEAM model. These variations range in elevation from -45 m to 27 m from the mean, quite close to the central Rayleigh wavelength, which is about 36.8 m for the LV-SEAM model. The second modification involves the inclusion of heterogeneities in the near-surface through a random media model with Gaussian ACF. The size of the heterogeneities and the impedance contrast are controlled with parameters a and ϵ, respectively. From the results presented in Figures 9 and 10, we observe that surface waves are more complex for $\epsilon = 0.2$ and $a = (0.5\lambda_R, \lambda_R)$, validating the increase in scattering energy with the impedance contrast and with a heterogeneity size close to the Rayleigh wavelength. Visually, the panel with parameters $\epsilon = 0.05$ and $a = \lambda_R$ is considered the most similar to the real data.

In this study, we assume that the random heterogeneous media is a stationary process, meaning the average size of the heterogeneity remains independent of depth and position. However, in reality, a gradational behavior might be more accurate, with the size and impedance of the heterogeneities functioning as a variable of depth under certain sedimentary condi-

tions. A modified random media model could, therefore, incorporate variations in the size of the heterogeneity and impedance as a function of depth. Additionally, it may be worthwhile to include isolated localized heterogeneities that are frequently found in real-world scenarios.

It's important to clarify that this study focuses on the forward problem, and there is no attempt to estimate model parameters by fitting the modeled and real data. The work by Irving et al. (2010), which estimates the parameters of the ACF of the random media by inverting the scattering energy, may be of interest to readers.

In the numerical modeling, a Ricker wavelet source of 10 Hz is assumed. To ensure a closer alignment between synthetic and real data, a source wavelet should be estimated from the real data. The frequency of the source controls the range of exciting wavelengths propagating through the heterogeneous media. Therefore, the source frequency plays a critical role in the scattering phenomenon as the scattering energy intensifies when the wavelength is on a similar scale to the heterogeneity size.

Finally, the domain to measure the realism of the synthetic data is worthy of discussion. In this study, synthetic and real data are compared in two different domains: the shot gather ($t - x$ domain) and the dispersion image ($f - v$ domain). An extended comparison could be conducted using seismic attribute analysis in pre-stack (Sánchez-Galvis et al., 2016; Sánchez-Galvis et al., 2017; Xia et al., 2018). It is believed that a comparative analysis in the pre-stack attribute space can provide more detailed information about the closeness of the synthetic data to the real one.

1.7. Conclusions

This study presents an approach to reproducing the complex ground roll energy cone seen in synthetic seismic data on mountainous onshore areas. The approach proposed aims to construct realistic near-surface models that ideally incorporate three key elements: (1) rough topography and bedrock, (2) a low-velocity layer, and (3) small-scale distributed heterogeneities. The focus of this study was on elements (2) and (3) to simulate the complex ground roll cone. The behavior of surface waves was compared between a real dataset, acquired from the Llanos foothills in Colombia, and synthetic datasets that were recorded on modifications of a portion of the SEAM Foothills model. A modification to the near-surface model was proposed, which included a low-velocity surface layer with a high P-wave to S-wave velocity ratio, along with a random distribution of heterogeneities following a Gaussian autocorrelation function. A parametric analysis was conducted to examine the influence of the average size of heterogeneities and the contrast impedance on the synthetic data. The results suggest that scattering energy is more pronounced for higher impedance contrasts and when the size of the heterogeneity is close to the Rayleigh wavelength. Therefore, the findings from this study underscore the necessity to include a low-velocity layer and small-scale distributed heterogeneities in the near-surface of the SEAM model. This allows for the computation of synthetic data that can realistically mimic scattered surface wave energy.

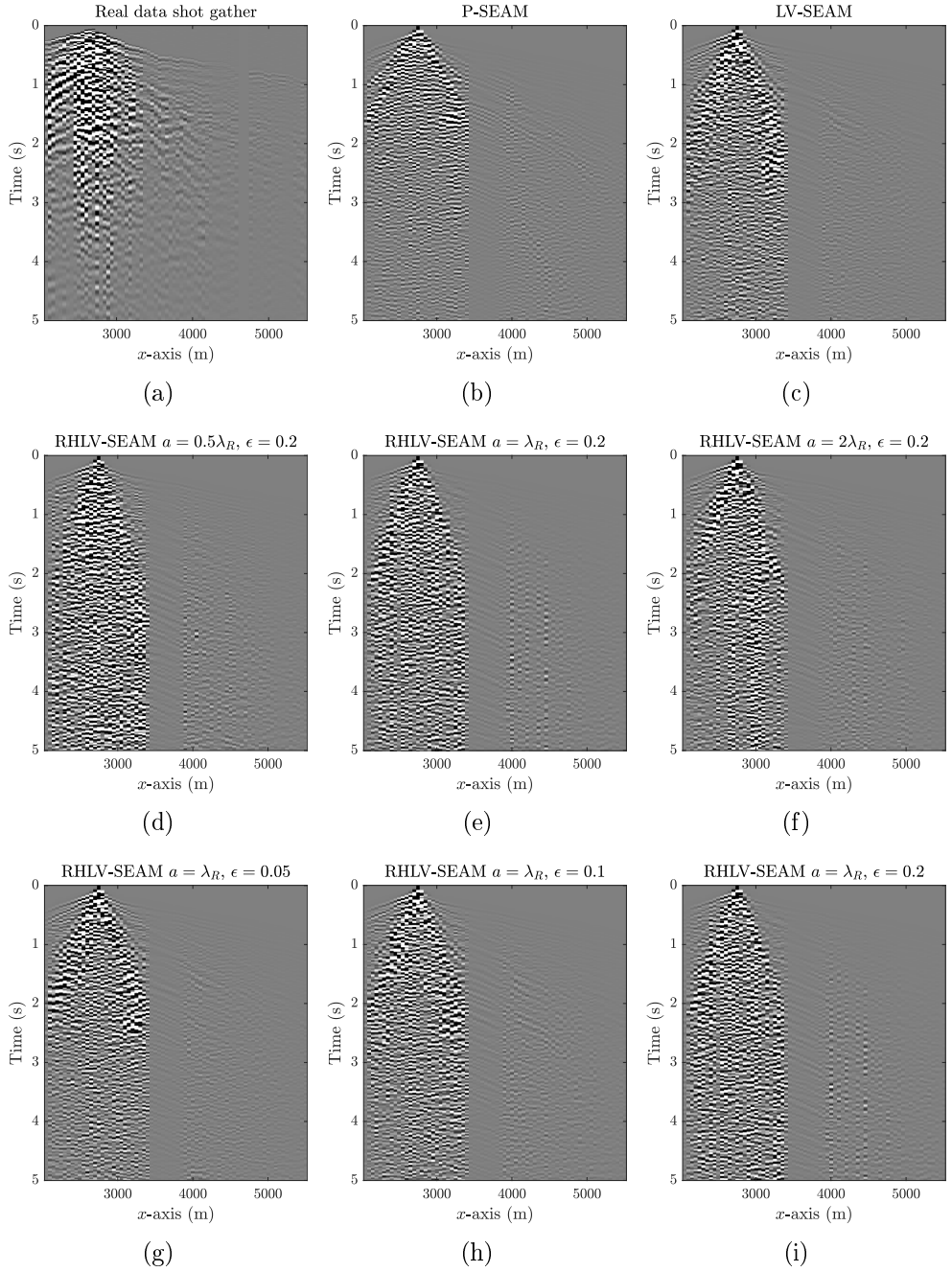

Figure 9. Synthetic and real data comparison for parametric analysis. (a) Shot gather of real data acquired in a Colombian foothills area equivalent to the SEAM Foothills model. Shot gather for synthetic data computed on (b) portion of the original SEAM Foothills model (P-SEAM) showed in Figure 4, (c) modified SEAM Foothills model by including a low-velocity layer in the surface (LV-SEAM), (d) modified SEAM Foothills model by perturbing the near-surface with a random medium (RHLV-SEAM) with a Gaussian ACF of $a = 0.5\lambda_R$ and $\epsilon = 0.2$, (e) with $a = \lambda_R$ and $\epsilon = 0.2$ (f) with $a = 2\lambda_R$ and $\epsilon = 0.2$ (g) with $a = \lambda_R$ and $\epsilon = 0.05$ (h) with $a = \lambda_R$ and $\epsilon = 0.1$ (i) with $a = \lambda_R$ and $\epsilon = 0.2$. Figure 9(e) and 9(i) are actually the same, that are repeated for comparison purposes.

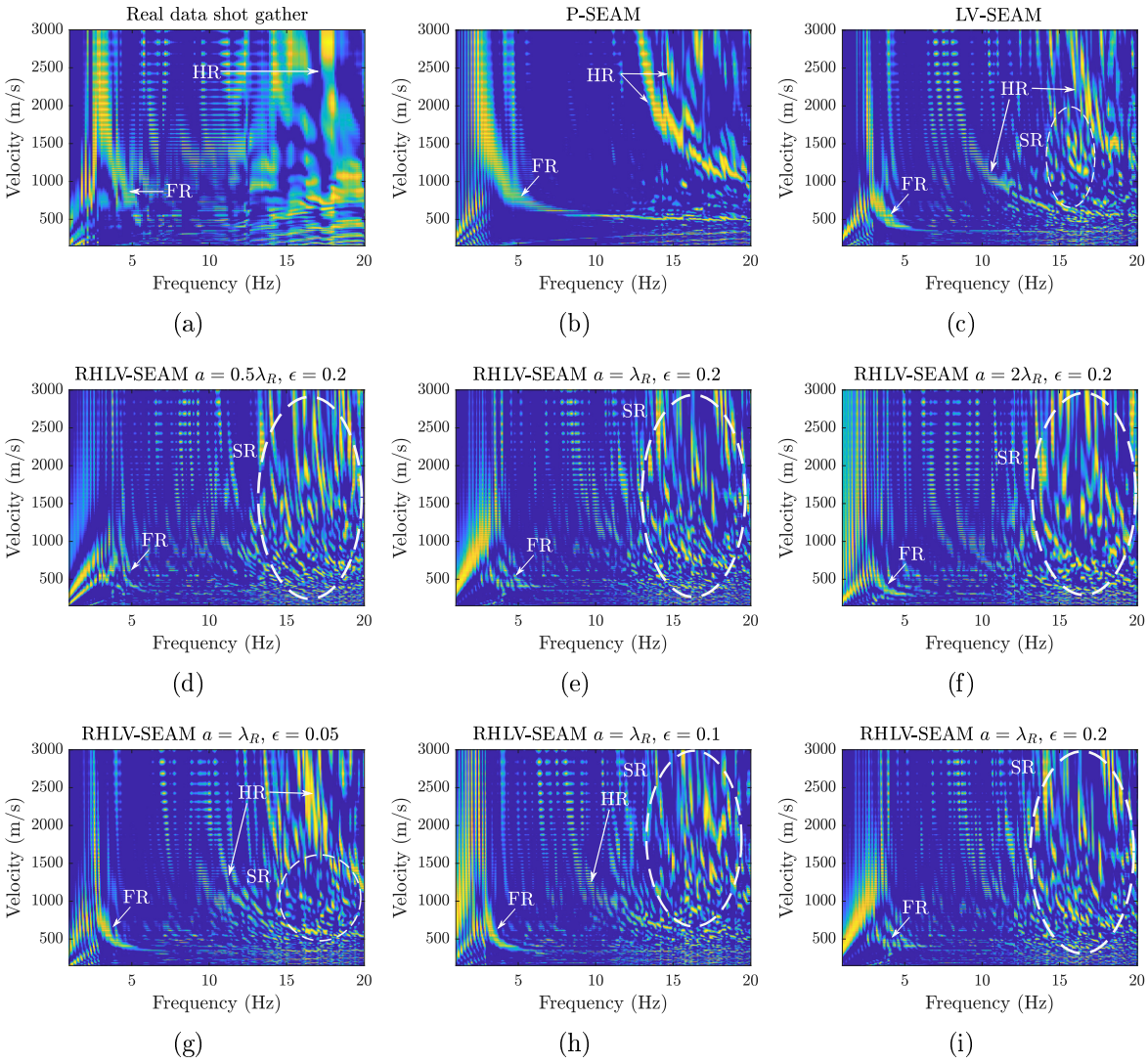

Figure 10. Dispersion images computed from the corresponding data in Figure 9. In each panel, FR is the interpreted fundamental mode of the Rayleigh wave, HR are the interpreted higher modes, and SR are the interpreted scattered Rayleigh waves. In a visual inspection, it is observed that the panel (g) is the most similar to the real data (panel (a)). The scattering energy increase as the impedance contrast increase (controlled by parameter ϵ) and with heterogeneity size (controlled by parameter a) close to Rayleigh wavelength. This explain why models with higher impedance contrast ($\epsilon = 0.2$) produce more noisy data.

CHAPTER 2. 3D-FDM for elastic wave modeling in the presence of irregular topography by using unstructured index array representation on a GPU

2.1. Abstract

Simulation of seismic wave propagation in complex, mountainous regions is a challenging task in exploration geophysics. As highlighted in Chapter 1, these challenges emphasize the need for realistic seismic wave simulations in foothill areas to contend with complex near-surface models, including rough topography, irregular bedrock interfaces, low-velocity surface sediment, and significant heterogeneities. The existing numerical methods, capable of solving the seismic wave equation under these conditions, typically necessitate a discretization model with a small grid size, thus leading to a high computational cost. To address this concern, we introduce a novel solver for 3D elastic wave modeling in the presence of irregular topography based on parameter modified (PM) formulation and finite-difference method (FDM) and designed for GPU acceleration (PMFD3D-GPU). This solver incorporates an innovative approach that involves an unstructured index array representation (UIAR) to implement the PM formulation to satisfy the free-surface condition for topographic variations. Validation of the PMFD3D-GPU solver against the well-known SPECFEM3D solver has been carried out, demonstrating L_2 misfit errors of less than 1 % in most cases of rough topography. Furthermore, an acceleration in the simulations is achieved by this solver, marking a speed-up approximately 20 times faster compared to the CPU implementation. There-

fore, the PMFD3D-GPU solver enables cost-effective, realistic, and detailed simulations of near-surface seismic scattering in heterogeneous earth models with irregular topography.

2.2. Introduction

There is a variety of numerical methods in the literature, each with unique advantages and limitations. The two most common approaches employed to model seismic waves are FDM and finite-element method (FEM). FDMs, while easy to implement and efficient for large-scale problems due to their local nature, struggle with complex geometries such as interface discontinuities and topographic variations (Virieux, 1986; Robertsson, 1996; Hayashi et al., 2001). This is due to the staircase artifacts produced by the rectangular grid. Furthermore, high-order accuracy generally requires high-order finite difference stencils, which increases both computational cost and complexity (LeVeque, 2007; Durran, 2013). Several modifications of FDM for curved or irregular domains have been proposed to reduce these staircase artifacts (Hestholm and Ruud, 1998; de la Puente et al., 2014; Solano et al., 2016). However, these modifications often complicate the interpretation of the solution and may introduce potential distortion to the solution grid reference. In contrast, FEM can manage complex geometries and heterogeneous materials (Bathe, 2006; Hughes, 2012). Despite its versatility, it is more computationally demanding and difficult to implement than FDM (Trefethen, 1996; Moczo et al., 2014). Modern extensions of FEM, like the Spectral Element Method (SEM) and the Discontinuous Galerkin Method (DGM), have been developed to overcome some of FEM's limitations. SEM improves accuracy and rate of convergence by approximating the solution within each element with high-degree polynomial basis functions

(Komatitsch et al., 1999; Komatitsch and Tromp, 2002; Capdeville et al., 2005). Additionally, the highly parallelizable nature of SEM aids in reducing computation time (Martin et al., 2008; Komatitsch et al., 2010). Similar to SEM, DGM can manage discontinuities in the solution, making it particularly suitable for problems with shocks or other sharp features (Käser and Dumbser, 2006; Dumbser and Käser, 2006; Käser et al., 2007). Both SEM and DGM allow for high computational efficiency on parallel computers due to their high degree of parallelism Komatitsch et al. (2010); Breuer et al. (2016). Despite these advantages, they are generally more complex to implement and computationally intensive due to the higher degree of freedom in each element.

Since several methods have been studied, many solvers are available to model elastic waves, each one with its unique strengths and limitations in addressing the intrinsic challenges of complex media and complex computational implementation. Some of the most used solvers are presented below:

- **SEISMIC_CPML**: This solver employs a Convolutional Perfectly Matched Layer (CPML) alongside a FDM for the numerical simulation of wave propagation (Komatitsch and Martin, 2007; Martin et al., 2010). However, it does not accommodate media with topographic variations.
- **EWEFD**: This comprises a suite of programs designed to solve the 2D and 3D anisotropic elastic wave equations . The programs runs on NVIDIA GPUs, providing a significant computational speed-up. Although the codes are part of the open-source Madagascar software package, they are not designed to handle irregular topography

(Weiss and Shragge, 2013).

- **SPECFEM3D**: This is a widely-recognized software package that employs a spectral-element method to solve the wave equation in three dimensions on unstructured meshes (Komatitsch et al., 1999; Komatitsch and Tromp, 1999; Komatitsch et al., 2010). While it can handle complex geometries and irregular topography, SPECFEM3D mesher requires each layer to be homogeneous, which is a limitation in realistic scenarios where elastic parameters are often heterogeneous. External meshers can be incorporated to address this issue. However, open-source meshers like Gmsh struggle with complex models Geuzaine and Remacle (2009), and more robust meshers, such as CUBIT, come at a charging fees.
- **SeisSol**: This is an open-source, high-performance solver developed by the Geophysics Section of the Department of Earth and Environmental Sciences at LMU Munich. It is particularly suitable for seismic wave propagation, including dynamic rupture processes. SeisSol uses the Arbitrary high-order DERivative (ADER) with DGM, allowing it to handle complex geometries and scenarios with irregular topography (Käser and Dumbser, 2006; Dumbser and Käser, 2006; Käser et al., 2007) . However, it shares the meshing limitations common to SPECFEM3D.
- **SALVUS**: This is a robust software for simulating waves in intricate 3D geological models by effectively accommodating irregular topography via SEM (Afanasiev et al., 2019). Yet, it is not fully open-source and charges to use it are required.

Due to the lack of available open-source software capable of simulating 3D elastic wa-

ve propagation in random heterogeneous media with irregular topography, a solver named PMFD3D-GPU was developed. This solver, based on the Finite Difference Method (FDM), is specifically designed for GPU acceleration. Utilizing an unstructured index array strategy, the solver incorporates the parameter-modified (PM) formulation introduced by Cao and Chen (2018). This formulation satisfies the free-surface condition for arbitrary surface topographies on rectangular grids. The PM formulation has been shown to achieve accuracy results comparable to SPECFEM3D for spatial sampling of 15 grid points per minimum wavelength (Cao and Chen, 2018). In comparisons with SPECFEM3D, PMFD3D-GPU achieved misfit errors close to 1 % in a homogeneous model with rough topography. Moreover, compared to the CPU implementation, this solver increases speed-up approximately 20 times faster by leveraging GPU acceleration. Finally, a numerical example using the SEAM Foothills Phase II model is presented, demonstrating the capacity of the solver to generate realistic synthetic data.

2.3. Elastic wave equation

In the context of seismic exploration, seismic waves are predominantly modeled as acoustic waves due to computational cost considerations. However, there is an increasing trend towards modeling these waves as elastic waves to capture the realism of Earth's subsurface behavior at the scales and frequencies relevant to seismic exploration. In such circumstances, rock formations undergo deformation when subjected to stress and consequently return to their original state once the stress is removed (Sheriff, 2002; Yilmaz, 2015).

In the derivation of the elastic wave equation, the approach outlined by Shearer (2009)

is followed, which entails combining the equation of motion with the constitutive relation for elastic materials. Adopting the index notation, the equation of motion is represented as:

$$\rho \partial_t^2 u_i = \partial_j \sigma_{ij}. \tag{5}$$

Here, u_i denotes the displacement in the $i, j = \{x, y, z\}$ direction, σ_{ij} represents the stress tensor, and ρ is the material density. The operators ∂_t and ∂_i represent the partial derivatives with respect to time and space, respectively.

On the other hand, the constitutive relation is expressed as:

$$\sigma_{ij} = \lambda \delta_{ij} e_{kk} + 2\mu e_{ij}. \tag{6}$$

In this equation, λ and μ are the Lamé parameters and e_{ij} denotes the strain tensor, which is defined as

$$e_{ij} = \left(\partial_i u_j + \partial_j u_i\right). \tag{7}$$

Substituting equation (7) into (6), the constitutive relation becomes:

$$\sigma_{ij} = \lambda \delta_{ij} \partial_k u_k + \mu \left(\partial_i u_j + \partial_j u_i\right). \tag{8}$$

Subsequently, integrating equation (8) into the equation of motion (5) yields:

$$\rho\partial_t^2 u_i = \partial_i\lambda\partial_k u_k + \partial_j\mu(\partial_i u_j + \partial_j u_i) + \lambda\partial_i\partial_k u_k + \mu\partial_i\partial_j u_j + \mu\partial_j\partial_j u_i \tag{9}$$

Equation (9) govern the elastic wave propagation in heterogeneous media. Alternatively to the index notation, this equation can be expressed in the operator notation as:

$$L_{ij}(\rho, \lambda, \mu, t)u_j(\mathbf{x}, t) = 0, \tag{10}$$

where

$$L_{ij}(\rho, \lambda, \mu, t) = \delta_{ij}\rho(\mathbf{x})\partial_t^2 - \partial_i[\lambda(\mathbf{x})\partial_j] - \partial_j[\mu(\mathbf{x})\partial_i] - \delta_{ij}\partial_k[\mu(\mathbf{x})\partial_k]. \tag{11}$$

Here, $\mathbf{x}$ denotes the position vector.

Another common approach to express the elastic wave equation for heterogeneous media is using the vector notation as follows:

$$\rho\ddot{\mathbf{u}} = \nabla\lambda(\nabla\cdot\mathbf{u}) + \nabla\mu\cdot\left[\nabla\mathbf{u} + (\nabla\mathbf{u})^{\mathrm{T}}\right] + (\lambda + 2\mu)\nabla\nabla\cdot\mathbf{u} - \mu\nabla\times\nabla\times\mathbf{u}, \tag{12}$$

where $\mathbf{u} = (u_x, u_y, u_z)$ represents the displacement vector, and $\nabla = (\partial_x, \partial_y, \partial_z)$ denotes the nabla operator.

In this chapter, the focus is on solving this equation numerically using the FDM.

2.4. Review of 3D FDM

Several FDM schemes have been proposed for elastic wave modeling (Clayton and Engquist, 1977; Virieux, 1986; Moczo et al., 2014). In this study, the staggered-grid scheme proposed by Virieux (1986) is followed for the first-order velocity-stress form.

2.4.1. First order velocity-stress form. The derivation of the elastic wave equation leads to a second-order partial differential equation. However, this can be alternatively expressed as a system of first-order partial differential equations. This transformation can be accomplished by introducing the velocity vector $\mathbf{v} = \partial\mathbf{u}/\partial t$. By replacing each component of vector $\mathbf{v} = (v_x, v_y, v_z)$ into the equation of motion (5), the system of first-order partial differential equations is expressed as follows:

$$\begin{aligned}
\frac{\partial v_x}{\partial t} &= \frac{1}{\rho}\left(\frac{\partial \sigma_{xx}}{\partial x} + \frac{\partial \sigma_{xy}}{\partial y} + \frac{\partial \sigma_{zx}}{\partial z}\right), \\
\frac{\partial v_y}{\partial t} &= \frac{1}{\rho}\left(\frac{\partial \sigma_{xy}}{\partial x} + \frac{\partial \sigma_{yy}}{\partial y} + \frac{\partial \sigma_{yz}}{\partial z}\right), \\
\frac{\partial v_z}{\partial t} &= \frac{1}{\rho}\left(\frac{\partial \sigma_{zx}}{\partial x} + \frac{\partial \sigma_{yz}}{\partial y} + \frac{\partial \sigma_{zz}}{\partial z}\right).
\end{aligned} \tag{13}$$

In the same way, by replacing each component of the velocity vector in equation (8), and subsequently applying time differentiation to both sides of the equations, the following expression is obtained:

$$
\begin{aligned}
\frac{\partial \sigma_{xx}}{\partial t} =& (\lambda + 2\mu)\frac{\partial v_x}{\partial x} + \lambda\frac{\partial v_y}{\partial y} + \lambda\frac{\partial v_z}{\partial z}, \\
\frac{\partial \sigma_{yy}}{\partial t} =& \lambda\frac{\partial v_x}{\partial x} + (\lambda + 2\mu)\frac{\partial v_y}{\partial y} + \lambda\frac{\partial v_z}{\partial z}, \\
\frac{\partial \sigma_{zz}}{\partial t} =& \lambda\frac{\partial v_x}{\partial x} + \lambda\frac{\partial v_y}{\partial y} + (\lambda + 2\mu)\frac{\partial v_z}{\partial z}, \\
\frac{\partial \sigma_{xy}}{\partial t} =& \mu\left(\frac{\partial v_y}{\partial x} + \frac{\partial v_x}{\partial y}\right), \\
\frac{\partial \sigma_{yz}}{\partial t} =& \mu\left(\frac{\partial v_z}{\partial y} + \frac{\partial v_y}{\partial z}\right), \\
\frac{\partial \sigma_{zx}}{\partial t} =& \mu\left(\frac{\partial v_x}{\partial z} + \frac{\partial v_z}{\partial x}\right).
\end{aligned}
\tag{14}
$$

Equations (13) and (14) are collectively known as the first-order velocity-stress form of the elastic wave equation.

2.4.2. Staggered grid scheme. The staggered grid scheme is widely utilized in geophysical simulations, particularly for modeling seismic wave propagation, primarily due to its improved accuracy, stability, conservation properties, and computational efficiency Moczo et al. (2014). Initially, the 3D space domain is discretized into a numerical grid with spatial steps $\Delta x, \Delta y, \Delta z$, as depicted in Figure 11(a). This scheme then arranges the components of the velocity and stress tensors at varied locations in the numerical grid to achieve more precise and stable results, as displayed in Figure 11(b). Here is a brief overview of the component arrangement:

- The normal stress tensor components σ_{xx}, σ_{yy}, and σ_{zz} are situated at the integral-grid points (i, j, k). The medium parameters (μ, λ, ρ) are also assumed to be located at these points.

- The shear stress tensor components σ_{xy}, σ_{yz}, and σ_{zx} are located at half-grid points, shifted from the integral points (Figure 11(b)).
- Similarly, the velocity components v_x, v_y, v_z are positioned at corresponding half-grid points, also shifted from the integral points (Figure 11(b)).

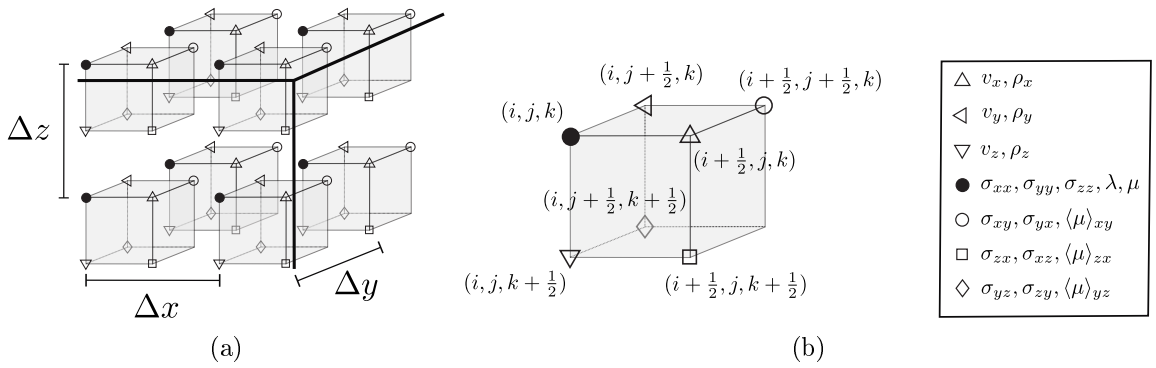

Figure 11. Staggered grid scheme. (a) 3D grid. (b) 3D cell.

Notice that the medium parameters are not defined at half-grid points as they are assumed to be situated at integral grid points (i, j, k). To overcome this, a parameter averaging method is typically utilized to determine the values of the parameters at the half-grid points.

2.4.3. Parameter averaging method. The averaging method proposed by Moczo et al. (2002) is typically used to estimate parameter values at half-grid points. According to this method, the parameter ρ at a half-grid point is calculated as the arithmetic mean of parameter values at the nearest integral grid points, as illustrated below:

$$\rho_x = \frac{1}{2}(\rho_{i,j,k} + \rho_{i+1,j,k}), \quad \rho_y = \frac{1}{2}(\rho_{i,j,k} + \rho_{i,j+1,k}), \quad \rho_z = \frac{1}{2}(\rho_{i,j,k} + \rho_{i,j,k+1}). \tag{15}$$

Here, ρ_x, ρ_y, and ρ_z denote the density values at the locations of the velocity components v_x, v_y, and v_z, respectively, as shown in Figure 11(b). However, in the majority of FDM implementations, the reciprocal value of density is preferred, which is computed at the half-grid points as follows:

$$b_x = \frac{2}{\rho_{i,j,k} + \rho_{i+1,j,k}}, \quad b_y = \frac{2}{\rho_{i,j,k} + \rho_{i,j+1,k}}, \quad b_z = \frac{2}{\rho_{i,j,k} + \rho_{i,j,k+1}}. \tag{16}$$

On the other hand, the parameter μ at a half-grid point is determined as the harmonic mean of parameter values at the nearest integral grid points, defined as:

$$\begin{aligned}
\langle\mu\rangle_{xy} &= \left[\frac{1}{4}\left(\frac{1}{\mu_{i,j,k}} + \frac{1}{\mu_{i+1,j,k}} + \frac{1}{\mu_{i,j+1,k}} + \frac{1}{\mu_{i+1,j+1,k}}\right)\right]^{-1}, \\
\langle\mu\rangle_{yz} &= \left[\frac{1}{4}\left(\frac{1}{\mu_{i,j,k}} + \frac{1}{\mu_{i,j+1,k}} + \frac{1}{\mu_{i,j,k+1}} + \frac{1}{\mu_{i,j+1,k+1}}\right)\right]^{-1}, \\
\langle\mu\rangle_{zx} &= \left[\frac{1}{4}\left(\frac{1}{\mu_{i,j,k}} + \frac{1}{\mu_{i+1,j,k}} + \frac{1}{\mu_{i,j,k+1}} + \frac{1}{\mu_{i+1,j,k+1}}\right)\right]^{-1}.
\end{aligned} \tag{17}$$

In the above equations, $\langle\mu\rangle_{xy}$, $\langle\mu\rangle_{yz}$, and $\langle\mu\rangle_{zx}$ represent the μ values at the positions of the shear stress tensor components σ_{xy}, σ_{yz}, and σ_{zx} respectively, as indicated in Figure 11(b).

2.4.4. FDM equations. By incorporating the parameter averaging method, the FDM resulting equations are:

$$\begin{aligned} D_t^- v_x &= b_x \left(D_x^+ \sigma_{xx} + D_y^- \sigma_{xy} + D_z^- \sigma_{zx} \right), \\ D_t^- v_y &= b_y \left(D_x^- \sigma_{xy} + D_y^+ \sigma_{yy} + D_z^- \sigma_{yz} \right), \\ D_t^- v_z &= b_z \left(D_x^- \sigma_{zx} + D_y^- \sigma_{yz} + D_z^+ \sigma_{zz} \right), \end{aligned} \tag{18}$$

and,

$$\begin{aligned} D_t^+ \sigma_{xx} &= (\lambda + 2\mu) D_x^- v_x + \lambda D_y^- v_y + \lambda D_z^- v_z, \\ D_t^+ \sigma_{yy} &= \lambda D_x^- v_x + (\lambda + 2\mu) D_y^- v_y + \lambda D_z^- v_z, \\ D_t^+ \sigma_{zz} &= \lambda D_x^- v_x + \lambda D_y^- v_y + (\lambda + 2\mu) D_z^- v_z, \\ D_t^+ \sigma_{xy} &= \langle \mu \rangle_{xy} \left(D_x^+ v_y + D_y^+ v_x \right), \\ D_t^+ \sigma_{yz} &= \langle \mu \rangle_{xy} \left(D_y^+ v_z + D_z^+ v_y \right), \\ D_t^+ \sigma_{zx} &= \langle \mu \rangle_{xy} \left(D_z^+ v_x + D_x^+ v_z \right), \end{aligned} \tag{19}$$

where D_i^+ and D_i^- are the forward and backward differencing operators with respect to the variable $i = \{x, y, z, t\}$. These operators depend on the order of approximation N of the stencil. For example, operator D_x^+ and D_x^- are defined as:

$$
\begin{aligned}
D_x^+ p_{i,j,k}^n =& \frac{1}{\Delta x} \sum_{\alpha=0}^{N/2-1} W_\alpha \left(p_{i+\alpha+1,j,k}^n - p_{i-\alpha,j,k}^n \right), \\
D_x^- p_{i,j,k}^n =& \frac{1}{\Delta x} \sum_{\alpha=0}^{N/2-1} W_\alpha \left(p_{i+\alpha,j,k}^n - p_{i-\alpha-1,j,k}^n \right).
\end{aligned} \tag{20}
$$

Similar definitions are used for D_y^+, D_y^-, D_z^+ and D_z^-. The coefficients W_α depends on the order of approximation of the staggered-grid scheme. For the case of fourth-order approximation ($N = 4$), $\mathbf{W} = \left[\frac{9}{8}, -\frac{1}{24}\right]$

Conversely, time differencing operators with second order of approximation are defined as:

$$
\begin{aligned}
D_t^+ p_{i,j,k}^n =& \frac{1}{2\Delta t} \left(p_{i,j,k}^{n+1/2} - p_{i,j,k}^{n-1/2} \right), \\
D_t^- p_{i,j,k}^n =& \frac{1}{2\Delta t} \left(p_{i,j,k}^n - p_{i,j,k}^{n-1} \right),
\end{aligned} \tag{21}
$$

where Δt is the time step.

2.4.5. Numerical accuracy and stability . The accuracy and stability of numerical solutions obtained through the FDM significantly depend on the spatial step size $(\Delta x, \Delta y, \Delta z)$. Generally, a smaller step size is associated with a more accurate approximation of the differential equation. For a uniform grid, the step size is consistent in all directions and is denoted by Δh. This step size is commonly determined based on the number of points N_λ per minimum wavelength $\lambda_{\min}$ that propagates through the medium, and is given by:

$$\Delta h = \frac{\lambda_{\min}}{N_\lambda} = \frac{V_{\min}}{f_{\max} N_\lambda}, \tag{22}$$

In this equation, $f_{\max}$ signifies the maximum frequency used in the simulation, which is typically set by the source, and $V_{\min}$ represents the minimum propagation velocity in the model, which is usually dictated by the smallest S-wave velocity. It is critical to choose an appropriate N_λ to maintain accuracy. In the context of the Parameter Modified (PM) method, selecting $N_\lambda = 15$ has been found to yield accuracy levels comparable to those obtained using the SPECFEM3D method (Cao and Chen, 2018). The specifics of the PM method will be explored in section 2.5.

The choice of step size also influences the stability of the numerical solution of the FDM. If the step size is too large, the numerical solution may become unstable and not converge to the correct solution. This is often regulated by the CFL (Courant-Friedrichs-Lewy) condition, which imposes a certain relationship between the spatial step size and the time step size for stability LeVeque (2007). Following the criterion presented by Lines et al. (1999), the stability of the staggered-grid scheme is ensured when the time step Δt is less than a certain limit $\Delta t_{\lim}$ given by:

$$\Delta t_{\lim} = \frac{1}{2V_{max} \sum_\alpha |W_\alpha| \sqrt{\frac{1}{(\Delta x)^2} + \frac{1}{(\Delta y)^2} + \frac{1}{(\Delta z)^2}}}. \tag{23}$$

During simulations, the time step is selected to be $\Delta t = \kappa \Delta t_{\lim}$, where $\kappa = 0.99$ as a

safety factor to ensure stability (Cao and Chen, 2018).

2.4.6. Model expansion and absorbing boundary conditions. The numerical simulations often involves finite model space. Therefore, Absorbing Boundary Conditions (ABC) are necessary to prevent artificial reflections from the boundaries of the computational domain. The most common ABC methods employed in wave modeling include the sponge ABC, Clayton-Enquist boundary condition, and the Perfectly Matched Layers (PMLs). The sponge ABC, introduced by Cerjan et al. (1985), is the simplest method and requires the least computational resources. Despite its simplicity, its performance is less effective compared to other methods. The Clayton-Enquist boundary condition, proposed by Clayton and Engquist (1977); Engquist and Majda (1977), offers a more effective performance than the sponge ABC. It is particularly beneficial for high-frequency waves and waves incident at steep angles. However, this method requires more computational resources than the sponge ABC, as it relies on a one-sided derivative approximation. Finally, PMLs provide superior absorption performance, even for waves with grazing incidence (Berenger, 1994; Collino and Tsogka, 2001; Komatitsch and Martin, 2007). However, they demand the most computational resources and memory among the three methods, especially in 3D simulations. In the proposed solver, the sponge ABC was chosen due to its straightforward implementation. However, further enhancements could potentially be achieved by incorporating PMLs into the implementation.

The first step in integrating ABCs is to expand the model, creating a specific region where the ABCs can operate. This process increases the dimensions of the grid points in the

model. Specifically, if the original model dimensions are (N_x^0, N_y^0, N_z^0), after expansion they become (N_x, N_y, N_z). As illustrated in Figure 12, the new dimensions are determined as:

$$N_x = N_x^0 + 2N_b, \quad N_y = N_y^0 + 2N_b, \quad N_z = N_z^0 + N_b, \tag{24}$$

where N_b is the number of points in each boundary layer, typically chosen between 20 and 30 points (Yang, 2014). In this implementation, note that the ABCs are not applied to the top of the model (Figure 12). This is because free-surface conditions are implemented at the top of the model.

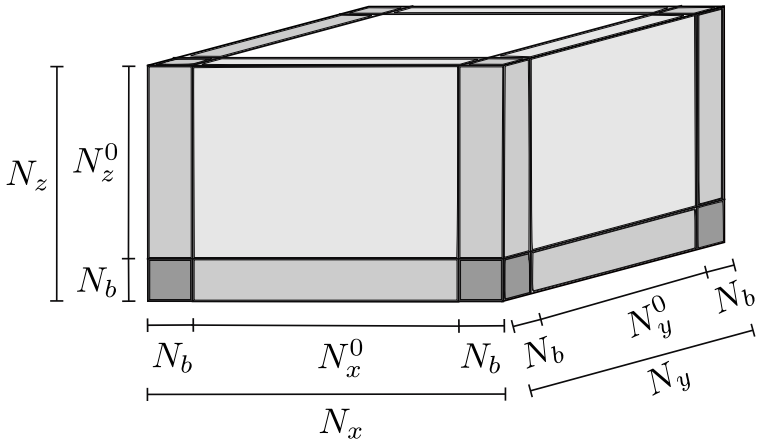

Figure 12. Model expansion to apply ABCs. The gray areas correspond to boundary region Ω_b.

The expanded model is achieved by resizing each parameter $m = \rho, \lambda, \mu$ as:

$$m_{i,j,k} = m^0_{i-N_b, j-N_b, k} \quad \forall (i,j,k) \notin \Omega_b, \tag{25}$$

where m^0 represents each parameter with the original dimensions (N_x^0, N_y^0, N_z^0), and

Ω_b denotes the boundary region defined as:

$$\Omega_b : \{(i,j,k) \in \mathbb{N}_0^3 | N_x^0 + N_b - 1 \leq i < N_b, N_y^0 + N_b - 1 \leq j < N_b, k < N_z^0\}. \tag{26}$$

Inside the boundary region, the values of the parameters are subsequently set according to:

$$m_{i,j,k} = \begin{cases} m_{0,0,k} & \text{if } i < N_b, j < N_b, \text{ and } k < N_z - N_b, \\ m_{N_x - N_b - 1,0,k} & \text{if } i > N_x - N_b - 1, j < N_b, \text{ and } k < N_z - N_b, \\ m_{0,N_y - N_b - 1,k} & \text{if } i < N_b, j > N_y - N_b - 1, \text{ and } k < N_z - N_b, \\ m_{N_x - N_b - 1, N_y - N_b - 1,k} & \text{if } i > N_x - N_b - 1, j > N_y - N_b - 1, \text{ and } k < N_z - N_b, \\ m_{i,j,N_z - N_b - 1} & \text{if } k > N_z - N_b - 1, \end{cases} \tag{27}$$

Finally, sponge ABCs are incorporated by gradually decreasing the amplitude of each variable $p = v_i, \sigma_{ij}$. This is done by multiplying each variable with a damping function within the boundary region as:

$$p_{i,j,k}^n = p_{i,j,k}^n D(i,j,k) \quad \forall (i,j,k) \in \Omega_b, \tag{28}$$

where

$$D(i,j,k) = \exp(-\alpha \left[(N_b - i)^2 + (N_b - j)^2 + (N_b - k)^2\right]), \tag{29}$$

is the damping function with a damping factor of α, typically set around 0.015 (Yang, 2014). This function ensures a gradual reduction of wave amplitudes as they approach the boundary, performing absorption and preventing reflections.

2.4.7. Source wavelet. The simulation of wave propagation necessitates the use of a source wavelet, which is a function representing the initial disturbance generating the wave motion through a medium. In seismic simulations, the most commonly used source is the Ricker function, defined as follows (Ricker, 1953):

$$w(t) = \left(1 - 2\pi^2 f_p^2 (t - t_0)^2\right) e^{-\pi^2 f_p^2 (t-t_0)^2} \tag{30}$$

where f_p is the peak frequency and t_0 is a delay parameter usually chosen to be $t_0 = 1/f_p$. As depicted in Figure 13, this wavelet has a waveform that is symmetric about a peak, and its spectral content is concentrated around the frequency f_p.

Commonly, the wavelet is inserted at a single point (the source location) in the numerical grid for some of the variables v_i, σ_{ij} (Moczo et al., 2014). The wave equation is subsequently solved to simulate the wavefield propagation from the source. When simulating explosive sources, the normal stress components are updated at every time step according to:

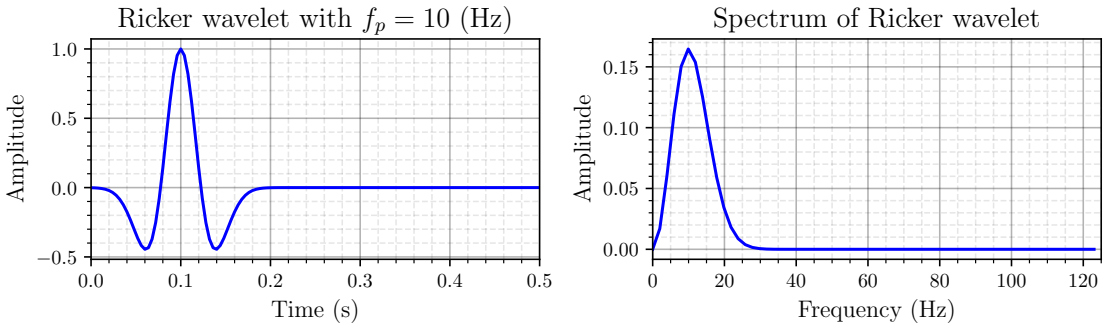

Figure 13. Ricker wavelet with 10 Hz of peak frequency (left) and its spectrum (right).

$$\sigma_{ii}^{n}(s_x, s_y, s_z) = \sigma_{ii}^{n}(s_x, s_y, s_z) + w(n\Delta t) \quad \text{for } i = \{x, y, z\} \tag{31}$$

where (s_x, s_y, s_z) denotes the source location coordinates. By using equation (31) to inject the source into a homogeneous medium, only compressional P-waves are generated.

It is important to note that the choice of source wavelet and its implementation method can significantly affect the accuracy and stability of FDM simulations. Specifically, the source wavelet sets the bandwidth of the frequencies to be simulated, thereby influencing the spatial step size according to equation (22). Although the Ricker wavelet theoretically contains frequencies up to infinity, the practical frequency range it covers leads to a modification of equation (22) for the case of the Ricker wavelet as follows (Sun et al., 2019):

$$\Delta h = \frac{V_{\min}}{2.5 f_p N_\lambda}. \tag{32}$$

2.5. The parameter modified method for free surface condition

The inclusion of the free surface condition is the most challenging part when modeling elastic waves in media with irregular topography using FDM. This condition states that the stress component normal to the surface is set of zero Moczo et al. (2014). In mathematical terms, the free-surface boundary condition for stress is often written as:

$$\sigma_{ij} n_j = 0, \tag{33}$$

where σ_{ij} is the stress tensor, and n_j is the outward normal vector at the surface topography. For a 3D problem, considering the surface as the plane $z = 0$, this condition simplifies to:

$$\sigma_{zz} = \sigma_{xz} = \sigma_{yz} = 0. \tag{34}$$

However, implementing the free-surface condition in FDM simulations involving scenarios with irregular topography brings with it several complexities. Specifically, staircase-shaped discretization is employed to approximate irregular surfaces. This, however, introduces artificial discontinuities that can lead to wave scattering and the generation of spurious reflections. These artifacts can significantly affect the accuracy of the wavefield simulation. To address this issue, various strategies have been explored, including the vacuum formulation (Zahradník et al., 1993; Bohlen and Saenger, 2006), the stress-image method (Levander, 1988; Robertsson, 1996; Hayashi et al., 2001), and medium averaging methods (Mittet, 2002; Xu et al., 2007; Zeng et al., 2012; Cao and Chen, 2018). Among these, the parameter mo-

dified (PM) method proposed by Cao and Chen (2018) stands out. It has demonstrated accuracy levels comparable to those achieved by SPECFEM3D. For this reason, this method was implemented within the proposed solver to satisfy the free-surface condition in arbitrary irregular topography.

The Parameter Modified (PM) method involves adjusting the constitutive relation for the horizontal boundary. With the application of matrix rotations, different constitutive relations emerge for various cases. A more detailed exploration of the theory behind the method can be found in (Cao and Chen, 2018).

In practical terms, the method categorizes the grid cells on the surface based on their relative position to the air. There are five basic classes:

- H: grid cell with air above,
- VR: grid cell with air to the right,
- VL: grid cell with air to the left
- VF: grid cell with air to the front
- VB: grid cell with air to the back

In addition to these basic classes, some transition cells such as inner and outer corner points also exist. An example of the point classification for the $x - z$ plane is depicted in Figure 14.

To facilitate the implementation of PM method, Cao and Chen (2018) put forth generalized expressions for FDM in interior and surface grid cells as:

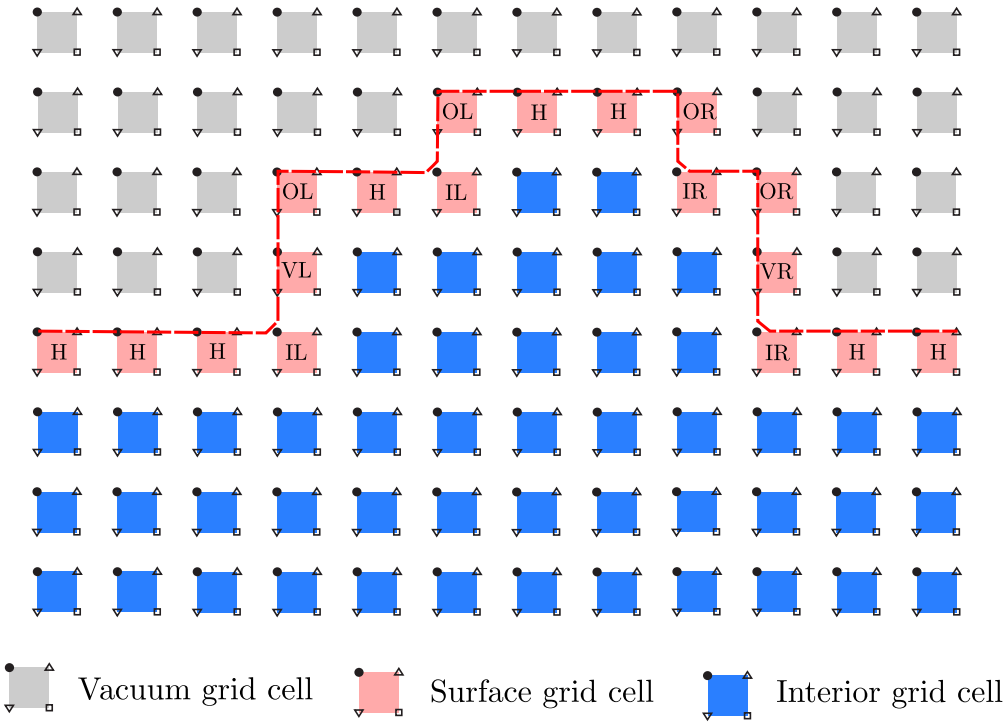

Figure 14. Grid cell classification for PM method. In this illustration only the $x-z$ plane is shown. IL: interior left point, IR: interior right point, OL: outer left point, OR: outer right point.

$$
\begin{aligned}
D_t^- v_x &= \tilde{b}_x \left(D_x^+ \sigma_{xx} + D_y^- \sigma_{xy} + D_z^- \sigma_{zx} \right), \\
D_t^- v_y &= \tilde{b}_y \left(D_x^- \sigma_{xy} + D_y^+ \sigma_{yy} + D_z^- \sigma_{yz} \right), \\
D_t^- v_z &= \tilde{b}_z \left(D_x^- \sigma_{zx} + D_y^- \sigma_{yz} + D_z^+ \sigma_{zz} \right),
\end{aligned}
\tag{35}
$$

and

$$
\begin{aligned}
D_t^+\sigma_{xx} &= \eta_1^{xx} D_x^- v_x + \eta_2^{xx} D_y^- v_y + \eta_3^{xx} D_z^- v_z, \\
D_t^+\sigma_{yy} &= \eta_1^{yy} D_x^- v_x + \eta_2^{yy} D_y^- v_y + \eta_3^{yy} D_z^- v_z, \\
D_t^+\sigma_{zz} &= \eta_1^{zz} D_x^- v_x + \eta_2^{zz} D_y^- v_y + \eta_3^{zz} D_z^- v_z, \\
D_t^+\sigma_{xy} &= \langle\tilde{\mu}\rangle_{xy} \left(D_x^+ v_y + D_y^+ v_x\right), \\
D_t^+\sigma_{yz} &= \langle\tilde{\mu}\rangle_{xy} \left(D_y^+ v_z + D_z^+ v_y\right), \\
D_t^+\sigma_{zx} &= \langle\tilde{\mu}\rangle_{xy} \left(D_z^+ v_x + D_x^+ v_z\right).
\end{aligned}
\tag{36}
$$

The newly defined parameters in these generalized equations are assigned based on the cell classification. In interior points, the parameters are set as follows:

$$
\begin{aligned}
&\tilde{b}_x = b_x, \quad \tilde{b}_y = b_y, \quad \tilde{b}_z = b_z, \\
&\eta_1^{xx} = \eta_2^{yy} = \eta_3^{zz} = \lambda + 2\mu, \\
&\eta_2^{xx} = \eta_3^{xx} = \eta_1^{yy} = \eta_3^{yy} = \eta_1^{zz} = \eta_2^{zz} = \lambda, \\
&\langle\tilde{\mu}\rangle_{xy} = \langle\mu\rangle_{xy}, \quad \langle\tilde{\mu}\rangle_{yz} = \langle\mu\rangle_{yz}, \quad \langle\tilde{\mu}\rangle_{zx} = \langle\mu\rangle_{zx}.
\end{aligned}
\tag{37}
$$

With these values, the generalized FDM equations (35) and (36) are consistent with the original FDM equations (18) and (19).

For surface points, the parameters are adjusted according to the constitutive relation. A summary of these modifications for each specific case can be found in Table 2. In the

following section, the implementation of this method on a GPU will be explained.

Table 2
Calculation of parameters at the surface points according to grid cell classification of the PM method. OP refers to outer transition points.

Parameters	H	VR	VL	VF	VB	OP
$\tilde{b}_x$	b_x	b_x	b_x	$2b_x$	$2b_x$	$2b_x$
$\tilde{b}_y$	b_y	$2b_y$	$2b_y$	b_y	b_y	$2b_y$
$\tilde{b}_z$	$2b_z$	$2b_z$	$2b_z$	$2b_z$	$2b_z$	$2b_x$
η_1^{xx}	$\lambda+2\mu$	0	0	$\frac{2\mu(\lambda+\mu)}{\lambda+2\mu}$	$\frac{2\mu(\lambda+\mu)}{\lambda+2\mu}$	0
η_2^{xx}	λ	0	0	0	0	0
η_3^{xx}	λ	0	0	$\frac{\mu\lambda}{\lambda+2\mu}$	$\frac{\mu\lambda}{\lambda+2\mu}$	0
η_1^{yy}	λ	0	0	0	0	0
η_2^{yy}	$\lambda+2\mu$	$\frac{2\mu(\lambda+\mu)}{\lambda+2\mu}$	$\frac{2\mu(\lambda+\mu)}{\lambda+2\mu}$	0	0	0
η_3^{yy}	λ	$\frac{\mu\lambda}{\lambda+2\mu}$	$\frac{\mu\lambda}{\lambda+2\mu}$	0	0	0
η_1^{zz}	λ	0	0	$\frac{\mu\lambda}{\lambda+2\mu}$	$\frac{\mu\lambda}{\lambda+2\mu}$	0
η_2^{zz}	λ	$\frac{\mu\lambda}{\lambda+2\mu}$	$\frac{\mu\lambda}{\lambda+2\mu}$	0	0	0
η_3^{zz}	$\lambda+2\mu$	$\frac{2\mu(\lambda+\mu)}{\lambda+2\mu}$	$\frac{2\mu(\lambda+\mu)}{\lambda+2\mu}$	$\frac{2\mu(\lambda+\mu)}{\lambda+2\mu}$	$\frac{2\mu(\lambda+\mu)}{\lambda+2\mu}$	0
$\langle\tilde{\mu}\rangle_{xy}$	$\langle\mu\rangle_{xy}$	$\langle\mu\rangle_{xy}$	$\langle\mu\rangle_{xy}$	$\langle\mu\rangle_{xy}$	$\langle\mu\rangle_{xy}$	$\frac{\langle\mu\rangle_{xy}}{2}$
$\langle\tilde{\mu}\rangle_{yz}$	$\langle\mu\rangle_{yz}$	$\frac{\langle\mu\rangle_{yz}}{2}$	$\frac{\langle\mu\rangle_{yz}}{2}$	$\langle\mu\rangle_{yz}$	$\langle\mu\rangle_{yz}$	$\frac{\langle\mu\rangle_{yz}}{2}$
$\langle\tilde{\mu}\rangle_{zx}$	$\langle\mu\rangle_{zx}$	$\langle\mu\rangle_{zx}$	$\langle\mu\rangle_{zx}$	$\frac{\langle\mu\rangle_{zx}}{2}$	$\frac{\langle\mu\rangle_{zx}}{2}$	$\frac{\langle\mu\rangle_{zx}}{2}$

2.6. Implementation strategy on a GPU

The Graphics Processing Units (GPUs) are specialized electronic circuits with thousands of cores that can perform operations simultaneously, which makes them especially well-suited for tasks that can be performed in parallel. This characteristic allows for a significant speedup in FDM computations, which can be readily parallelized due to the stencil nature of finite differences. Numerous GPU implementations have been performed to solve the wave equation (Abdelkhalek et al., 2009; Micikevicius, 2009; Michéa and Komatitsch, 2010; Komatitsch et al., 2010; Nakata et al., 2011; Weiss and Shragge, 2013; Rubio et al., 2014; Fabien-Ouellet et al., 2017; Liu et al., 2018; Alkhimenkov et al., 2021). In this subsection, the implementation of the PMFD3D-GPU solver will be presented, utilizing a subdomain decomposition strategy with unstructured index array representation.

2.6.1. Subdomain decomposition. As discussed in the previous section, the PM method for FDM necessitates the recalculation of medium parameters at surface points. To facilitate the implementation of the PM method, Cao and Chen (2018) proposed generalized expressions for FDM in both interior and surface grid cells (equations (35) and (36)). However, implementing these generalized expressions on a GPU would not be efficient in terms of memory resource management. While the original FDM expressions (equations (18) and (19)) only require storing three field parameters (ρ, μ, λ), the generalized expressions necessitate the storage of fifteen field parameters $(\tilde{b}_x, \tilde{b}_y, \tilde{b}_z, \eta_1^{xx}, \eta_2^{xx}, \eta_3^{xx}, \eta_1^{yy}, \eta_2^{yy}, \eta_3^{yy}, \eta_1^{zz}, \eta_2^{zz}, \eta_3^{zz}, \langle\tilde{\mu}\rangle_{xy}, \langle\tilde{\mu}\rangle_{yz}, \langle\tilde{\mu}\rangle_{zx})$. An alternative approach

to circumvent this challenge would involve recalculating the parameter values at each step rather than saving them. However, this alternative would compromise computational efficiency since it would require the classification of each grid cell at every step.

A subdomain decomposition strategy is proposed for computing FDM simulations, effectively minimizing memory usage while maintaining high computational efficiency. The strategy involves dividing the effective domain (all grid points where medium parameters differ from zero) into two sections: the surface subdomain and the interior subdomain (Figure 15). The surface subdomain, denoted by Ω_S, includes grid cells situated at the surface. Within this domain, the generalized expressions are implemented, and the fifteen field parameters are stored. The interior subdomain, represented by Ω_I, encompasses grid cells located internally, below the surface subdomain. In this interior subdomain, the original FDM equations are implemented, and parameter averaging is conducted at each time step. By adopting this strategy, memory usage is minimized as field parameters are only saved at the surface, and computational efficiency is ensured as grid cell classification is performed just once.

Note that these subdomains do not necessarily conform to a square shape (Figure 15). As a result, additional procedures must be undertaken to manage the indices of each grid cell within each respective subdomain.

2.6.2. Unstructured index array representation. In structured grid data (such as a square or rectangle), each point in the grid can be accessed by using its row and column indices because all the rows and columns are equally spaced and organized in a regular manner. However, in unstructured or irregularly shaped grids (like the subdomains

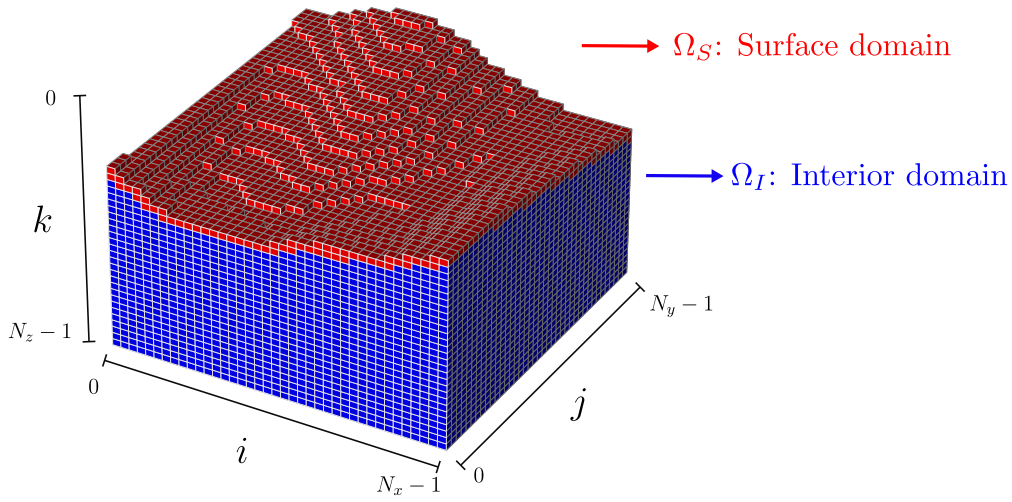

Figure 15. Subdomain decomposition based on the grid cell classification. The surface subdomain (Ω_S) is represented by red cells, while blue cells illustrate the interior subdomain (Ω_I).

in Figure 15), this regular access pattern does not exist. This can make it more difficult to perform computations and navigate through the data, especially on parallel processors like GPUs.

To address this challenge, the Unstructured Index Array Representation (UIAR) technique is introduced, enabling the representation of indices for each grid cell within subdomains of arbitrary shapes. This technique provides a structured and systematic approach to organize and access data from irregular or complex subdomains. It involves the creation of an index array that maps the irregular grid points in the subdomain to a structured format.

Specifically, the surface subdomain Ω_S, containing N_s grid cells, is represented by a one-dimensional array S. This array encapsulates the indices of the irregular subdomain in the following manner:

$$S(l) = iN_yN_z + jN_z + k, \quad \forall(i,j,k) \in \Omega_S, \tag{38}$$

Here, the index l spans from 0 to $N_S - 1$, covering all the cells within the subdomain Ω_S.

Similarly, the interior subdomain Ω_I, which includes N_I grid cells, is represented by a one-dimensional array I. This array incorporates the indices of the irregular subdomain as follows:

$$I(m) = iN_yN_z + jN_z + k, \quad \forall(i,j,k) \in \Omega_I, \tag{39}$$

In this case, the index m extends from 0 to $N_I - 1$, accounting for all cells within the subdomain Ω_I.

These one-dimensional arrays (S and I) facilitate efficient data access and manipulation within these irregularly shaped subdomains, providing a systematic representation of otherwise unstructured index data. Consequently, this method enables the effective execution of computations on GPUs. Algorithms 1 and 2 present the kernel pseudocodes for updating particle velocities and the stress tensor at the grid cells within the surface subdomain. Accordingly, algorithms 3 and 4 exhibit the kernel pseudocodes for updating particle velocities and the stress tensor at the grid cells within the interior subdomain.

2.6.3. Workflow implementation. Figure 16 presents the workflow utilized to implement the PMFD3D-GPU solver. As shown, several steps of the workflow are

Algorithm 1 Kernel for update particle velocities in Ω_S

if $l < N_S$ **then**
  $i = S[l]/(N_y N_z)$
  $j = (S[l] - iN_y N_z)/Nz$
  $k = S[l] - iN_y N_z - jNz$
  $v_x, v_y, v_z \leftarrow$ **velocitySurface**$(\sigma_{xx}, \sigma_{yy}, \sigma_{zz}, \sigma_{xy}, \sigma_{yz}, \sigma_{zx}, i, j, k)$ ▷ Equation (35)
end if

Algorithm 2 Kernel for update stress tensor in Ω_S

if $l < N_S$ **then**
  $i = S[l]/(N_y N_z)$
  $j = (S[l] - iN_y N_z)/Nz$
  $k = S[l] - iN_y N_z - jNz$
  $\sigma_{xx}, \sigma_{yy}, \sigma_{zz}, \sigma_{xy}, \sigma_{yz}, \sigma_{zx} \leftarrow$ **stressSurface**(v_x, v_y, v_z, i, j, k) ▷ Equation (36)
end if

Algorithm 3 Kernel for update particle velocities in Ω_I

if $m < N_I$ **then**
  $i = I[m]/(N_y N_z)$
  $j = (I[m] - iN_y N_z)/Nz$
  $k = I[m] - iN_y N_z - jNz$
  $v_x, v_y, v_z \leftarrow$ **velocityInterior**$(\sigma_{xx}, \sigma_{yy}, \sigma_{zz}, \sigma_{xy}, \sigma_{yz}, \sigma_{zx}, i, j, k)$ ▷ Equation (18)
end if

Algorithm 4 Kernel for update stress tensor in Ω_I

if $m < N_I$ **then**
  $i = I[m]/(N_y N_z)$
  $j = (I[m] - iN_y N_z)/Nz$
  $k = I[m] - iN_y N_z - jNz$
  $\sigma_{xx}, \sigma_{yy}, \sigma_{zz}, \sigma_{xy}, \sigma_{yz}, \sigma_{zx} \leftarrow$ **stressInterior**(v_x, v_y, v_z, i, j, k) ▷ Equation (19)
end if

executed on the CPU, including model expansion, domain decomposition, and the calculation of medium parameters in the surface subdomain. Subsequently, the GPU is set up, and model data is transferred from the CPU to the GPU. Once this transfer is complete, the GPU conducts the FDM computations for both the surface and interior subdomains. These computations includes updating the particle velocities and stress tensor components, injecting the source, and applying the Absorbing Boundary Conditions (ABCs). Following these computations, the resulting receiver data are transferred back to the CPU and subsequently written to disk. This procedure is repeated until all time steps are completed.

2.7. Numerical tests

In this section, we asses the efficiency and accuracy of PMFD3D-GPU through two distinct numerical tests. The first test involves a direct comparison of accuracy with SPECFEM 3D. The second test demonstrates the capability of PMFD3D-GPU to generate realistic synthetic data within a portion of the SEAM Foothills Phase II model. Additionally, the computational performance of PMFD3D-GPU is evaluated during these tests.

2.7.1. Accuracy validation with SPECFEM3D. In this test, the accuracy of PMFD3D-GPU is validated by performing elastic wave modeling in a homogeneous model with rough topography. Both PMFD3D-GPU and SPECFEM3D are used for comparison, and the synthetic data obtained from each method is subsequently analyzed and compared.

The homogeneous model, with dimensions and medium parameters as specified in Table 3, is uniformly discretized in all directions with a spacing of $\Delta h = 5$ m. The irregular

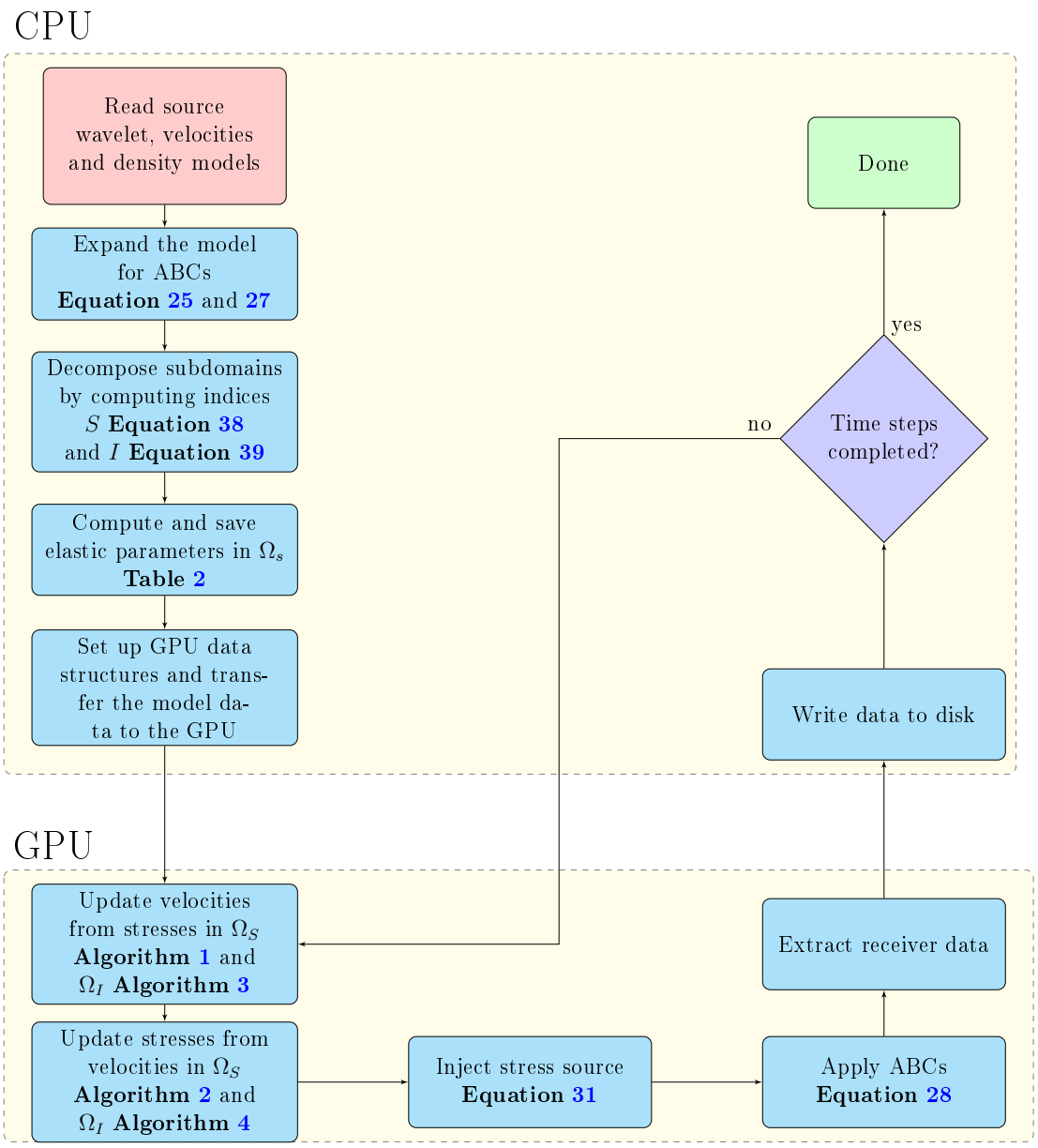

Figure 16. Workflow used to implement the PMFD3D-GPU solver.

topography is generated using the elevation map function $T(x, y)$, defined as:

$$T(x,y) = 350 + 250 \sin\left(\frac{x}{1000}\right) \cos\left(\frac{y}{1000}\right) \tag{40}$$

This function was then corrupted with normally distributed random noise and subsequently smoothed using a repeated triangle filter, applied over 40 points on each axis. The resulting elevation map can be observed in Figure 17.

Table 3
Medium parameters for homogeneous model.

V_P (m/s)	V_S (m/s)	ρ (Mg/m^3)	V_P/V_S	Dimension (m)	Grid cell size (m)
3550	2050	2.0	3.5	$3000 \times 2000 \times 2000$	$5 \times 5 \times 5$

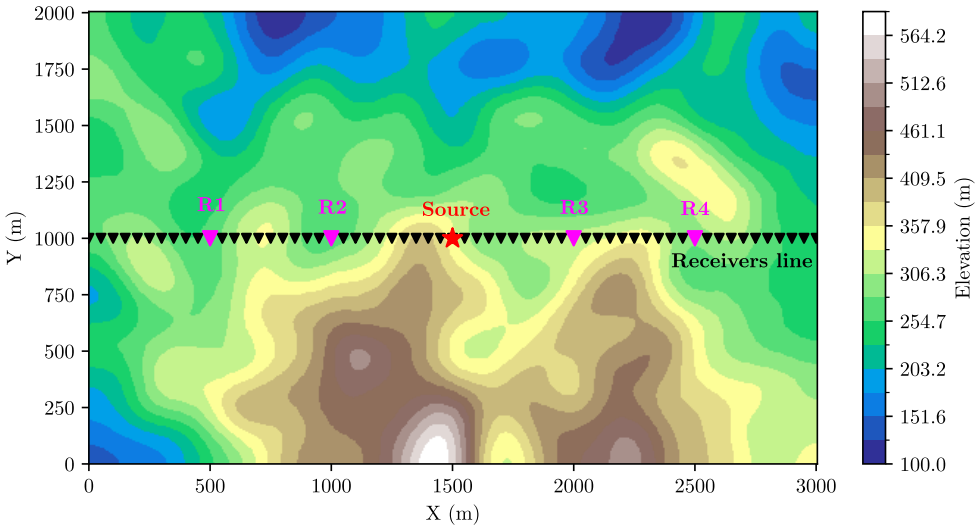

Figure 17. Elevation map and acquisition geometry. The source is situated at coordinates (1500,1000) m, 20 m beneath the surface. 3C receivers are placed along the surface at Y=1000 m, in a line from 0 to 3000 m, spaced every 10 m. Key receivers R1, R2, R3, and R4 are located at X= 500 m, 1000 m, 2000 m, and 2500 m; respectively.

For synthetic seismic data generation, an acquisition geometry was established with a line of 301 receivers, deployed at intervals of 10 m along the x-axis at $Y = 1000$ m, as shown in Figure 17. Additionally, an explosive Ricker source with a peak frequency of 10 Hz was positioned at the coordinates (1500,1000) m, at a depth of 20 m.

To conduct modeling with SPECFEM3D, the solver required an initial setup that specified the number of spectral elements for the simulation. For this test, the solver was set to use $96 \times 72 \times 40$ elements to represent the model. SPECFEM3D included an internal mesher, XMESHFEM3D, which accurately organized the geometry of the elements to cover the irregular surface. The resulting mesh for the current model is depicted in Figure 18.

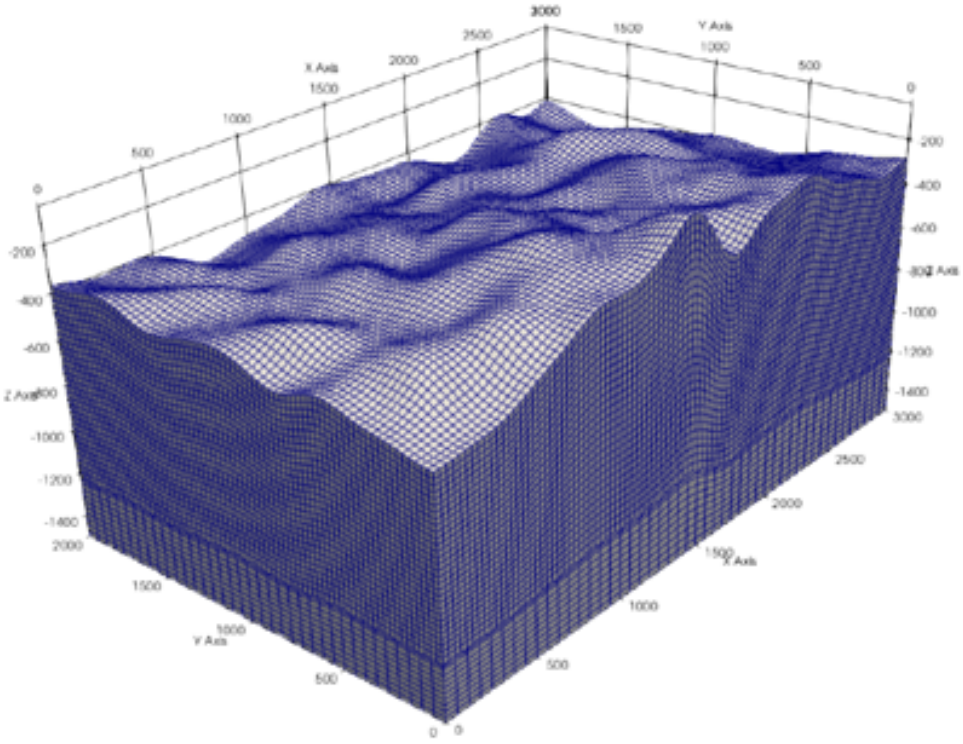

Figure 18. Mesh produced by XMESHFEM3D, the internal mesher of SPECFEM3D, utilizing $96 \times 72 \times 40$ elements to represent the model corresponding to the elevation map shown in Figure 17.

Simulations were conducted for 1.5 seconds using both solvers. The resulting multi-component shot gathers, obtained from SPECFEM3D and PMFD3D-GPU, are shown in Figures 19(a) and 19(b), respectively. A comparison reveals that the differences between the

shots are minimal around the source position and gradually increase as we move away from it, as depicted in Figure 19(c).

To conduct a further comparison between the methods, traces were extracted from four receivers along the receiver line. The receivers, denoted as R1, R2, R3, and R4, are positioned at distances of 500 m, 1000 m, 2000 m, and 2500 m along the x-axis, as depicted in Figure 17. The normalized seismic traces for each receiver, obtained from both solvers, are shown in Figure 20. Visually, the traces appear identical across all components and receivers.

For a more quantitative comparison, the L_2 misfit error was computed between the shot gathers obtained from PMFD3D-GPU and SPECFEM3D, using the following formula:

$$L_2 = \frac{\|\mathbf{u} - \mathbf{u}^0\|^2}{\|\mathbf{u}^0\|^2}, \tag{41}$$

where $\mathbf{u}^0$ denotes the shot gather computed by SPECFEM3D, and $\mathbf{u}$ represents the shot gather computed by PMFD3D-GPU. The calculated error percentages for each component from each receiver are presented in Table 4. From these results, it's clear that most of the errors were under 1 %. Notably, higher errors were detected in receivers R1 and R4, which are situated furthest from the source. Particularly these errors are more prominent in the horizontal components (along the $x-$ and $y-$axes).

2.7.2. 3D SEAM Foothills model example. In this example, realistic seismic synthetic data was generated by conducting elastic wave modeling in a selected portion of the SEAM Foothills Phase II model using PMFD3D-GPU. The chosen portion

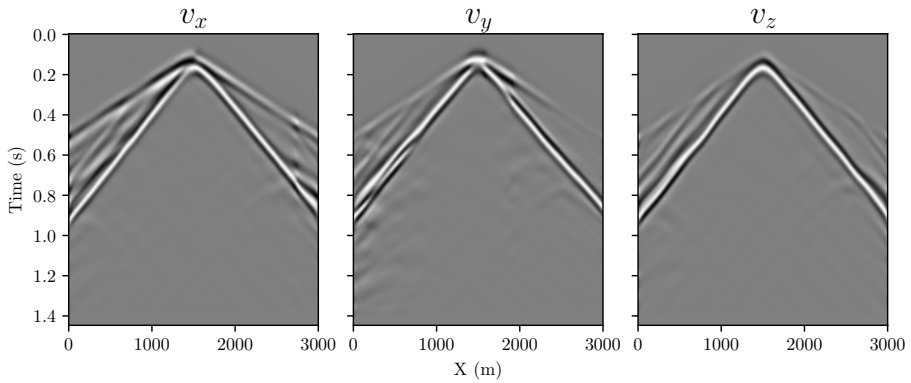

(a)

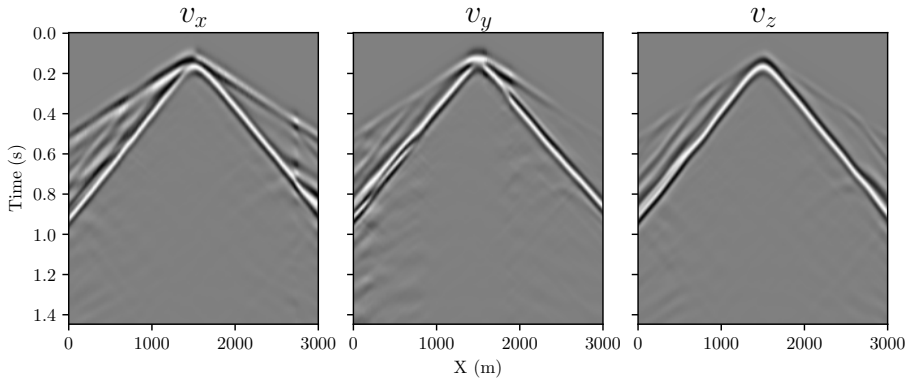

(b)

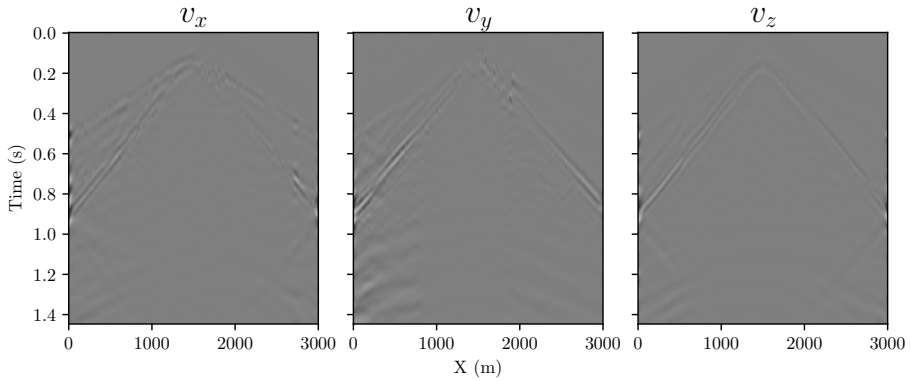

(c)

Figure 19. Multicomponent shot gather. (a) SPECFEM3D. (b) PMFD3D-GPU. (c) Difference between (a) and (b).

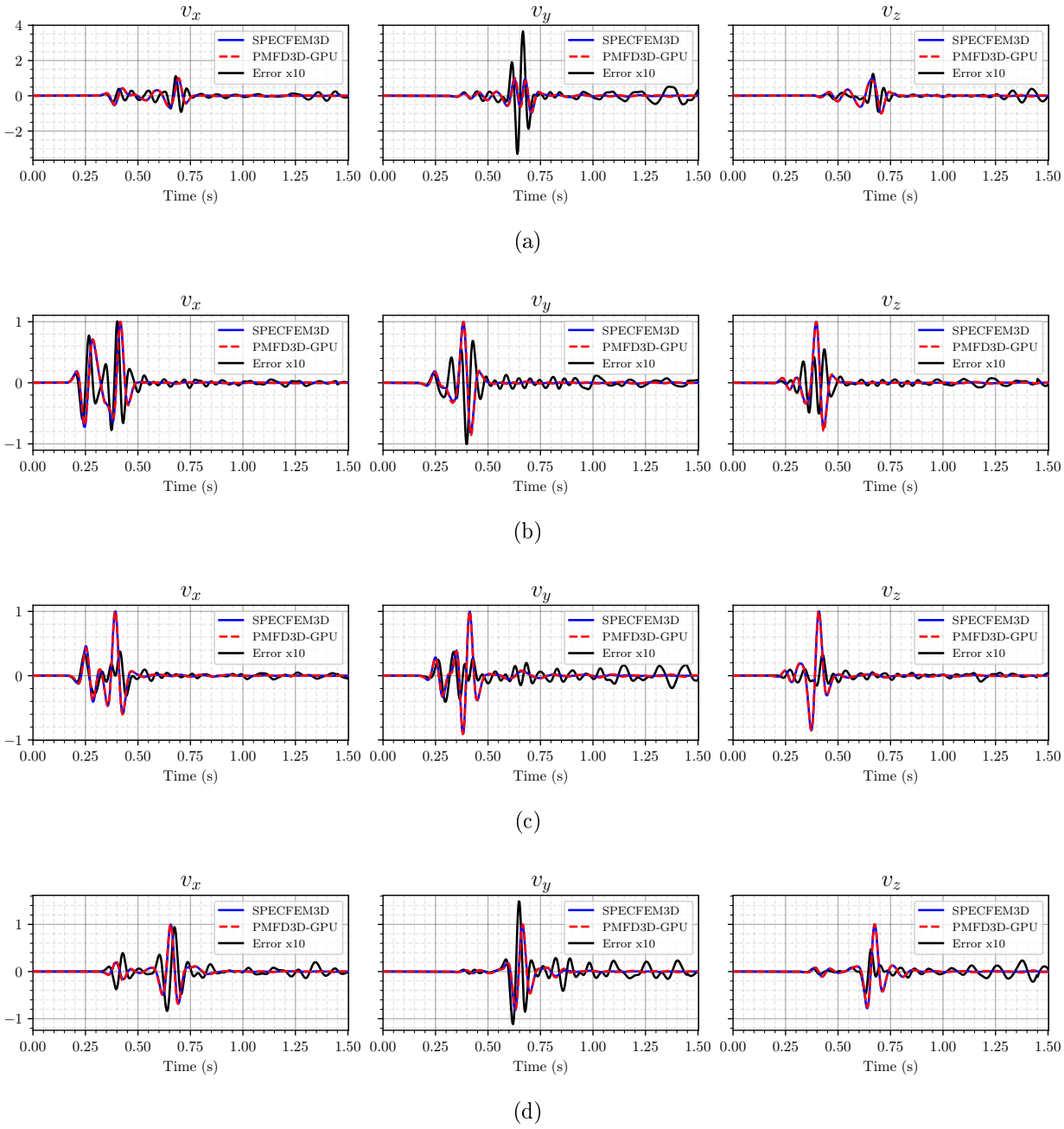

Figure 20. Normalized Seismic Traces Comparison Using SPEFEM3D and PMFM3D-GPU Methods. (a) R1 at $x = 50$ m, (b) R2 at $x = 100$ m, (c) R3 at $x = 200$ m, and (d) R4 at $x = 250$ m. Solutions from SPEFEM3D are solid blue lines, and PMFM3D-GPU solutions are red dashed lines. Black lines represent the difference error multiplied by 10.

Table 4
L_2 misfit norm error of the PMFD3D method compared to the SPECFEM3D method for receivers R1, R2, R3, and R4.

Receiver	v_x (%)	v_y (%)	v_z (%)
R1	1.15	7.77	0.80
R2	0.88	0.97	0.51
R3	0.27	0.42	0.11
R4	1.24	2.25	0.37

measures 6000 m × 2000 × 4400 m and is discretized uniformly with a spacing of $\Delta h = 10$ m across all axes. The topographic elevation map for this selected segment is illustrated in Figure 21.

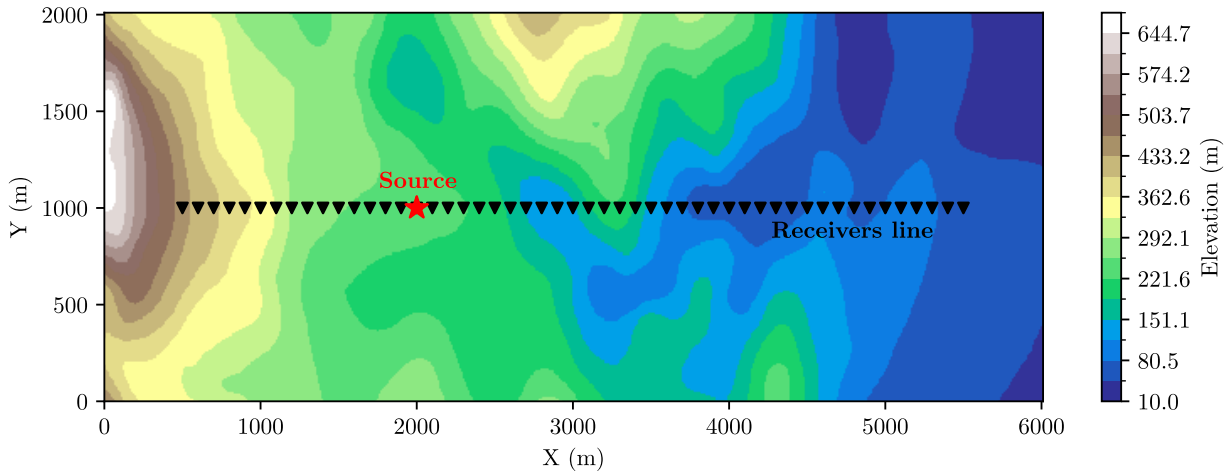

Figure 21. Elevation map and acquisition geometry for the portion of the SEAM model. The source is positioned at coordinates (200,1000) m, with a depth of 12 m. 3C receivers are aligned on the surface line from 500 to 5500 m at Y=1000 m, with an inter-receiver spacing of 10 m.

For the acquisition geometry, receivers were placed on the surface along a line spanning from 500 to 5500 m at Y=1000 m, with an inter-receiver distance of 10 m (as seen in Figure 21). Additionally, an explosive source was positioned at coordinates (200,1000) m, at a depth

of 12 m. The synthetic data was generated by applying PMFD3D-GPU with 4 seconds of simulation. The resultant multicomponent shot gather is displayed in Figure 22. Here, realistic seismic events such as Rayleigh waves, near-surface refractions, and near-surface scattering can be observed. This result demonstrates the capability of PMFD3D-GPU in handling elastic wave modeling in complex geological settings.

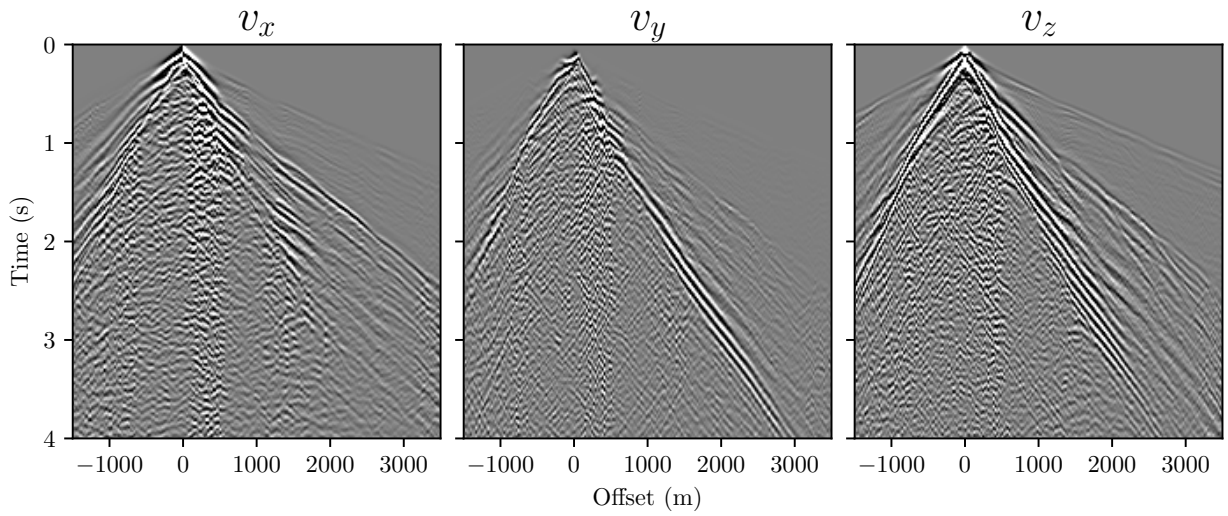

Figure 22. Multicomponet shot gather SEAM with PMFD3D-GPU.

2.7.3. Computational performance. The numerical examples presented show that PMFD3D-GPU can perform accurate elastic wave simulations in heterogeneous media. However, the strengths of PMFD3D-GPU extend beyond just accuracy, as it also offers significant computational efficiency. A comprehensive performance analysis, as detailed in Table 5, showcases the time consumption of PMFD3D-GPU in comparison to the C CPU version with OpenMP across various 3D models. When comparing the time spent by PMFD3D-CPU on a uniform grid with that of PMFD3D-GPU on the SEAM model, the

GPU implementation is found to be approximately 20 times faster.

Table 5
Comparative analysis of computational performance between the PMFD3D solver implemented on a CPU and the proposed GPU-accelerated implementation (PMFD3D-GPU).

CPU: Intel Core i7-12700 processor, 12 Core, 2.1GHz to 4.9GHz, 16GB of memory using C and OpenMP
GPU: NVIDIA GeForce RTX 3060 12 GB of memory using CUDA-C

Model	Dimension ($N_x \times N_y \times N_z$)	Time samples	CPU Comp. time (min)	GPU Comp. time (min)
Homogeneous topography	$(681 \times 481 \times 340)$ $410,341$ surface points $86,335,041$ interior points	2256	115.65	5.47
SEAM portion	$(641 \times 241 \times 461)$ $177,235$ surface points $56,195,513$ interior points	5003	166.61	7.53

2.8. Discussion

Numerical modeling of elastic waves in 3D complex media is a computationally demanding task. While many numerical methods are available for undertaking this task, each invariably faces a trade-off between accuracy and computational efficiency, regardless of the chosen method. Within this context, PMFD3D-GPU has proven to be a suitable solver, providing high accuracy results in a relatively short execution time. The GPU-accelerated with CUDA-C implementation strategy significantly speeds up the simulation of the PM method, widely outpacing the CPU implementation. Furthermore, the solver proposed in this chapter reached accuracy levels comparable to those achieved by SPECFEM3D in the rough topography medium test.

Contrasted with existing solvers, PMFD3D-GPU fills the gap for open-source solvers that are capable of propagating elastic waves in heterogeneous media featuring irregular topography. While useful alternatives do exist, they typically demand additional efforts for application in complex scenarios. For instance, SPECFEM3D is capable of simulating elastic wave propagation with high accuracy, but its internal mesher is not designed to handle arbitrary heterogeneous models. This limitation necessitates the use of external meshers, which could potentially lead to license fees. In contrast, the proposed solver can be effortlessly applied in any scenario without incurring extra costs or efforts.

Although PMFD3D-GPU brings significant benefits, there is scope for further enhancements in various aspects. Currently, sponge absorbing boundary conditions (ABCs) have been implemented due to their ease of implementation and minimal computational resource requirements. However, perfectly matched layers (PMLs) outperform sponge ABCs in terms of absorption performance, and including them would increase the accuracy of the proposed solver. Implementing PMLs can be computationally expensive in terms of memory as they necessitate the storage of multiple auxiliary fields. However, PML memory allocation strategies as proposed by Páez et al. (2020) could be employed to reduce the memory requirements for simulations. In terms of computational execution time, further reduction could potentially be achieved by adopting a shared memory strategy in the GPU kernel implementation instead of the currently used global memory strategy. Shared memory strategy has been empirically proven to offer much lower latency than global memory owing to its proximity to the cores and its smaller size, as outlined by Cheng et al. (2014). These potential

improvements highlight the ongoing possibilities for optimization and increased efficiency in GPU-accelerated numerical modeling.

2.9. Conclusions

This chapter presented PMFD3D-GPU, a finite-difference solver designed for 3D elastic wave modeling in heterogeneous models with irregular topography. The solver utilizes a GPU implementation strategy, incorporating the parameter modified method to satisfy the free-surface condition for varying topographic elevation maps. A subdomain decomposition method with an unstructured index array representation was employed to efficiently manage grid cell indices within irregular subdomains, resulting in improved computational efficiency. The accuracy of PMFD3D-GPU was validated through numerical testing using a variable topography model, demonstrating results comparable to those from SPECFEM3D. The solver successfully generated realistic seismic synthetic data, as evidenced in an exercise using the SEAM Foothills Phase II model. Moreover, PMFD3D-GPU achieved a significant speedup compared to the CPU implementation of the PMFD3D method. Potential improvements were also discussed, including the application of PMLs to enhance absorption in the ABCs and the utilization of a shared memory strategy to further reduce computational execution time.

CHAPTER 3. Numerical modeling of near-surface seismic scattering by the partitioned domain method

3.1. Abstract

Accurate modeling of near-surface seismic scattering (NSS) is crucial for reducing noise and enhancing the quality and interpretability of seismic data. This process enables the identification of specific characteristics of NSS, leading to the development of more effective techniques to attenuate it. While various methods have been developed to model NSS from elastic wave forward modeling, they often present constraints in considering complex overburdens with substantial topographic variations or random heterogeneous media. To address these limitations, the partitioned domain method (PDM) is introduced in this chapter. The method involves two stages of elastic wave modeling to generate synthetic seismic data with and without NSS. The first stage uses the entire earth model to generate the total wavefield (TW), encompassing all seismic wave types. The second stage employs the near-surface portion of the earth model to yield the near-surface wavefield (NW), inclusive of direct waves, Rayleigh waves, and NSS. A deep wavefield (DW), comprising body wave reflections and refractions from deeper structures, is then derived by subtracting the NW from the TW. To study the performance of the proposed method, a numerical example using the SEAM Foothills Phase II model is conducted. In this example, elastic wave modeling is performed with the PMFD3D-GPU solver presented in Chapter 2. The results demonstrate that the method can effectively model NSS, enhancing the understanding of land seismic noise and

facilitating the development of new attenuation techniques.

3.2. Introduction

The near-surface is the space immediately below the free-surface of the earth. This space is approximately 300 meters deep within the scale of exploration seismology and is composed of a soil column and low-velocity, unconsolidated, heterogeneous, and weathered layers of rock Yilmaz (2015). These characteristics makes the acquired seismic data in complex land areas have near-surface scattering (NSS) that mask the desired body-waves reflections. This unwanted energy represents the most challenging noise in land seismic data processing as conventional processing techniques, like $f-k$ filters, struggle to effectively characterize and eliminate it. Therefore, modeling NSS has emerged as a crucial step in understanding how seismic waves propagate and scatter upon encountering near-surface heterogeneities. This task is typically accomplished by modeling elastic wave scattering.

Several methods for modeling elastic wave scattering have been proposed, broadly falling into two categories: analytical and numerical approaches. The analytical approach often relies on the first Born approximation for calculating single scattering. Within this approach, perturbation methods have been extensively studied and applied in numerous investigations (Hudson, 1967; Wu and Aki, 1985; Wu, 1989; Beylkin and Burridge, 1990; Maeda et al., 2008; Sato et al., 2012). Additionally, the asymptotic method is another technique within the analytical approach (Snieder, 1986; Blonk and Herman, 1994). While these methods have enhanced the understanding of scattering behavior, they exhibit limitations, especially when addressing large and high-contrast heterogeneities that violate the first Born

(single-scattering) approximation.

In contrast, numerical approaches are capable of solving the full wave equation, offering an advantage when dealing with more complex background media, significant contrasts in medium parameters, and irregular interfaces. Moreover, they can generate synthetic seismograms with high accuracy over a wide range of wavelength ratios. Within this approach, the finite-difference method proposed by Robertsson and Chapman (2000) provides an efficient way to model scattering. However, it does not account for the interaction of the scattered wavefield with the free surface and bedrock layers. An alternative numerical method, the integral equation method with elastic wave numerical modeling using the moments method (Riyanti and Herman, 2005; Campman and Dwi Riyanti, 2007), not only models multiple scattering but can also handle strong contrast and large heterogeneities. Despite these strengths, the method's applicability is constrained to laterally homogeneous embedding consisting of horizontal layers, a situation often absent in areas with complex overburden. More recently, Almuhaidib and Toksöz (2014) proposed a flexible approach to modeling scattering using Finite Difference Method (FDM) with perturbation theory. This approach decomposes the medium parameters into background and perturbation parts, enabling the modeling of scattering from arbitrarily shaped scatterers and the interaction of the multiply scattered wavefield with the free surface. However, this approach assumes constant background medium parameters and employs the homogeneous wave equation for simulating the incident wavefield.

Considering the limitations of existing methodologies in modeling Near Surface Scatte-

ring (NSS) in complex overburden scenarios, a novel approach called the Partitioned Domain Method (PDM) is proposed as a promising solution. The PDM addresses these challenges by partitioning the computational domain and simulating the near-surface and deep wavefields separately. In this chapter, the PDM is introduced and its effectiveness is assessed through a numerical example utilizing the SEAM foothill model. The results substantiate the PDM's capability to generate deep wavefields devoid of significant NSS energy. This innovative approach provides valuable insights into wavefield characteristics and contributes to the advancement of seismic processing techniques for scattering noise attenuation.

3.3. Elastic wave modeling in heterogeneous media

In Section 2.3, the elastic wave equation for heterogeneous media was presented using operator notation, as follows:

$$L_{ij}(\rho, \lambda, \mu; t)u_j(\mathbf{x}, t) = 0, \tag{42}$$

where

$$L_{ij}(\rho, \lambda, \mu, t) = \delta_{ij}\rho(\mathbf{x})\partial_t^2 - \partial_i[\lambda(\mathbf{x})\partial_j] - \partial_j[\mu(\mathbf{x})\partial_i] - \delta_{ij}\partial_k[\mu(\mathbf{x})\partial_k]. \tag{43}$$

To analyze the scattering of elastic waves, it is assumed that the medium parameters deviate from the background homogeneous structure in the following manner Maeda et al. (2008); Sato et al. (2012):

$$\lambda(\mathbf{x}) = \lambda_0 + \delta\lambda(\mathbf{x}), \qquad \mu(\mathbf{x}) = \mu_0 + \delta\mu(\mathbf{x}), \qquad \rho(\mathbf{x}) = \rho_0 + \delta\rho(\mathbf{x}) \qquad \text{for } \mathbf{x} \in \mathcal{V}\ , \tag{44}$$

where subscript zero denotes a homogeneous background medium, and $\delta\rho$, $\delta\lambda$ and $\delta\mu$ denote the fluctuation of density and Lamé coefficients in the volume region $\mathcal{V}$.

In the subsequent sections, solutions for the elastic wave equation will be studied in both homogeneous and heterogeneous media.

3.3.1. Homogeneous background model. In the homogeneous background model, the elastic wave equation can be represented as:

$$L_{ij}(\rho_0, \lambda_0, \mu_0; t) u_j^0(\mathbf{x}, t) = 0. \tag{45}$$

Here, u^0 indicates the particle displacement that satisfies the homogeneous equation. Frequently, this equation is solved using Green's functions analysis, aiming to solve the equation for an impulsive source as follows:

$$L_{ij}(\rho_0, \lambda_0, \mu_0; \omega) G_{jk}(\mathbf{x}, t) = \delta_{ik}\delta(\mathbf{x} - \mathbf{x}'), \tag{46}$$

where G_{jk} is the Green's function for displacement of the j component induced by an excitation source in the k direction. $\delta()$ represents the Dirac delta function, and $\mathbf{x}'$ designates the source coordinate location.

As deduced by Sato et al. (2012), the Green's function can be expressed as combination of several Green's functions:

$$G_{jk}(\mathbf{x},t) = \underbrace{G^{P}_{jk}(\mathbf{x},t) + G^{Sv}_{jk}(\mathbf{x},t) + G^{Sh}_{jk}(\mathbf{x},t)}_{\text{Green's functions for body waves}} + G^{R}_{jk}(\mathbf{x},t) + G^{N}_{jk}(\mathbf{x},t). \tag{47}$$

Each term on the right-hand side of this equation represents a specific wave type. The first three terms $\left(G^{P}_{jk}, G^{Sv}_{jk}, G^{Sh}_{jk}\right)$ denote the Green's function for $P-$, Sv, and $Sh-$ body waves, respectively. The fourth term, G^{R}_{jk}, represents the Green's function for Rayleigh waves, while G^{N}_{jk} reflects the near-field effects.

By ignoring the near-field effects and combining all the body wave terms into a single term (G^{B}_{jk}), the total Green's function can be simplified as:

$$G_{jk}(\mathbf{x},t) = G^{B}_{jk}(\mathbf{x},t) + G^{R}_{jk}(\mathbf{x},t). \tag{48}$$

This resultant total Green's function can then be utilized to generate the total background wavefield as the sum of a body wavefield and a Rayleigh wavefield as follows:

$$\mathbf{u}^{0}(\mathbf{x},t) = \mathbf{u}^{0,B}(\mathbf{x},t) + \mathbf{u}^{0,R}(\mathbf{x},t). \tag{49}$$

3.3.2. Heterogeneous model. The solution to the wave equation for a heterogeneous model can be expressed in terms of the solution for a homogeneous medium. By incorporating Eq. (44) into Eq. (43), the operator L_{ij} can be split into two terms as follows:

$$[L_{ij}(\rho_0, \lambda_0, \mu_0; t) + L_{ij}(\delta\rho, \delta\lambda, \delta\mu; t)]u_j(\mathbf{x}, t) = 0. \tag{50}$$

Here, the first term on the left-hand side corresponds to the operator for the homogeneous equation, while the second term depends only on the perturbed medium parameters.

After relocating the second term to the right-hand side, the resulting equation is:

$$L_{ij}(\rho_0, \lambda_0, \mu_0; t)u_j(\mathbf{x}, t) = -L_{ij}(\delta\rho, \delta\lambda, \delta\mu; t)u_j(\mathbf{x}, t). \tag{51}$$

This equation shows that the term depending only on the perturbed medium parameters can be treated as a source term injected into the homogeneous elastic wave equation.

Consequently, the total wavefield can be expressed as the sum of an incident wavefield and a scattering wavefield as follows:

$$u_i(\mathbf{x}, t) = u_i^0(\mathbf{x}, t) + \int_{-\infty}^{\infty} dt' \iiint_{-\infty}^{\infty} d(\mathbf{x}')G_{ik}(\mathbf{x} - \mathbf{x}', t - t')[-L_{kj}(\delta\rho, \delta\lambda, \delta\mu; t)]u_j(\mathbf{x}', t'). \tag{52}$$

Alternatively, equation (52) can be expressed in the vector notation, such that $\mathbf{m} = (\lambda, \mu, \rho)$ and omitting the differential terms:

$$\mathbf{u} = \underbrace{\mathbf{u}^0}_{\text{incident wavefield}} + \underbrace{\int \mathbf{G}[-\mathbf{L}(\delta\mathbf{m})]\mathbf{u}}_{\text{scattering wavefield}}, \tag{53}$$

where

$$\mathbf{G} = \begin{bmatrix} G_{xx} & G_{xy} & G_{xz} \\ G_{yx} & G_{yy} & G_{yz} \\ G_{zx} & G_{zy} & G_{zz} \end{bmatrix}, \quad \mathbf{L} = \begin{bmatrix} L_{xx} & L_{xy} & L_{xz} \\ L_{yx} & L_{yy} & L_{yz} \\ L_{zx} & L_{zy} & L_{zz} \end{bmatrix}, \quad \text{and } \mathbf{u} = \begin{bmatrix} u_x \\ u_y \\ u_z \end{bmatrix}. \tag{54}$$

Notice that the scattering term in Eq. (53) depends on the total wavefield. By recursively replacing this equation within itself, an infinite series can be formed, which schematically looks like:

$$\mathbf{u} = \mathbf{u}^0 + \underbrace{\int \mathbf{G}[-\mathbf{L}(\delta\mathbf{m})]\mathbf{u}^0}_{\text{first-order scattering}} + \underbrace{\int \mathbf{G}[-\mathbf{L}(\delta\mathbf{m})] \int \mathbf{G}[-\mathbf{L}(\delta\mathbf{m})]\mathbf{u}^0}_{\text{second-order scattering}} + \underbrace{\ldots}_{\text{higher-order scattering}}. \tag{55}$$

This equation, known as the forward scattering series, demonstrates that scattering is a multiplicative process, which complicates its separation. Unlike additive noise, which can often be estimated and subtracted, multiplicative noise interacts nonlinearly with the seismic signal, making it more difficult to isolate.

The total wavefield can then be expressed as an infinite sum of scattering wavefield terms of different orders:

$$\mathbf{u} = \sum_{n=0}^{\infty} \mathbf{u}^n, \tag{56}$$

where each term $\mathbf{u}^n$ corresponds to the n-th-order scattering wavefield, which is defined as:

$$\mathbf{u}^n = \underbrace{\int \mathbf{G}[-\mathbf{L}(\delta\mathbf{m})] \cdots \int \mathbf{G}[-\mathbf{L}(\delta\mathbf{m})]}_{n \text{ nested integrals}} \mathbf{u}^0. \tag{57}$$

By incorporating Eq. (56) into Eq. (53), and after some manipulation, the total wavefield can be expressed as:

$$\mathbf{u} = \mathbf{u}^0 + \int \mathbf{G}[-\mathbf{L}(\delta\mathbf{m})] \left(\sum_{n=0}^{\infty} \mathbf{u}^n \right). \tag{58}$$

Finally, the total wavefield $\mathbf{u}$ can be expressed as the sum of a body wavefield $\mathbf{u}^B$ and a Rayleigh wavefield $\mathbf{u}^R$:

$$\mathbf{u} = \mathbf{u}^B + \mathbf{u}^R, \tag{59}$$

where

$$\mathbf{u}^B = \underbrace{\mathbf{u}^{0,B}}_{\text{incident body waves}} + \underbrace{\int \mathbf{G}^B[-\mathbf{L}(\delta\mathbf{m})] \left(\sum_{n=0}^{\infty} \mathbf{u}^n \right)}_{\text{body-waves scattering}}, \tag{60}$$

and

$$\mathbf{u}^R = \underbrace{\mathbf{u}^{0,R}}_{\text{incident Rayleigh waves}} + \underbrace{\int \mathbf{G}^R[-\mathbf{L}(\delta\mathbf{m})] \left(\sum_{n=0}^{\infty} \mathbf{u}^n \right)}_{\text{Rayleigh-wave scattering}}. \tag{61}$$

Note that Eq. (60) indicates that the body wavefield is expressed as the combination of incident body waves and body-wave scattering. This body-wave scattering corresponds to the multiple scattering where the last interaction results in a body wave, either P- or S-wave. Similarly, Eq. (61) shows that the Rayleigh wavefield is expressed as the combination of the incident Rayleigh wave and Rayleigh-wave scattering, which corresponds to the multiple scattering where the last interaction results in a Rayleigh wave.

3.3.3. First Born approximation. In the specific instance of heterogeneities exhibiting small fractional fluctuations (volume heterogeneities localized in the near-surface), the amplitude of the scattered wave is less than the incident wave. In this scenario, the scattering wavefield is approximated as single-scattering, as opposed to multiple scattering. This implies that only the first term of scattering is considered, and the total wavefield can be expressed as:

$$\mathbf{u} = \mathbf{u}^0 + \mathbf{u}^1 = \mathbf{u}^0 + \int \mathbf{G}[-\mathbf{L}(\delta\mathbf{m})]\mathbf{u}^0. \tag{62}$$

This approximation holds valid when $|\mathbf{u}^1| \ll |\mathbf{u}^0|$.

Consequently, the body wavefield and the Rayleigh wavefield are also represented as the sum of an incident wavefield and the single-scattering terms as follows:

$$\mathbf{u}^B = \mathbf{u}^{0,B} + \underbrace{\int \mathbf{G}^B[-\mathbf{L}(\delta\mathbf{m})]\mathbf{u}^{0,B}}_{\text{body-to-body waves}} + \underbrace{\int \mathbf{G}^B[-\mathbf{L}(\delta\mathbf{m})]\mathbf{u}^{0,R}}_{\text{Rayleigh-to-body waves}}, \tag{63}$$

$$\mathbf{u}^R = \mathbf{u}^{0,R} + \underbrace{\int \mathbf{G}^R[-\mathbf{L}(\delta\mathbf{m})]\mathbf{u}^{0,R}}_{\text{Rayleigh-to-Rayleigh waves}} + \underbrace{\int \mathbf{G}^R[-\mathbf{L}(\delta\mathbf{m})]\mathbf{u}^{0,B}}_{\text{body-to-Rayleigh waves}}. \tag{64}$$

Equations (63) and (64) reveal that the scattering wavefield comprises conversions between body and Rayleigh waves. The body-wave scattering consists of body-to-body and Rayleigh-to-body wave conversions. Conversely, Rayleigh-wave scattering includes Rayleigh-to-Rayleigh and body-to-Rayleigh wave conversions. Figure 23 provides a schematic representation of how seismic waves are scattered in the presence of a volume heterogeneity. There are four types of single-scattering: body-to-body, body-to-Rayleigh, Rayleigh-to-body, and Rayleigh-to-Rayleigh.

3.4. The perturbation method with FDM

In scenarios involving complex overburdens, the first Born approximation is not applicable due to the significant fractional fluctuations in medium parameters, leading to high amplitude scattering. Nonetheless, employing the perturbation method with FDM provides a straightforward and efficient approach to model multiple scattering without the need for the first Born approximation. This method, developed by Almuhaidib and Toksöz (2014), simulates the scattering wavefield using the following three-step process:

1) A total wavefield $\mathbf{u}$ is numerically computed using FDM with the elastic wave equation for heterogeneous media (42). This total wavefield comprises the incident $\mathbf{u}^0$ and scattering wavefield $\mathbf{u}^{sc}$ ($\mathbf{u} = \mathbf{u}^0 + \mathbf{u}^{sc}$).

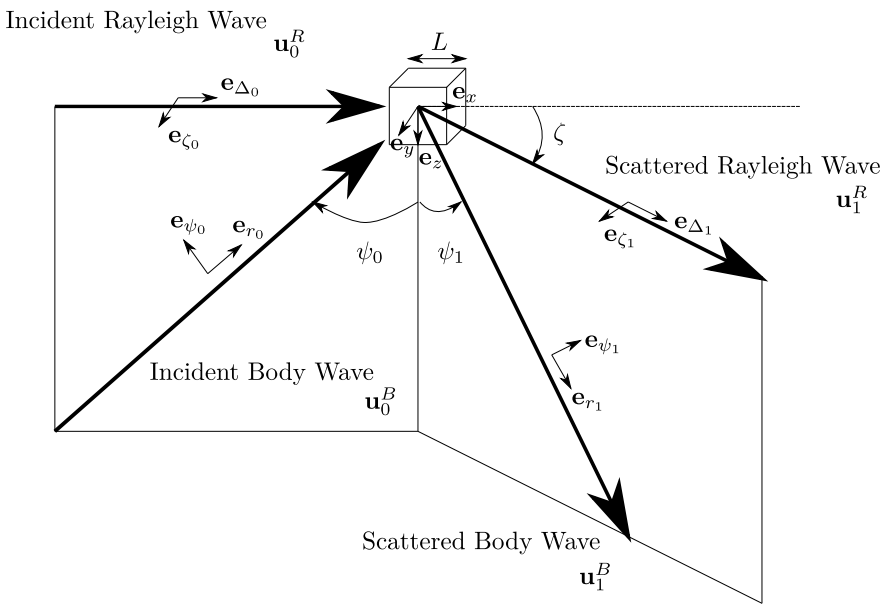

Figure 23. Scattering effects of near-surface localized elastic volume heterogeneities. Upon the incidence of body and Rayleigh waves on the heterogeneity, both wavefields are scattered, resulting in scattered body waves and scattered Rayleigh waves.

2) The incident wavefield $\mathbf{u}^0$ is numerically computed with FDM using the elastic wave equation for homogeneous media (45).

3) The scattering wavefield $\mathbf{u}^{\text{sc}}$ is then obtained by subtracting the incident wavefield from the total wavefield ($\mathbf{u}^{\text{sc}} = \mathbf{u} - \mathbf{u}^0$).

To illustrate the application of this method, consider the velocity and density model depicted in Figure 24, consisting of three homogeneous layers with two heterogeneities within the first layer. The elastic wave propagation is modeled numerically by employing a 30 Hz Ricker source positioned at a depth of 10 m and a horizontal distance of 1000 m. Receivers are positioned on the surface between 250 m and 1750 m horizontal distance, with an interval spacing of 2 m. The synthetic shot gathers of the incident, total, and scattered waves are

shown in Figure 25. Here, it is possible to observe the four types of single-scattering (body-to-body, body-to-Rayleigh, Rayleigh-to-body, and Rayleigh-to-Rayleigh)

Experiments conducted by Almuhaidib and Toksöz (2014) demonstrated the efficacy of this method in simulating near-surface scattering, not only under localized volume heterogeneities but also irregular bedrock interfaces. However, this method is predicated on a homogeneous background medium with constant parameters in the near-surface region. Consequently, it may not be able to handle more complex near-surface scenarios, such as those including rough topography and random media, as discussed in Chapter 1.

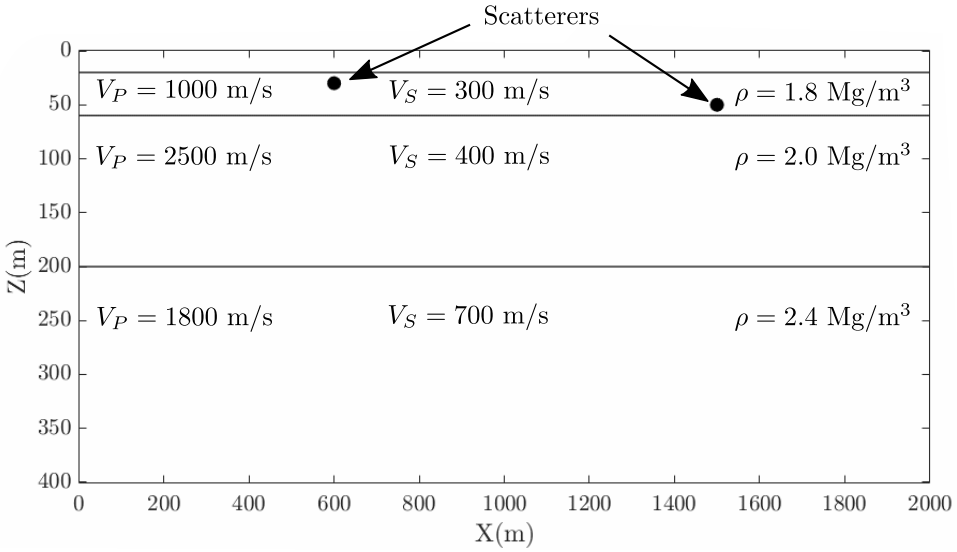

Figure 24. Earth model with three homogeneous layers and two scatter points in the first layer.

3.5. The partitioned domain method

Near-surface scattering (NSS) is influenced by not only localized heterogeneities and an irregular bedrock but also by surface topographic variations. In such cases, using the perturbation method with FDM may not be appropriate. Hence, the Partitioned Domain

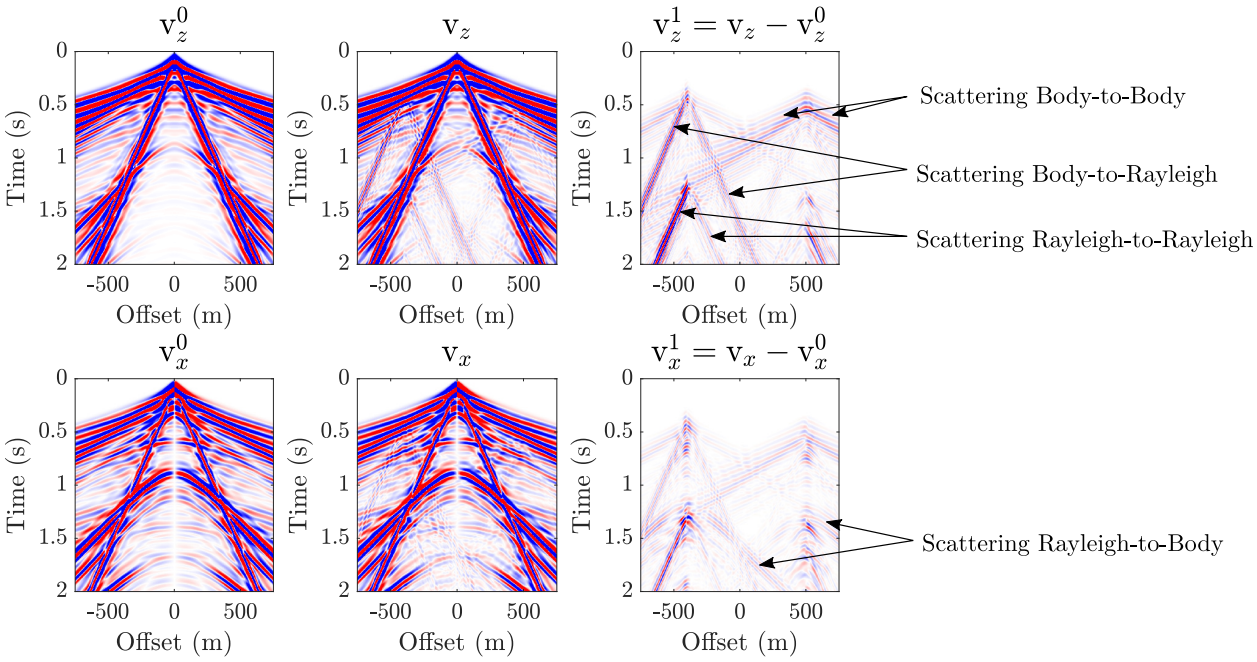

Figure 25. Scattering wavefield computation using the perturbed method (the difference between total and incident wavefields).

Method (PDM) is introduced as an approach capable of addressing complex land areas characterized by rough topography and near-surface parameter variations.

Consider a spatial computational domain, Ω, representing the earth model parameters. This domain can be divided into two subdomains, Ω_1 and Ω_1, as illustrated in Figure 26. The subdomain Ω_1, with a depth of Z_{ns}, refers to the near-surface region, while Ω_2, the portion below Ω_1, denotes deeper structures.

In the field of exploration seismology, the source is often situated in the near-surface region. This source generates seismic waves, incident body-waves $\mathbf{u}_{\Omega_1}^{0,B}$ and incident Rayleigh waves $\mathbf{u}^{0,R}$, which propagate through the near-surface (Ω_1) (Figure 27(a)). Owing to the presence of heterogeneities with fractional fluctuations of medium parameters ($\delta\mathbf{m}$) in the

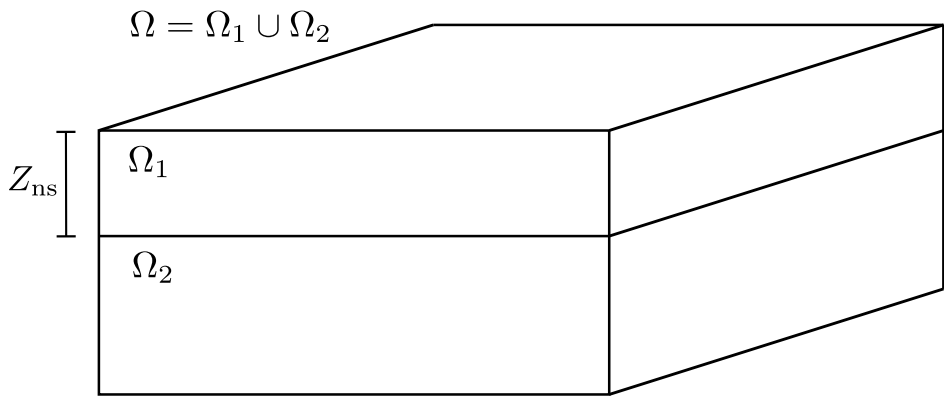

Figure 26. Partition of the whole domain Ω for the earth model parameters into the sub-domains Ω_1 (near-sruface portion) and Ω_2 (deep structures portion). The depth of Ω_1 is represented by Z_{ns}

near-surface region, these incident waves scatter, producing body-wave scattering $\mathbf{u}^{n,B}_{\Omega_1}$ and Rayleigh wave scattering $\mathbf{u}^{n,R}$ (Figure 27(b)).

A portion of the body-wave energy, whether incident or scattering, is transmitted to the deeper structures (Ω_2). Due to the contrast layers, this transmitted energy is reflected back to the near-surface as $\mathbf{u}^{0,B}_{\Omega_2}$ (Figure 27(c)). Upon hitting the near-surface heterogeneities, this reflected energy generates a new scattered wavefield, $\mathbf{u}^{n,B}_{\Omega_2}$ (Figure 27(d)).

Consequently, the total wavefield can be expressed as a superposition of an incident wavefield and NSS as follows:

$$\mathbf{u}_{\text{TW}} = \mathbf{u}^{0,B}_{\Omega_1} + \mathbf{u}^{0,B}_{\Omega_2} + \mathbf{u}^{0,R} + \underbrace{\int \mathbf{G}[-\mathbf{L}(\delta\mathbf{m})] \left(\sum_{n=0}^{\infty} \left(\mathbf{u}^{n,B}_{\Omega_1} + \mathbf{u}^{n,B}_{\Omega_2} + \mathbf{u}^{n,R} \right) \right)}_{\text{NSS: near-surface scattering}}. \tag{65}$$

The NSS can be further decomposed into NSS produced by Ω_1 waves and NSS gene-

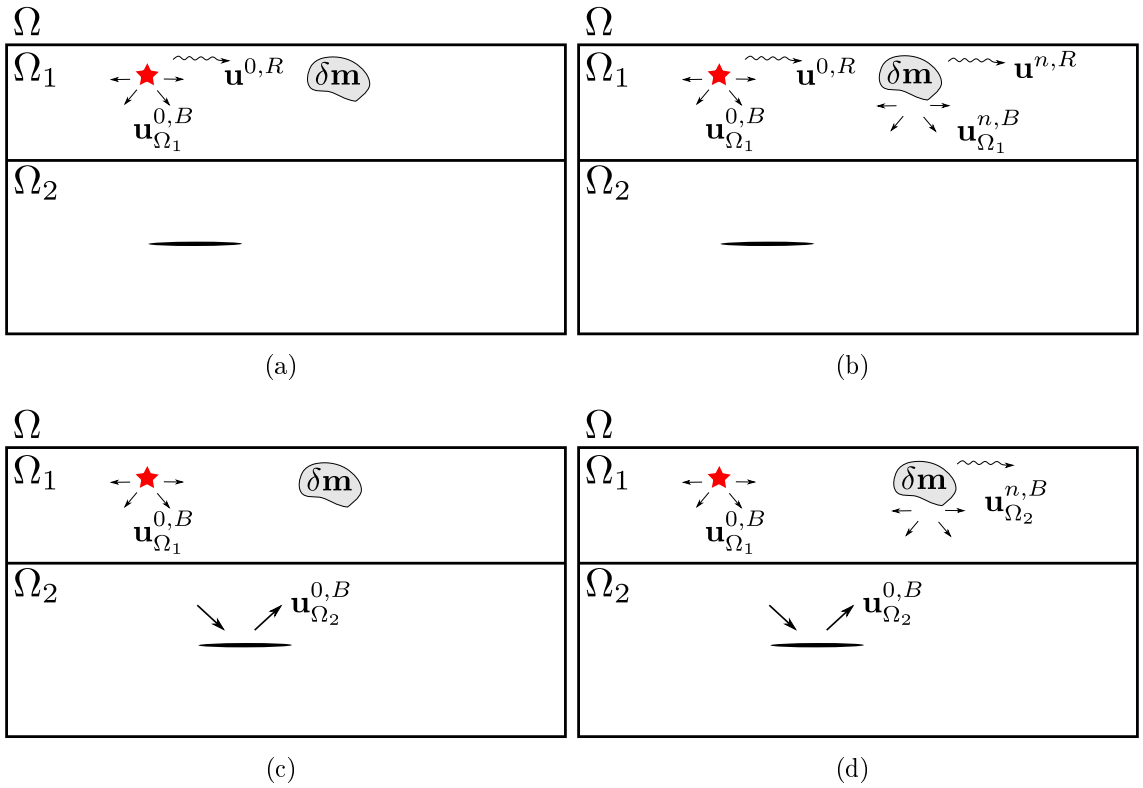

Figure 27. Near-surface scattering produced by a heterogeneity with parameters fluctuation represented by $\delta\mathbf{m}$. (a) Incident wavefields located in the near-surface segment. (b) Near-Surface Scattering (NSS) of Ω_1 waves. (c) Incident upgoing waves stemming from Ω_2, including reflections and refractions. (d) NSS of upgoing waves originating from Ω_2. The red star denotes the source location. Straight arrows signify the propagation of body waves, while wiggly arrows indicate Rayleigh wave propagation.

rated by Ω_2 waves as:

$$\mathbf{u}_{\mathrm{TW}} = \mathbf{u}^{0,B}_{\Omega_1} + \mathbf{u}^{0,B}_{\Omega_2} + \mathbf{u}^{0,R} + \underbrace{\int \mathbf{G}[-\mathbf{L}(\delta\mathbf{m})] \left(\sum_{n=0}^{\infty} \left(\mathbf{u}^{n,B}_{\Omega_1} + \mathbf{u}^{n,R} \right) \right)}_{\text{NSS from } \Omega_1 \text{ waves}} + \underbrace{\int \mathbf{G}[-\mathbf{L}(\delta\mathbf{m})] \left(\sum_{n=0}^{\infty} \left(\mathbf{u}^{n,B}_{\Omega_2} \right) \right)}_{\text{NSS from } \Omega_2 \text{ waves}}. \tag{66}$$

During seismic processing in exploration, the filtering stage aims to cleanse the total wavefield and isolate the reflected wavefield, $\mathbf{u}^{0,B}_{\Omega_2}$, which is then used to image the deeper structures.

3.5.1. Near-surface wavefield. The near-surface wavefield, $\mathbf{u}_{\mathrm{NW}}$, represents the solution of the elastic wave equation when only Ω_1 is considered as the computational domain. Consequently, the near-surface wavefield can be derived by excluding Ω_2 waves from equation (66), as depicted below:

$$\mathbf{u}_{\mathrm{NW}} = \mathbf{u}^{0,B}_{\Omega_1} + \mathbf{u}^{0,R} + \underbrace{\int \mathbf{G}[-\mathbf{L}(\delta\mathbf{m})] \left(\sum_{n=0}^{\infty} \left(\mathbf{u}^{n,B}_{\Omega_1} + \mathbf{u}^{n,R} \right) \right)}_{\text{NSS from } \Omega_1 \text{ waves}}. \tag{67}$$

In this equation, only the near-surface scattering (NSS) arising from Ω_1 waves are taken into account.

3.5.2. Deep wavefield. The primary objective of PDM method is to obtain a synthetic wavefield that is devoid of NSS. Hence, the deep wavefield is defined as the difference between the total wavefield and the near-surface wavefield, as shown below:

$$\mathbf{u}_{\mathrm{DW}} = \mathbf{u}_{\mathrm{TW}} - \mathbf{u}_{\mathrm{NW}}. \tag{68}$$

By integrating equations (66) and (67) into (68), the deep wavefield can be expressed as follows:

$$\mathbf{u}_{\mathrm{DW}} = \mathbf{u}_{\Omega_2}^{0,B} + \underbrace{\int \mathbf{G}[-\mathbf{L}(\delta\mathbf{m})] \left(\sum_{n=0}^{\infty} \mathbf{u}_{\Omega_2}^{n,B} \right)}_{\text{NSS from } \Omega_2 \text{ waves}}. \tag{69}$$

Please note that while the deep wavefield recovers the energy of the reflected waves, $\mathbf{u}_{\Omega_2}^{0,B}$, it still contains residual energy from the NSS of Ω_2 waves. This implies that the PDM method can be utilized to separate, via simulation, the total wavefield from the NSS of Ω_1 waves. It's important to recognize that the residual NSS from Ω_2 waves is considerably less energetic than the NSS from Ω_1 waves.

3.5.3. Implementation of PDM method. The PDM method can be implemented by following these four steps:

1) Partition the entire domain Ω into two subdomains, Ω_1 and Ω_2, as depicted in Figure (26). The depth of Ω_1, denoted by Z_{ns}, must be manually determined based on the chosen limit for the near-surface portion.

2) Compute the total wavefield $\mathbf{u}$ by numerically solving the elastic wave equation for heterogeneous media (42). This total wavefield comprises both the near-surface wavefield $\mathbf{u}_{\mathrm{NW}}$ and the deep wavefield $\mathbf{u}_{\mathrm{DW}}$ (thus, $\mathbf{u} = \mathbf{u}_{\mathrm{NW}} + \mathbf{u}_{\mathrm{DW}}$).

3) Calculate the near-surface wavefield $\mathbf{u}_{\mathrm{NW}}$ by numerically solving the elastic wave equation for heterogeneous media (42), this time only considering the subdomain Ω_1. Before solving, crop the earth model at the depth Z_{ns}.

4) Determine the deep wavefield $\mathbf{u}_{\mathrm{DW}}$ by subtracting the near-surface wavefield from the total wavefield (i.e., $\mathbf{u}_{\mathrm{DW}} = \mathbf{u} - \mathbf{u}_{\mathrm{NW}}$).

In the following section, an example of the application of the PDM method will be presented, underscoring the advantages of employing this approach.

3.6. Numerical example with the SEAM Foothills Phase II model

To illustrate the effectiveness of the PDM method in modeling NSS, an experiment using the SEAM Foothills Phase II model was conducted. In particular, a portion of the model that was previously explored in section 2.7.2 was used for this example. For the acquisition setup, receivers were arranged on the surface along a line stretching from 500 to 5500 m along the x-axis, with an inter-receiver distance of 10 m, and an explosive source was placed at X = 1000 m. The topographic elevation map for this model, along with the acquisition geometry, is depicted in Figure 21.

In this example, the steps detailed in subsection 3.5.3 were followed, considering three different near-surface depth values, Z_{ns}. Specifically, Z_{ns} was set to 1100 m, 1300 m, and 1500 m. Figure 28 illustrates the boundaries of the near-surface for these three different depths within the 2D section of the model, in the same plane as the line of receivers.

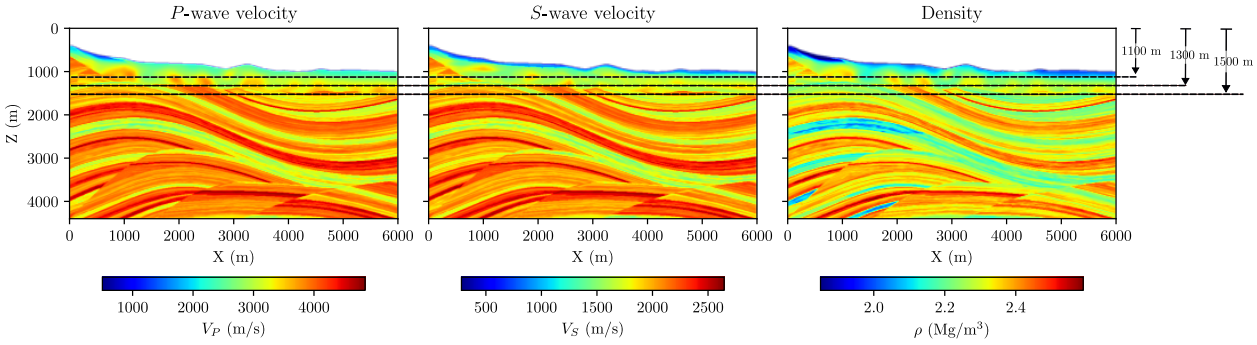

Figure 28. 2D section of the SEAM portion model sliced along the line of receivers. The topographic elevation map and the acquisition geometry are depicted in Figure 21.

The PMFD3D-GPU solver, presented in chapter 2, was utilized to solve the elastic wave equation for both the whole domain Ω and the subdomain Ω_1. Snapshots of the propagation for the total, near-surface, and deep wavefields are illustrated in Figure 29. These snapshots correspond to Z_{ns} =1500 (m). It is important to observe that in the near-surface wavefield, seismic energy does not appear for depths below 1500 (m). Additionally, in the deep wavefield, there is noticeable energy above the near-surface limit. This corresponds to the upgoing waves from Ω_2 that are not being simulated in the near-surface wavefield.

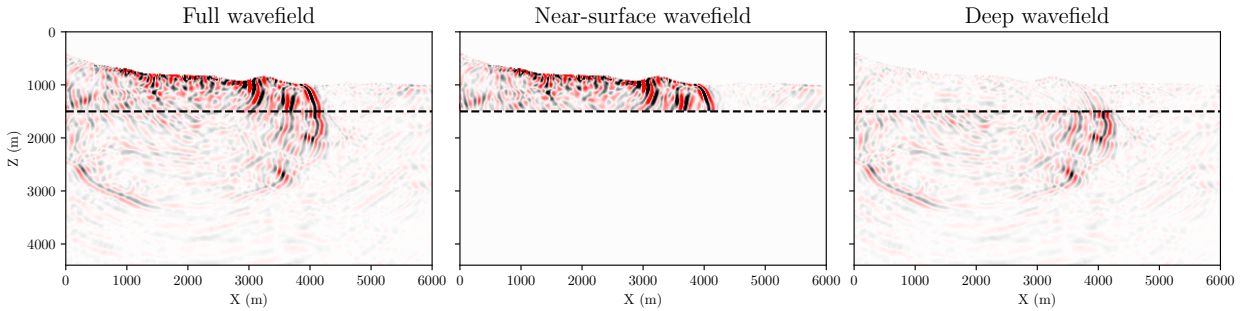

Figure 29. Snapshots of the vertical particle velocity at $t = 2$ (s). (a) total wavefield, (b) near-surface wavefield, and (c) Deep wavefield (the difference between (a) and (b)). In the near-surface wavefield, the earth model depth extends to the dashed line, which includes ABC at the bottom.

The multicomponent shot gather for the total wavefield exhibits various wave types such as Rayleigh waves, refractions, reflections, and NSS (as illustrated in Figure 30). Similarly, the multicomponent shot gathers for the near-surface wavefields also exhibit various wave types. However, these wavefields do not contain waves from the Ω_2 subdomain, as indicated in equation 67. It is observed that the deeper the near-surface portion, the more pronounced the energy of refraction events becomes. In the multicomponent shot gathers of

the deep wavefield, which were obtained by subtraction, it is evident that more refraction energy is present when the near-surface portion is more shallow.

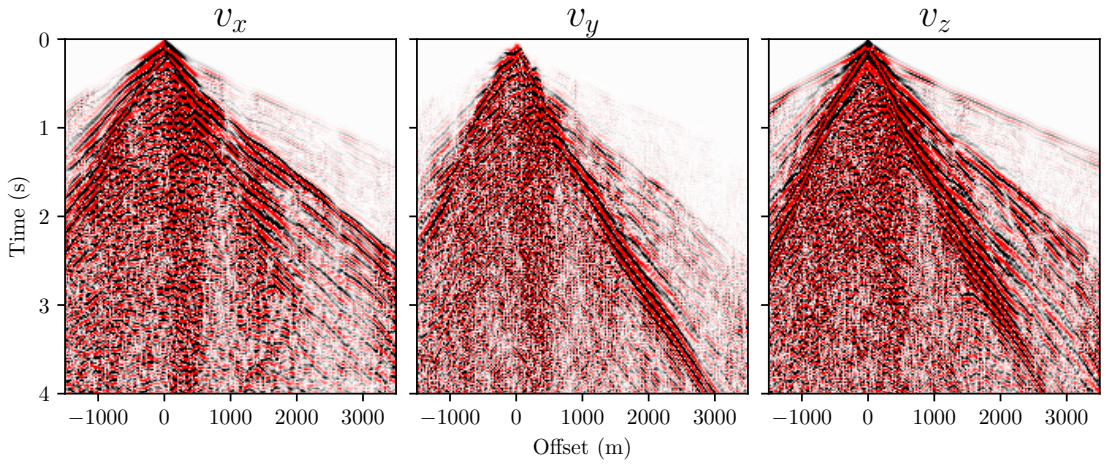

Figure 30. Multicomponet shot gather for the total wavefield acquired in the portion of the SEAM Foothills model using whole domain.

An analysis was conducted to quantify the energy proportion of the near-surface wavefield and the deep wavefield in relation to the total wavefield. The results, presented in Table 6, demonstrate that the total wavefield is predominantly composed of the near-surface wavefield, with only a minor portion of the energy attributed to the deep wavefield. Specifically, in the x- and z-components, the near-surface wavefield accounted for over 99.7 % of the total energy across all three different depths of the near-surface portion. Consequently, the deep wavefields represented 0.3 % or less of the total energy.

3.7. Discussion

The proposed PDM has demonstrated its efficacy as a strategy for modeling NSS in complex overburden scenarios, which include rough topography and random media. This

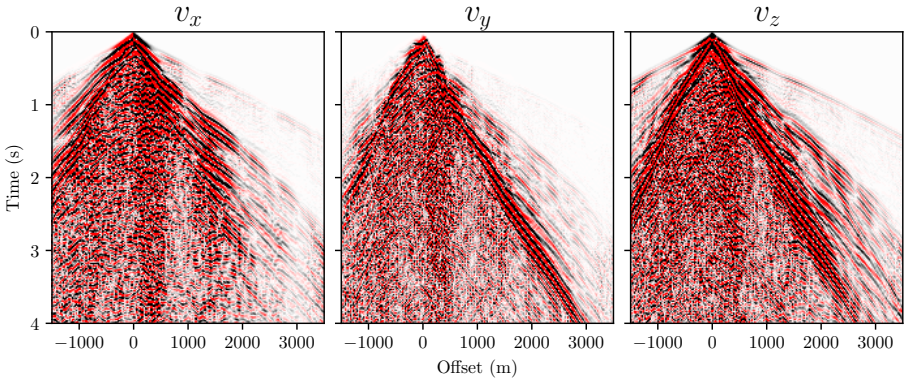

(a)

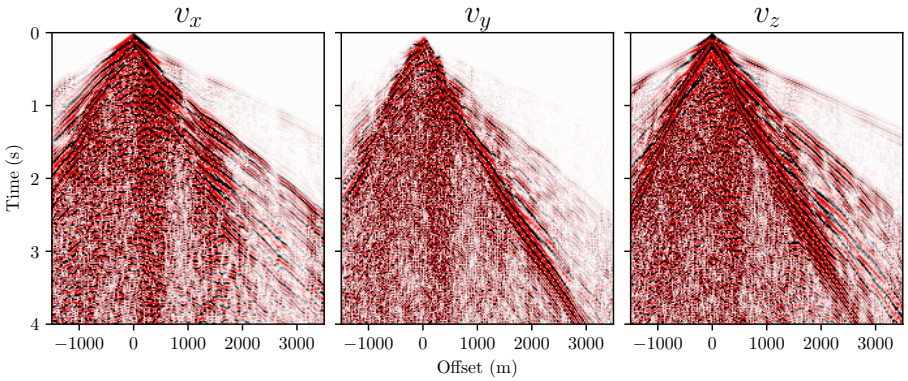

(b)

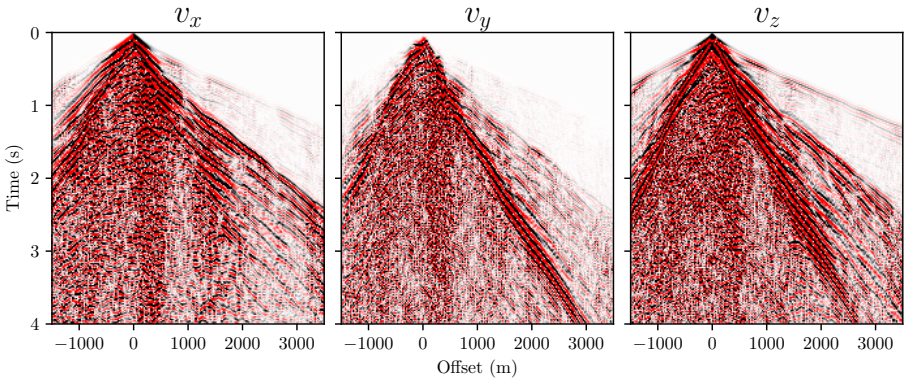

(c)

Figure 31. Multicomponent shot gather of the near-surface wavefield with different depths of near-surface subdomain. (a) Z_{ns} =1100 (m). (b) Z_{ns} =1300 (m). (c) Z_{ns} =1500 (m).

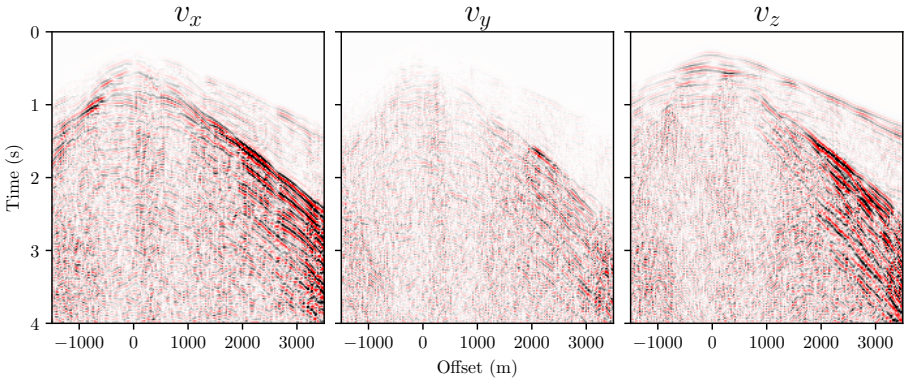

(a)

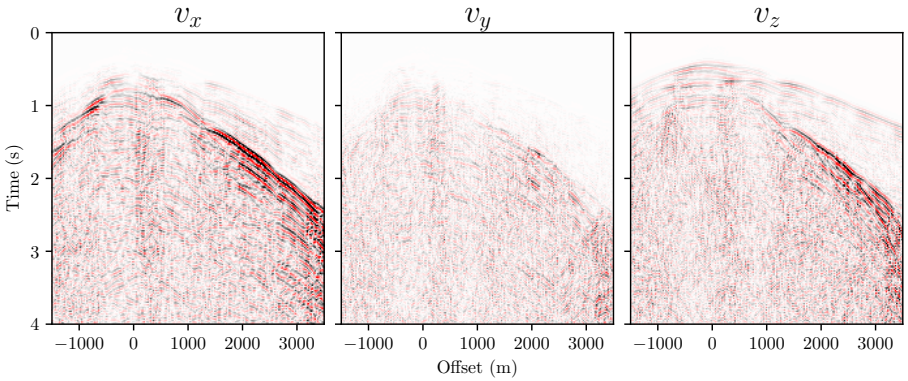

(b)

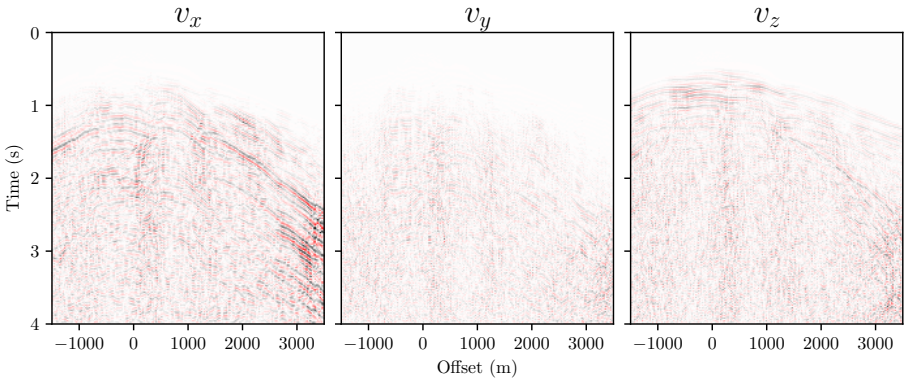

(c)

Figure 32. Multicomponent shot gather of the deep wavefield with different depths of near-surface subdomain. (a) Z_{ns} =1100 (m). (b) Z_{ns} =1300 (m). (c) Z_{ns} =1500 (m).

Table 6
Percentage of composition of near-surface wavefield and deep wavefield in relation to the total wavefield

Ω_1 depth (m)	Near-surface wavefield			Deep wavefield		
	v_x (%)	v_y (%)	v_z (%)	v_x (%)	v_y (%)	v_z (%)
1100	99.72	97.17	99.74	0.28	2.83	0.26
1300	99.79	97.93	99.80	0.21	2.07	0.20
1500	99.97	99.61	99.97	0.03	0.39	0.03

is a distinct advantage over existing methods, such as the analytical perturbation method, asymptotic methods, integral equation, and FDM with perturbation method. These conventional methods typically assume constant background medium parameters and rely on the homogeneous wave equation to simulate the incident wavefield. Contrary to these methods, PDM does not make this assumption, thereby enabling the generation of incident waves in heterogeneous background models. This capability leads to a more accurate modeling of NSS in complex environments.

The mathematical model revealed that partitioning the computational domain makes it possible to separate the total wavefield into two components: the near-surface wavefield and the deep wavefield. Numerical results obtained with the SEAM foothills model confirmed that a significant majority of seismic energy (around 99 %) was localized in the near-surface wavefield, while only a minor fraction (about 1 %) was detected in the deep wavefield (see Table 6). Despite their lower energy, deep wavefields carry all the energy of the upcoming waves, which are essential for imaging deeper geological structures.

The principal contribution of the PDM is its ability to generate ideal synthetic data de-

void of ground roll. The numerical example clearly showed that the resulting deep wavefields are free from wave types often classified as coherent noise, including Rayleigh waves, near-surface refractions (diving waves), reflections, and most near-surface scattering (see Figure 32). The simulated deep wavefield can thus serve as a synthetic gold standard, facilitating the validation and comparison of new filtering techniques. Although real data is generally preferable for training machine learning models due its authenticity and variability, the generation of numerous synthetic gold standards offer the advantage of being significantly more cost-effective and time-efficient compared to collecting real seismic data. All these aspects underscore the utility of the PDM for the advancement of seismic processing techniques.

While the PDM clearly offers numerous benefits, it's crucial to also consider its limitations. One significant limitation stems from the formulation of the method itself. The PDM is designed to separate NSS by treating it as an additive process rather than a multiplicative one. This approach results in an incomplete isolation of NSS from the total wavefield, as demonstrated by equation (68), which indicates that the deep wavefield still retains some NSS produced by the upcoming waves. However, the residual NSS is considerably less energetic than that found in the near-surface wavefield (Figures 31 and 32), allowing the PDM to remain a viable tool for simulating synthetic data free from ground roll. Another limitation involves setting the domain partition through the adjustment of the Z_{ns} value. This value must be manually calibrated based on the near-surface depth. The numerical example showed that larger Z_{ns} values yield a near-surface wavefield with higher energy, and correspondingly, a deep wavefield with lower energy (see Table 6). Thus, users must experiment

with various Z_{ns} values to obtain the desired wavefield results from the PDM.

3.8. Conclusions

In this chapter, the Partitioned Domain Method (PDM) has been introduced as an innovative approach for modeling Near-Surface Scattering (NSS) in complex overburden scenarios, characterized by rough topography and random media. By employing a domain partitioning technique, the PDM separates the total wavefield into distinct near-surface and deep wavefields, enabling more accurate simulations. Notably, the PDM stands out from existing methodologies by eliminating the assumption of constant background medium parameters and facilitating the generation of incident waves in heterogeneous background models. Although the PDM exhibits limitations, such as the incomplete isolation of NSS and the requirement for manual calibration of the domain partition, the resulting synthetic wavefields offer valuable synthetic data devoid of ground roll. These synthetic datasets serve as a gold standard for the validation and comparison of novel filtering techniques. Furthermore, the generation of synthetic data holds significant potential for advancing seismic processing techniques and training machine learning models aimed at attenuating scattering noise. Future research efforts should focus on addressing the limitations of the PDM and expanding its applicability in the field of near-surface scattering modeling.

CHAPTER 4. Polarization analysis and filtering in the frequency-slowness domain of undersampled 3C seismic data

4.1. Abstract

Polarization filters have emerged as a useful tool for coherent noise attenuation in multicomponent seismic data. By exploiting the polarization properties of seismic waves, these filters can significantly improve wave type separation, which is a crucial step in seismic data processing. The existing methods fall into two categories: single-station and multi-station filters, each with unique advantages and limitations. Single-station filters, while free of constraints related to spatial sampling, cannot utilize velocity information for wave type discrimination. Conversely, multi-station approaches leverage coherence between traces for wave separation but require regularly spatially sampled data. To address these limitations, a novel two-step method is introduced for distinguishing and separating polarized wave types in shot gathers captured from an spatial undersampled linear array of 3C vector sensors. The first step involves conducting a polarization analysis in the frequency-slowness domain using elliptical elements derived from the linear Radon transform of the seismic data. The second step isolates specific polarized waves using the 3C Frequency-Slowness Polarization Filter (3C-FSPF), a technique that employs tailored activation functions based on the polarization analysis. To evaluate the proposed method, comprehensive tests were conducted on both synthetic and real data. The results consistently demonstrate the effectiveness of 3C-FSPF in separating diverse polarized wave types under conditions of irregular and sparse spatial sampling

and noise. The findings underscore the potential of this method for advancing exploration geophysics by enhancing the quality of seismic data, particularly in land regions with complex near-surface structures. Future work will explore the application of this method in other geophysical contexts and the use of machine learning algorithms to refine the technique.

4.2. Introduction

Filtering of coherent noise such as surface waves is a critical stage of the seismic data processing workflow. These waves, while potentially informative about surface structures, can interfere with the detection of signals reflecting from deeper geological layers. Thus, efficient and accurate methods for their separation are key to the success of seismic surveys, particularly when exploring for hydrocarbons. The separation of wave types is typically performed in the frequency-wavenumber (f, k) or frequency-slowness (f, p) domains, which are known to segregate different wave types into distinct regions. This enables the design of filters that specifically target and eliminate unwanted waves, such as surface waves, while retaining desired waves like primary reflections. However, despite the effectiveness of these techniques, they encounter significant obstacles when applied to areas with complex land seismic characteristics. Two main factors contribute to these challenges. Firstly, spatial sampling can be greatly limited due to issues like difficult accessibility and the existence of complex geographical features such as mountains and foothills. Secondly, a substantial proportion of seismic energy is scattered within the near-surface region, due to low-velocity layers and geological heterogeneities. As reported by Stork (2020) and Sánchez-Galvis et al. (2021), these heterogeneities can cause scattering noise, irregular guided waves, and wave-

let distortion, which collectively complicate the task of wave type differentiation within the (f, k) and (f, p) domains. To address these challenges, alternative methods such as polarization filters have been explored to separate wave types. Nevertheless, these methods bring their own set of challenges depending on the selected approach.

Seismic polarization methods can be broadly categorized into single-station and multi-station approaches. The single-station approach estimates the polarization content of seismic waves from multicomponent sensors individually, making it independent of spatial sampling. The Covariance Matrix Method (CMM), introduced by Filnn (1965), was the first single-station polarization technique for seismic data. This method utilizes time windows of the 3C trace to analyze the rectilinearity and direction of particle motion, which are estimated from the eigenvalues of the covariance matrix. CMM has been employed to design polarization filters for enhancing the signal-to-noise ratio of teleseismic body phases (Montalbetti and Kanasewich, 1970), separating P- and S-wave components from three-component (3C) crosswell seismic data (Liu et al., 2012), and removing ground roll (Perelberg and Hornbostel, 1994).

However, the accuracy of polarization analysis using the original formulation of the CMM is dependent on the length of the time window. Consequently, some modifications have been suggested. For instance, Jurkevics (1988) computed the polarization parameters using sliding time windows into frequency bands of the multicomponent trace. Additionally, Christoffersson et al. (1988) employed maximum likelihood estimation for the particle motion using models of P, S, Love, and Rayleigh waves.

The complex trace method (CTM) was introduced to reduce the limitations of time windows by instantaneously computing the polarization attributes via the analytic signal. Vidale (1986) initiated this by computing the instantaneous covariance matrix of the analytic signal vector, followed by Rene et al. (1986) who computed instantaneous polarization attributes using the CTM for 2C trace. Later, Morozov and Smithson (1996) developed a generalized polarization analysis for time-domain instantaneous attributes from 3C analytic signal. Lu et al. (2010) used CTM to estimate the instantaneous ellipticity and implemented the instantaneous polarization filtering method to obtain instantaneous linear or elliptic polarization in the case of land multi-component records acquired in energy exploration.

The spectral matrix method (SMM), introduced by Samson (1977), was another noteworthy advancement addressing the limitations of time windows. This method performs the analysis in the frequency domain rather than the time domain. It was developed into a method for the design of polarization detectors and filters in the frequency domain. Later, Samson and Olson (1981) developed data-adaptive polarization filters based on the polarization analysis using SMM. Then, Du et al. (2000) developed a data-adaptive polarization filter to reduce micro-seismic noise contamination in three-component broad-band seismograms.

Other develpments include the Singular Value Decomposition Method (SVDM), introduced by Jackson et al. (1991). This was a novel method for estimating polarization attributes by singular value decomposition of the 3C seismic trace. SVDM was used to design several polarization filters for wave type separation (De Franco, 2001), and ground roll attenuation (Jin and Ronen, 2005; Tiapkina et al., 2012; Sánchez-Galvis et al., 2016).

Further advancements came with the introduction of the time-frequency domain methods (TFDM). Pinnegar (2006) proposed a new form of polarization analysis and filtering by representing the 3C signal into elliptical elements in the time-frequency domain using the S-transform. Other significant contributions using the S transform have been developed (Tan et al., 2013; Kazemnia Kakhki et al., 2020). Alternatively, TFDM was also studied by incorporating the wavelet transform (Roueff et al., 2006; Diallo et al., 2005, 2006b,a; Kulesh et al., 2007; Wang and Wang, 2017).

Most recently, the Correlation Matrix Method (CrMM), proposed by Nasr et al. (2021), is a time-domain method conceived to enhance the accuracy of polarization analysis with outlier data.

In contrast to the single-station approach, multi-station methods use multiple sensors simultaneously by utilizing coherence between traces for wave type separation. Le Bihan and Mars (2004) introduced a subspace method for wave separation on 3C data using an extension of the Singular Value Decomposition (SVD) algorithm to the field of quaternions, a technique further developed by Hobiger et al. (2011, 2012); Le Bihan et al. (2014). Other methods, such as the wideband spectral matrix method introduced by Paulus et al. (2005); Paulus and Mars (2006), and the extended SVD method for multiple traces proposed by Kendall et al. (2005a,b); de Meersman and Kendall (2005); De Meersman (2008); Al-Hasanat et al. (2017) have expanded the field of seismic data analysis. Finally, the Quaternion SVD approach, a fusion of quaternion and SVD methodologies, was investigated by Sajeva and Menanno (2017) for the characterization and extraction of a Rayleigh-wave mode in vertically

heterogeneous media. However, multi-station methods are constrained by the requirement for regularly spaced data, a condition that is often challenging to meet in seismic exploration of complex land areas where geological conditions prohibit regular spatial sampling.

In response to these limitations, a novel two-step method is proposed for effectively distinguishing and separating polarized wave types in shot gathers captured from an under-sampled linear array of 3C vector sensors. This method enhances the technique presented by Pinnegar (2006) by transforming the seismic data into the frequency-slowness (f, p) domain for simultaneous operation on multiple traces. This represents a shift from Pinnegar's original model, which operates on a single-station basis in the time-frequency (t, f) domain. Moreover, the proposed method incorporates activation functions with adjustable parameters, which allows the filtering process to adapt to different wave types. This represents a substantial modification from the fixed-parameter functions proposed by Pinnegar (2006), which primarily focused on the attenuation of the Rayleigh wave.

4.3. Frequency-Slowness domain analysis

The frequency-slowness (f, p) domain analysis is an essential tool in seismic processing, particularly in the areas of ground roll attenuation (Trad et al., 2003; Luo et al., 2009a; Hu et al., 2016), and velocity estimation (Luo et al., 2007, 2008). The transformation of the seismic data from the time-offset domain (t, h) to the frequency-slowness (f, p) domain can be performed by the LRT in the frequency domain.

The forward LRT in the frequency domain is given by (Yilmaz 2001):

$$m(p,f) = \sum_{h=h_{\min}}^{h_{\max}} d(h,f) e^{i2\pi fph}. \tag{70}$$

Similarly, the conjugate transform from the frequency-slowness (f,p) domain to the time-offset domain (t,h) is given by:

$$d(h,f) = \sum_{p=p_{\min}}^{p_{\max}} m(p,f) e^{-i2\pi fph}, \tag{71}$$

where $d(h,f)$ is the shot gather after the temporal Fourier transform, the function $m(p,f)$ is the Radon model, f is the frequency, p is the slowness ($p_{\min}$ and $p_{\max}$ are the slowness range), and h is the offset ($h_{\min}$ and $h_{\max}$ are the offset range).

For one particular frequency f, the LRT can be written in a matrix form as follows:

$$\mathbf{d} = \mathbf{L}\mathbf{m}, \tag{72}$$

where $\mathbf{d} \in \mathbb{C}^{N_h \times 1}$ represents the Fourier coefficients of the shot gather with N_h traces, $\mathbf{m} \in \mathbb{C}^{N_p \times 1}$ denotes the Radon model with N_p slowness values, and $\mathbf{L} \in \mathbb{C}^{N_h \times N_p}$ is the forward LRT operator with the form:

$$\mathbf{L} = \begin{bmatrix} e^{-i2\pi f p_0 h_0} & e^{-i2\pi f p_1 h_0} & \dots & e^{-i2\pi f p_{N_p-1} h_0} \\ e^{-i2\pi f p_0 h_1} & e^{-i2\pi f p_1 h_1} & \dots & e^{-i2\pi f p_{N_p-1} h_1} \\ \vdots & \vdots & \ddots & \vdots \\ e^{-i2\pi f p_0 h_{N_h-1}} & e^{-i2\pi f p_1 h_{N_h-1}} & \dots & e^{-i2\pi f p_{N_p-1} h_{N_h-1}} \end{bmatrix}. \tag{73}$$

The adjoint transformation can be also written in a matrix form as follows:

$$\mathbf{m}_{\text{adj}} = \mathbf{L}^{\text{H}}\mathbf{d}, \tag{74}$$

where $\mathbf{L}^{\text{H}}$ is the conjugate transpose of $\mathbf{L}$, and $\mathbf{m}_{\text{adj}}$ is the adjoint Radon model. This adjoint model has low resolution and it cannot be used to reconstruct the original data in the (f, h) domain. However, the High Resolution LRT (HRLRT) can be used to find the Radon model that best fits the data by using an inversion scheme with sparsity constraint (Trad et al. 2003; Luo et al. 2009b). Specifically, The HRLRT can be computed by minimizing the following objective function:

$$J = \|\mathbf{W}_r \left(\mathbf{d} - \mathbf{L}\mathbf{W}_m^{-1}\mathbf{W}_m\mathbf{m}\right)\|^2 + \alpha\|\mathbf{W}_m\mathbf{m}\|^2, \tag{75}$$

where $\mathbf{W}_r \in \mathbb{R}^{N_h \times N_h}$ is a matrix of diagonal weights of residual values, $\mathbf{W}_m \in \mathbb{R}^{N_p \times N_p}$ is a diagonal matrix of model space weights and $\alpha \in \mathbb{R}$ is a regularization parameter that maintains balance between data misfit and model constraints. The vector model $\mathbf{m}$ that

minimizes the objective function J can be found by solving the following equation:

$$\left(\mathbf{W}_m^{-T}\mathbf{L}^H\mathbf{W}_r^T\mathbf{W}_r\mathbf{L}\mathbf{W}_m^{-1} + \lambda\mathbf{I}\right)\mathbf{W}_m\mathbf{m} = \mathbf{W}_m^{-T}\mathbf{L}^H\mathbf{W}_r^T\mathbf{W}_r\mathbf{d}, \tag{76}$$

where $\mathbf{I} \in \mathbb{R}^{N_h \times N_h}$ is the identity matrix. Equation (76) can be solved by using a conjugate gradient (CG) algorithm. Details about implementation of CG method are presented in Appendix A.

4.4. Polarization analysis of 3C seismic data

Polarization information from seismic waves can be captured using three-component (3C) vector sensors. At a particular frequency, represented as f, the signal from the 3C sensor traces an ellipse within three-dimensional space. The shape and orientation of this ellipse can be expressed using six elements of Fourier coefficients. These elements may comprise either the three amplitudes and their corresponding phases, or the three real and three imaginary components.

Alternatively, the shape and orientation of the ellipse can be described by another set of six elements commonly employed in the characterization of planetary orbits (Murray and Dermott, 1999). These elements include the semi-major axis a, the semi-minor axis b, the inclination angle I, the longitude of the ascending node Ω, the argument of pericentre ω, and the phase relative to the time of maximum displacement ϕ. The geometry of a 3D elliptical motion represented by these elliptical elements is shown in Figure 33.

In a novel work, Pinnegar (2006) derived expressions to calculate the Fourier coeffi-

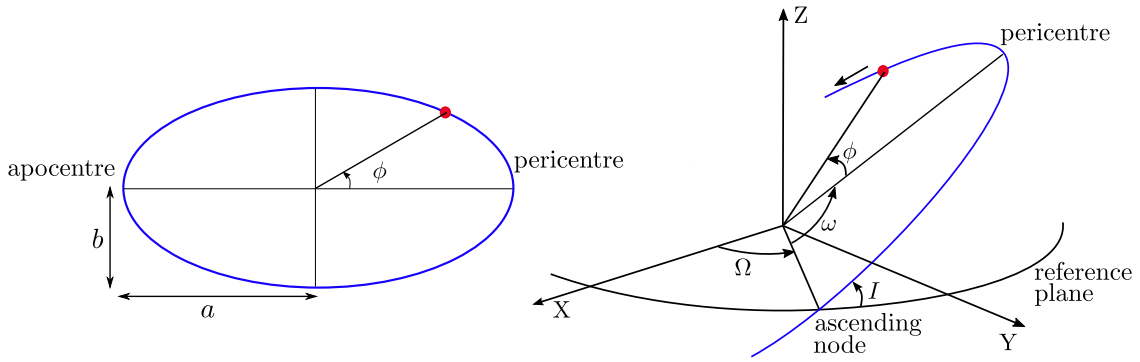

Figure 33. Geometry of the 3D elliptical motion. The particle's displacement traces out and ellipse with semi-major axis a, semi-minor axis b, inclination angle I, longitude of ascending node Ω , argument of pericentre ω, and phase ϕ.

cients from the spectra of elliptical elements and vice versa. In this section, the work presented by Pinnegar (2006) will be followed to illustrate the method.

Let us denote the 3C seismic trace by $\mathbf{u}(t) = \{u_x(t), u_y(t), u_z(t)\}$, where $u_x(t)$, $u_y(t)$ and $u_z(t)$ are the x-, y- and z-component, respectively. The 3C seismic trace can also be represented in the frequency domain by $\mathbf{U}(f) = \{U_x(f), U_y(f), U_z(f)\}$ where $\{U_x(f), U_y(f), U_z(f)\}$ are the Fourier transform of every single component $\{u_x(t), u_y(t), u_z(t)\}$. These Fourier spectra are complex-valued functions such that

$$U_j(f) = U_j^R(f) + iU_j^I(f) \quad \text{for } j = \{x, y, z\}, \tag{77}$$

where U_j^R and U_j^I denote the real and imaginary part of the Fourier spectrum, respectively.

For one specific frequency f, an ellipse on the $x - y$ plane can be expressed like

$$\mathbf{U}'(f) = \{a(f)\cos(2\pi ft - \phi(f)), b(f)\sin(2\pi ft - \phi(f)), 0\}\,. \tag{78}$$

In this equation, the semi-major axis is oriented along the x-axis, while the semi-minor axis is oriented along the y-axis. An arbitrary orientation of the ellipse can be obtained by applying matrix rotations as follows:

$$\mathbf{U}(f) = P_\Omega P_I P_\omega \mathbf{U}'(f) \tag{79}$$

where

$$P_\omega = \begin{bmatrix} \cos\omega(f) & -\sin\omega(f) & 0 \\ \sin\omega(f) & \cos\omega(f) & 0 \\ 0 & 0 & 1 \end{bmatrix},$$

$$P_I = \begin{bmatrix} 1 & 0 & 0 \\ 0 & \cos I(f) & -\sin I(f) \\ 0 & \sin I(f) & \cos I(f) \end{bmatrix},$$

and

$$P_\Omega = \begin{bmatrix} \cos\Omega(f) & -\sin\Omega(f) & 0 \\ \sin\Omega(f) & \cos\Omega(f) & 0 \\ 0 & 0 & 1 \end{bmatrix},$$

are transformation matrices used to represent the orientation of the ellipse.

The forward and inverse expressions for elliptical elements were derived by Pinnegar (2006). In the forward expressions, the data spectra $\mathbf{U} = \{U_x^R, U_x^I, U_y^R, U_y^I, U_z^R, U_z^I\}$ are obtained from the spectra of elliptical elements $\{a, b, \Omega, I, \omega, \phi\}$ as follows:

$$
\begin{aligned}
U_x^R =& a\cos\varphi\{\cos\omega\cos\Omega - \sin\omega\sin\Omega\cos I\} + b\sin\varphi\{\sin\omega\cos\Omega + \cos\omega\sin\Omega\cos I\} \\
U_x^I =& b\cos\varphi\{\sin\omega\cos\Omega + \cos\omega\sin\Omega\cos I\} - a\sin\varphi\{\cos\omega\cos\Omega - \sin\omega\sin\Omega\cos I\} \\
U_y^R =& a\cos\varphi\{\cos\omega\sin\Omega + \sin\omega\cos\Omega\cos I\} + b\sin\varphi\{\sin\omega\sin\Omega - \cos\omega\cos\Omega\cos I\} \\
U_y^I =& b\cos\varphi\{\sin\omega\sin\Omega - \cos\omega\cos\Omega\cos I\} - a\sin\varphi\{\cos\omega\sin\Omega + \sin\omega\cos\Omega\cos I\} \\
U_z^R =& a\cos\varphi\sin\omega\sin I - b\sin\varphi\cos\omega\sin I \\
U_z^I =& -a\sin\varphi\sin\omega\sin I - b\cos\varphi\cos\omega\sin I
\end{aligned}
\quad . \tag{80}
$$

On the other hand, in the inverse expressions, the spectra of elliptical elements $\{a, b, \Omega, I, \omega, \phi\}$ are obtained from the spectra of data $\mathbf{U} = \{U_x^R, U_x^I, U_y^R, U_y^I, U_z^R, U_z^I\}$ as follows:

$$
\begin{aligned}
a =& \frac{1}{\sqrt{2}}\sqrt{A+\sqrt{B^2+C^2}},\\
b =& \frac{1}{\sqrt{2}}\sqrt{A-\sqrt{B^2+C^2}},\\
I =& \arctan\left\{\frac{\left[\left(U_z^R U_y^I - U_z^I U_y^R\right)^2 + \left(U_z^R U_x^I - U_z^I U_x^R\right)^2\right]^{1/2}}{\left(U_y^R U_x^I - U_y^I U_x^R\right)}\right\},\\
\Omega =& \arctan\left\{\frac{\left(U_z^R U_y^I - U_z^I U_y^R\right)}{\left(U_z^R U_x^I - U_z^I U_x^R\right)}\right\},\\
\omega =& \omega_0 - \pi\left(\frac{\operatorname{sign}(\omega_0)-1}{2}\right),\\
\varphi =& \varphi_0 + \pi\left(\frac{\operatorname{sign}(\omega_0)-1}{2}\right)\operatorname{sign}(\varphi_0),
\end{aligned}
\tag{81}
$$

where

$$
\begin{aligned}
A =& \left(U_x^R\right)^2 + \left(U_x^I\right)^2 + \left(U_y^R\right)^2 + \left(U_y^I\right)^2 + \left(U_z^R\right)^2 + \left(U_z^I\right)^2,\\
B =& \left(U_x^R\right)^2 - \left(U_x^I\right)^2 + \left(U_y^R\right)^2 - \left(U_y^I\right)^2 + \left(U_z^R\right)^2 - \left(U_z^I\right)^2,\\
C =& -2\left(U_x^R U_x^I + U_y^R U_y^I + U_z^R U_z^I\right),\\
\omega_0 =& \arctan\left\{\frac{b\left[U_z^R\cos(\varphi_0) - U_z^I\sin(\varphi_0)\right]}{-a\left[U_z^R\sin(\varphi_0) + U_z^I\cos(\varphi_0)\right]}\right\},\\
\varphi_0 =& \frac{1}{2}\arctan\left(\frac{C}{B}\right)
\end{aligned}
\tag{82}
$$

For simplicity, lets define the operator Q to represent the forward expressions as follows:

$$\mathbf{U}(f) = Q\left\{a, b, I, \Omega, \omega, \phi\right\}. \tag{83}$$

Therefore, the inverse expressions can be written as:

$$\left\{a, b, I, \Omega, \omega, \phi\right\} = Q^{-1}\left\{\mathbf{U}(f)\right\}. \tag{84}$$

Additional seismic attributes can be computed from the elliptical elements. In this study, the power spectrum P and the ellipticity e are analyzed, and they are computed using Equations 85 and 86, respectively.

$$P = \sqrt{a^2 + b^2}. \tag{85}$$

$$e = \begin{cases} 0 & \text{if } a < \epsilon \\ b/a & \text{otherwise} \end{cases}. \tag{86}$$

The parameter ϵ is an small positive number used to avoid division by zero.

The forward and inverse expressions of elliptical elements representation can be also performed in the (f, p) domain by substituting $\mathbf{U}(f, p)$ in place of $\mathbf{U}(f)$ in equation 83 and 84.

4.5. Frequency-slowness polarization filter for 3C data (3C-FSPF)

Seismic data include several events, such as reflections, refractions, surface waves, direct waves, and scattering. In this study, the 3C seismic data $\mathbf{u}(t,h)$ is assumed to be a summation of events from various wave types, represented as follows:

$$\mathbf{u}(t,h) = \sum_{\Upsilon} \mathbf{u}^{\Upsilon}(t,h). \tag{87}$$

Here, Υ denotes each one of the specific wave types. It is postulated that each wave type exhibits unique polarization characteristics within a limited and exclusive area of the (f,p) domain. As a result, it becomes possible to identify and separate each wave type in this domain.

In this research, a filter mask $F(f,p)$ is proposed to extract a particular wave type. The filter utilizes polarization analysis with elliptical elements in the (f,p) domain to achieve the separation of the specific wave type, as follows:

$$\hat{\mathbf{u}}^{\Upsilon}(t,h) = IR\{Q(aF, bF, I, \Omega, \omega, \phi)\}, \tag{88}$$

where $\hat{\mathbf{u}}^{\Upsilon}$ represent the extracted wave type Υ, while the notation IR represents the inverse Radon transformation of the seismic data after filtering in the (f,p) domain.

To construct the filter mask, the fixed-parameter activation functions proposed by Pinnegar (2006) are adapted. Originally, these functions were designed specifically for ex-

tracting Rayleigh waves. However, the suggested approach involves using these functions with variable parameters, allowing for adaptation to different polarization characteristics for any wave type. The filter mask F is then created using the activation functions F_e, F_Ω, and F_I as follows:

$$F(f,p) = F_e(e(f,p))F_\Omega(\Omega(f,p))F_I(I(f,p)). \tag{89}$$

Here, F_e, F_Ω, and F_I are the activation functions for ellipticity, longitude of ascending node, and inclination angle, respectively. Let's elaborate these functions further:

The activation function

$$F_e(e;e_1,e_2) = \begin{cases} 0 & \text{if } e < e_1 \\ \frac{1}{2}\left[1+\cos\left(\pi\frac{e-e_2}{e_2-e_1}\right)\right] & \text{if } e_1 \le e \le e_2\,, \\ 1 & \text{if } e > e_2 \end{cases} \tag{90}$$

is designed to attenuate wave type events with ellipticities lower than e_1 and preserve energy with ellipticities higher than e_2. There's a transition region between these values, as depicted in Figure 34(a).

The activation function

$$F_\Omega(\Omega;\Omega_c,\Omega_1,\Omega_2)=\begin{cases}0 & \text{if } |\Omega-\Omega_c|>\Omega_2\\ \frac{1}{2}\left[1-\cos\left(\pi\frac{|\Omega-\Omega_c|-\Omega_2}{\Omega_2-\Omega_1}\right)\right] & \text{if } \Omega_1\le|\Omega-\Omega_c|\le\Omega_2\\ 1 & \text{if } |\Omega-\Omega_c|<\Omega_1\end{cases}, \tag{91}$$

is intended to allow the passage of energy with an azimuth around Ω_c within a band pass of $2\Omega_1$ and $2\Omega_2$, taking the transition region into account (see Figure 34(b)). Similarly, the activation function F_I lets the energy pass with an inclination angle around I_c within a band pass of $2I_1$ and $2I_2$, again considering the transition region (see Figure 34(c)).

$$F_I(I;I_c,I_1,I_2)=\begin{cases}0 & \text{if } |I-I_c|>I_2\\ \frac{1}{2}\left[1-\cos\left(\pi\frac{|I-I_c|-I_2}{I_2-I_1}\right)\right] & \text{if } I_1\le|I-I_c|\le I_2\\ 1 & \text{if } |I-I_c|<I_1\end{cases}. \tag{92}$$

To implement the filter mask using all these activation functions, eight parameters must be tuned. However, for recovering certain wave types, the use of all the activation functions may not be necessary. Furthermore, these activation functions can be inverted for different effects. For instance, replacing F_e with $1-F_e$ allows the filter to reject energy with ellipticities higher than e_2 and preserve the energy lower than e_1.

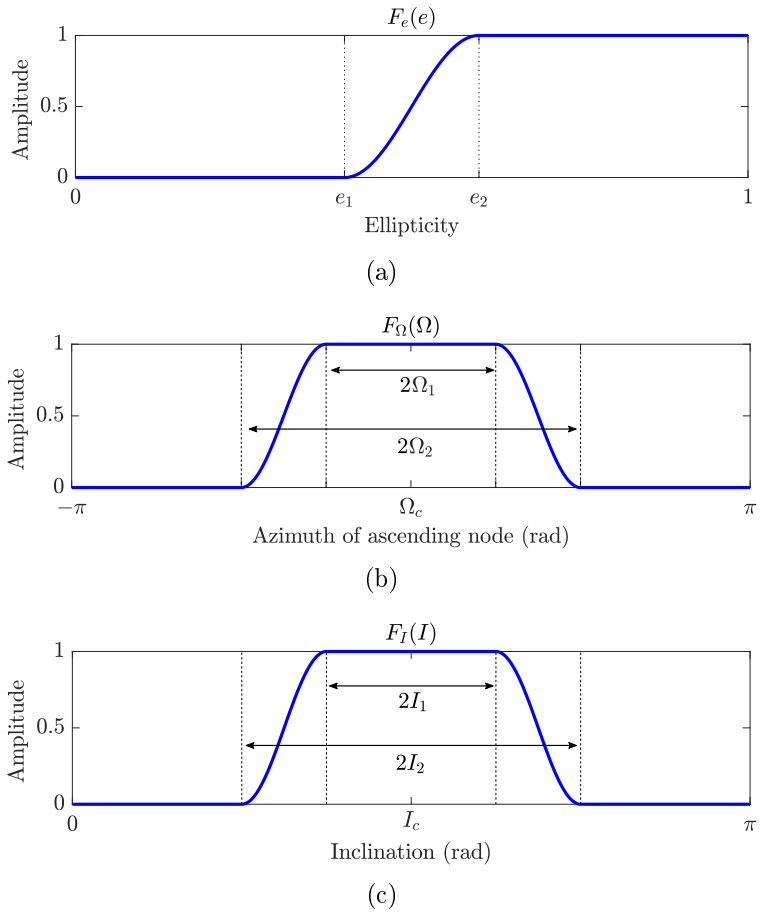

Figure 34. Activation functions employed in the 3C-FSPF mask construction. (a) function for ellipticity, (b) function for azimuth angle, and (c) function for inclination angle.

4.5.1. Implementation procedure:. The steps to implement the 3C-FSPF are presented below:

Step 1: Transform the seismic data from (t, h) domain to (f, p) domain. This is achieved by first applying the temporal Fourier transform and subsequently the High Resolution Linear Radon Transform (HRLRT), which is applied by solving equation (76).

Step 2: Determine the elliptical elements using the inverse expressions provided in equation

(81).

Step 3: Design a polarization filter mask by setting the parameters as detailed in equation (89).

Step 4: Calculate the Radon model of the filtered data. This is done by using the inverse expressions provided in equation (80) after applying the polarization filter mask to both the semi-major and semi-minor elements in the frequency-slowness domain (f, p) as specified in equation (89).

Step 5: Transform the filtered seismic data back to the (t, h) domain. This involves using the forward Linear Radon Transform (LRT) operator as mentioned in equation (72), followed by the application of the inverse Fourier transform.

4.6. Example 1: Separation of polarized wavefields in a synthetic 3C shot gather

In this example, a synthetic dataset generated analytically was used to demonstrate the operation and feasibility of the proposed method under both regular and irregular spatial sampling data. Specifically, the synthetic 3C data $\mathbf{u}(t, x)$ was produced by combining two plane wavefields with different polarizations:

$$\mathbf{u}(t, x) = \mathbf{u}^E(t, x) + \mathbf{u}^L(t, x), \tag{93}$$

where $\mathbf{u}^E(t, x)$ is an elliptically polarized wavefield, while $\mathbf{u}^L(t, x)$ is a linearly polarized wavefield. These wavefields were generated in the frequency domain following the expression:

$$\mathbf{U}(f, x) = \mathbf{A}(f)e^{-i2\pi f(t_0+px)}, \tag{94}$$

where p represents the apparent slowness of the plane wavefield along the x-axis, while t_0 refers to the shift time from the reference time of $t = 0$. To calculate the 3C vector amplitude $\mathbf{A}(f)$, the semi-major axis a and semi-minor axis b are rotated using the matrices P_Ω, P_I, and P_ω, as follows:

$$\mathbf{A}(f) = P_\Omega P_I P_\omega \{a(f), b(f), 0\} \tag{95}$$

The semi-axes a and b are defined in the frequency domain as the product of a Ricker wavelet $R(f; fc)$, with central frequency f_c, and a Gaussian window function $W(f; f_\mu, f_\sigma)$, with mean frequency f_μ and standard deviation f_σ

$$\begin{aligned} a(f) =& C_a R(f; f_c) W(f; f_\mu, f_\sigma), \\ b(f) =& C_b R(f; f_c) W(f; f_\mu, f_\sigma), \end{aligned} \tag{96}$$

where C_a and C_b are positive scalars utilized to control the amplitude spectrum of each semi-axis, with the constraint that $C_a \geq C_b$. The ratio C_b/C_a determines the degree of ellipticity of the polarized wavefield. As the ratio approaches zero, the polarization becomes increasingly linear. Conversely, as the ratio approaches one, the polarization becomes more circular.

The expressions for the Ricker and the Gaussian window function are:

$$\begin{aligned} R(f;f_c) =& \frac{2}{\sqrt{\pi}}\frac{f^2}{f_c^3}e^{-(f/f_c)^2}, \\ W(f;f_\mu,f_\sigma) =& e^{-(f-f_\mu)/2f_\sigma^2}. \end{aligned} \tag{97}$$

The purpose of the Gaussian window function is to compact the frequency spectrum of the Ricker wavelet, resulting in more distinct and separable wavefields in the (f,p) domain. Additionally, using the expression in the equation 94 ensures that the resulting wavefields are non-dispersive and non-evanescent since p is a real value that does not depend on f.

Table 7 presents the elliptical elements used to generate the polarized wavefields in this example. The elliptically polarized wavefield has an ellipticity of $C_b/C_a = 0.8$, while the linear wavefield has an ellipticity of $C_b/C_a = 0.1$. For the linear wavefield, the parameters used were $p = 2.5 \times 10^{-3}$ (s/m), $t_0 = 0.4$ (s), $f_c = 15$ (Hz), $f_\mu = 15$ (Hz), and $f_\sigma = 3$ (Hz). For the elliptical wavefield, the following parameters were used: $p = 2 \times 10^{-3}$ (s/m), $t_0 = 0.3$ (s), $f_c = 8$ (Hz), $f_\mu = 8$ (Hz), and $f_\sigma = 2$ (Hz).

Table 7
Elliptical elements for generating linearly and elliptically polarized wavefields in the synthetic data example.

Wavefield type	C_a	C_b	ω (rad)	Ω (rad)	I (rad)
Linear polarized (event A)	10	1	$3\pi/5$	$\pi/5$	$\pi/3$
Elliptical polarized (event B)	10	8	$\pi/2$	$\pi/3$	$2\pi/3$

The resultant linear and elliptical wave types in the (t,x) domain are showcased in Figures 35(a) and 35(b) respectively, while Figure 35(c) presents the total wavefield. These

datasets were generated under a scheme of regular spatial sampling with an inter-receiver distance maintained at 1 m. The hodogram of the first trace reveals the differences between the linearly polarized wavefield (in red) and the elliptically polarized one (in blue), as seen in Figure 36(a). Conversely, the hodogram corresponding to the total wavefield (Figure 36(b)) reveals an irregular polarization, complicating the distinction between the linear and elliptical wave types (Figure 36(b)).

To separate the wave types using the proposed method, a polarization analysis is necessary. Thus, the synthetic 3C data is represented using elliptical elements within the (f, p) domain, employing equations 81 and 82. The analysis in this domain required the computation of the HRLRT for each single component, setting the parameters to $p_0 = 0$ (s/m), $\Delta p = 2 \times 10^{-5}$ (s/m), and $N_p = 251$ samples. When inspecting the (f, p) spectrum of the semi-major axis, two distinct events are identified (A and B). These events are associated with linear and elliptical polarized wave types, respectively (see Figure 37(a)). On one-dimensional projection, the energy of these events overlaps in both frequency and slowness, necessitating a 2D filter mask for successful wavefield separation. Upon assessing the (f, p) spectrum for the semi-minor axis, as illustrated in Figure 37(b), an expected pattern is observed. Here, the linear polarized wave type, classified as event A, consistently demonstrates lower values in comparison to its elliptical counterpart, labeled as event B. This discrepancy indicates a distinct differentiation between these two wave types within the (f, p) spectrum.

Further, the (f, p) spectra of the inclination (I), argument (ω), and azimuth (Ω) angles produce polarization analysis results consistent with the information in Table 7. This

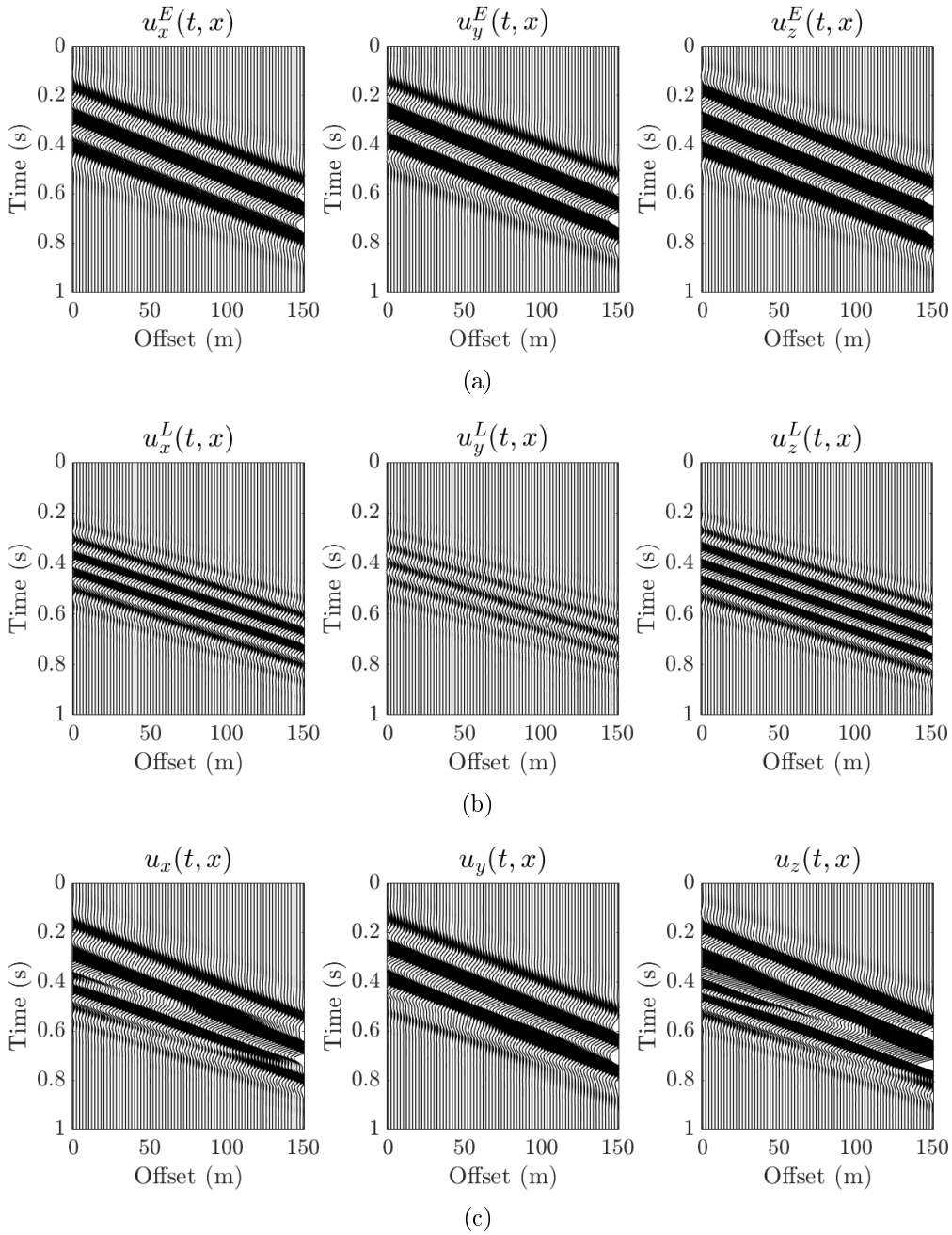

Figure 35. Multicomponent shot gather of (a) Elliptically linearly polarized wavefield $\mathbf{u}^E(t,x)$, (b) Linearly polarized wavefield $\mathbf{u}^L(t,x)$, and (c) total wavefield $\mathbf{u}(t,x) = \mathbf{u}^E(t,x) + \mathbf{u}^L(t,x)$

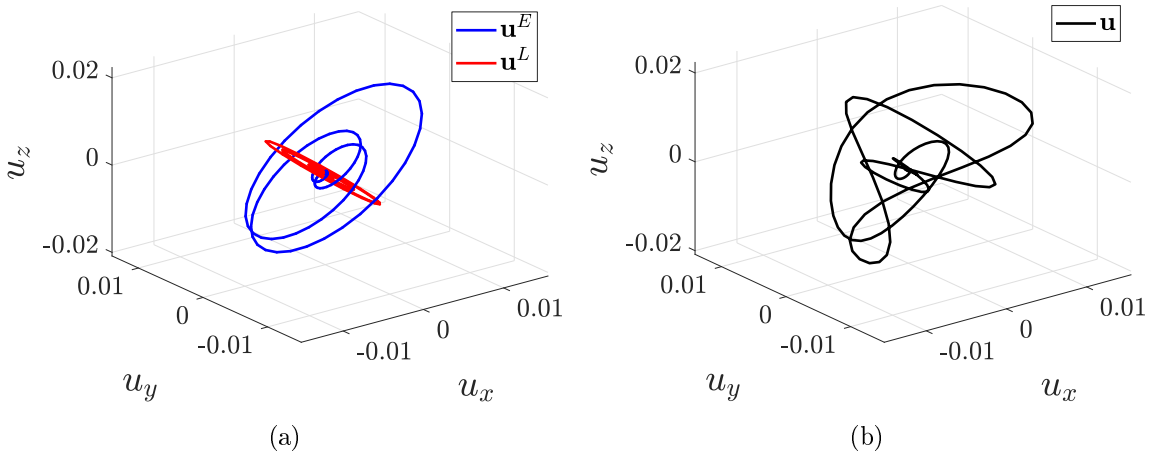

Figure 36. Hodogram for the first trace of the 3C synthetic shot gather. (a) Elliptically polarized wavefield represented in blue, and linearly polarized wavefield represented in red; (b) Total wavefield.

consistency is reflected in Figures 37(c), 37(d), and 37(e), respectively. On the other hand, instability in the phase ϕ behavior is observed (see Figure 37(f)). Although ϕ does not significantly contribute to the polarization analysis, as it does not function as a parameter in determining the ellipse's orientation traced by the particle motion, it is nonetheless important. As the defining phase for the elliptical trajectory, is necessary to reconstruct the multicomponent data. Moreover, using equations 85 and 86, the power spectrum and ellipticity are computed, respectively. Observations from Figure 37(h) reveal a higher power spectrum for event B (representing the elliptically polarized wave type) compared to event A (indicative of the linearly polarized wave type). Further, the (f, p) spectrum of the ellipticity exhibits higher values within the elliptically polarized wave type zone and lower values in the linearly polarized wave type zone (Figure 37(g)).

Based on the results of the polarization analysis, the 3C-FSPF workflow was followed

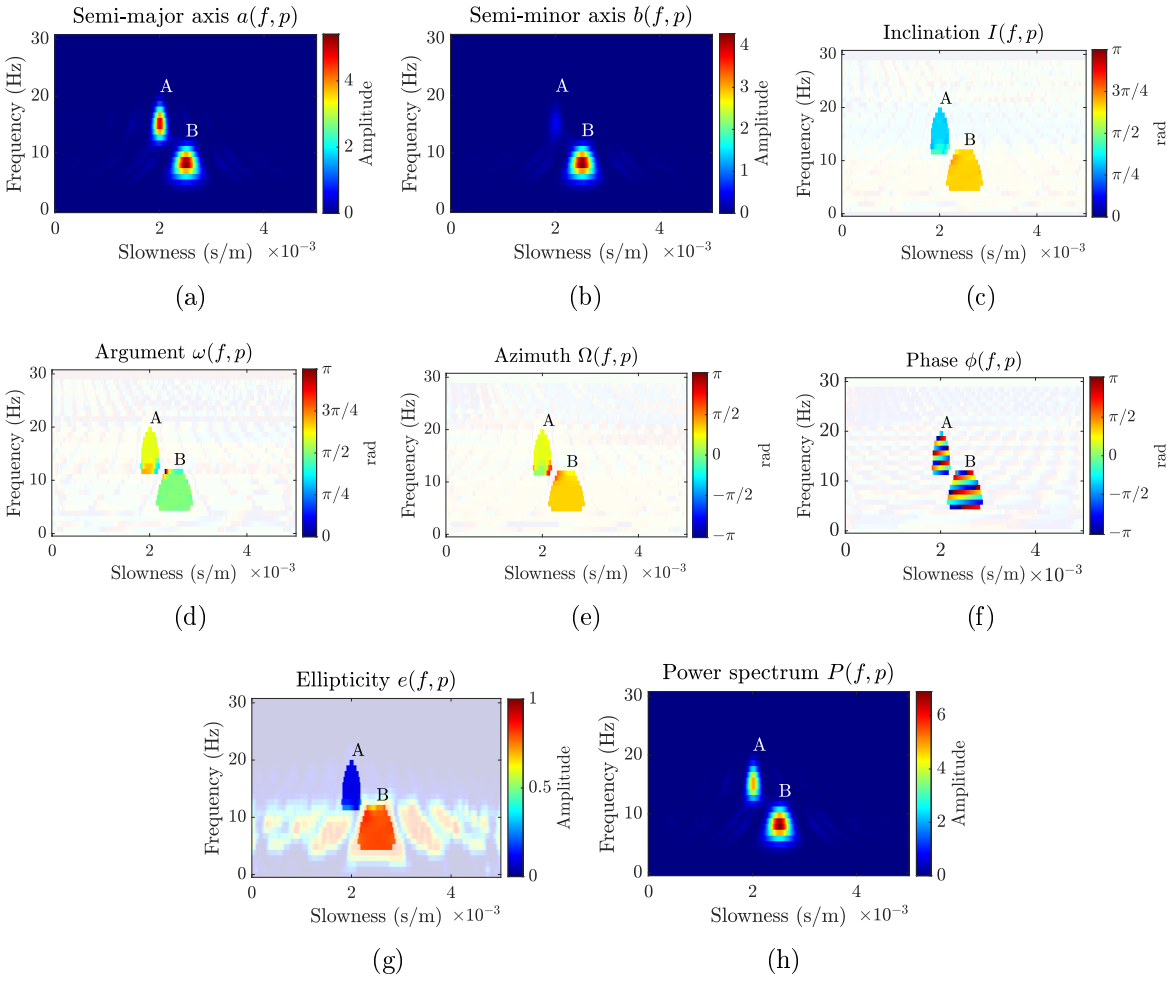

Figure 37. Spectra of elliptical elements in the (f,p) domain, derived via HRLRT from the synthetic data in Figure 35(c): (a) Semi-major axis a, (b) semi-minor axis b, (c) inclination I, (d) argument of pericentre ω, (e) azimuth of ascending node Ω, (f) phase ϕ, (g) ellipticity e, and (h) power spectrum P.

to selectively extract the elliptically polarized wave type. The 3C-FSPF mask was created by using the activation function for ellipticity F_e with $e_1 = 0.2$ and $e_2 = 0.3$. These values were strategically chosen after a thorough examination of the (f,p) spectrum of ellipticity, as showcased in Figure 37(g). The resulting (f,p) domain filter mask is illustrated in Figure 38.

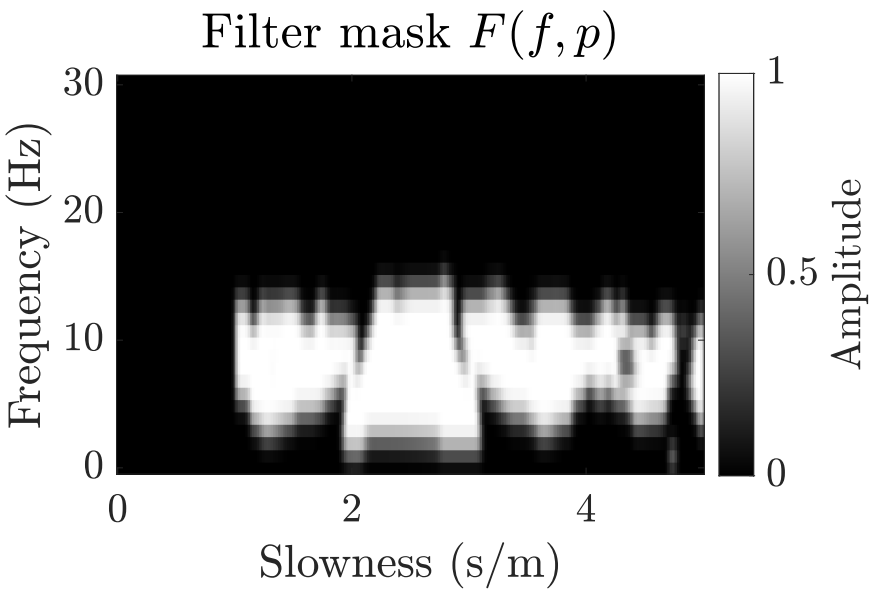

Figure 38. 3C-FSPF mask $F(f,p)$ utilizing the activation function for ellipticity F_e with $e_1 = 0.2$ and $e_2 = 0.3$.

Figure 39(a) shows the elliptically polarized wavefield extracted by 3C-FSPF. A comparison of the data displayed in Figure 39(a) with that in Figure 35(a) reveals a marked similarity between the wavefield extracted by the 3C-FSPF and the true elliptical wavefield. In order to derive the linearly polarized wavefield, the previously predicted elliptically polarized wavefield was subtracted from the original data. The resultant data displayed in Figure 39(b) closely mirrors the true linearly polarized wave type, as can be seen in Figure 35(b). To obtain the linearly polarized wavefield, we subtracted the extracted elliptically polarized wavefield from the data. The resulting data predicted by the 3C-FSPF is also similar to the true data (Figure 35(b)). To quantify the degree of similarity between the predicted $\hat{u}_i$ and the true data u_i^0 within each component $i = (x, y, z)$, the prediction gain G_i (in dB) was calculated using Equation 98. This measure allowed us to gauge the effectiveness of the

method in accurately predicting the polarized wavefields.

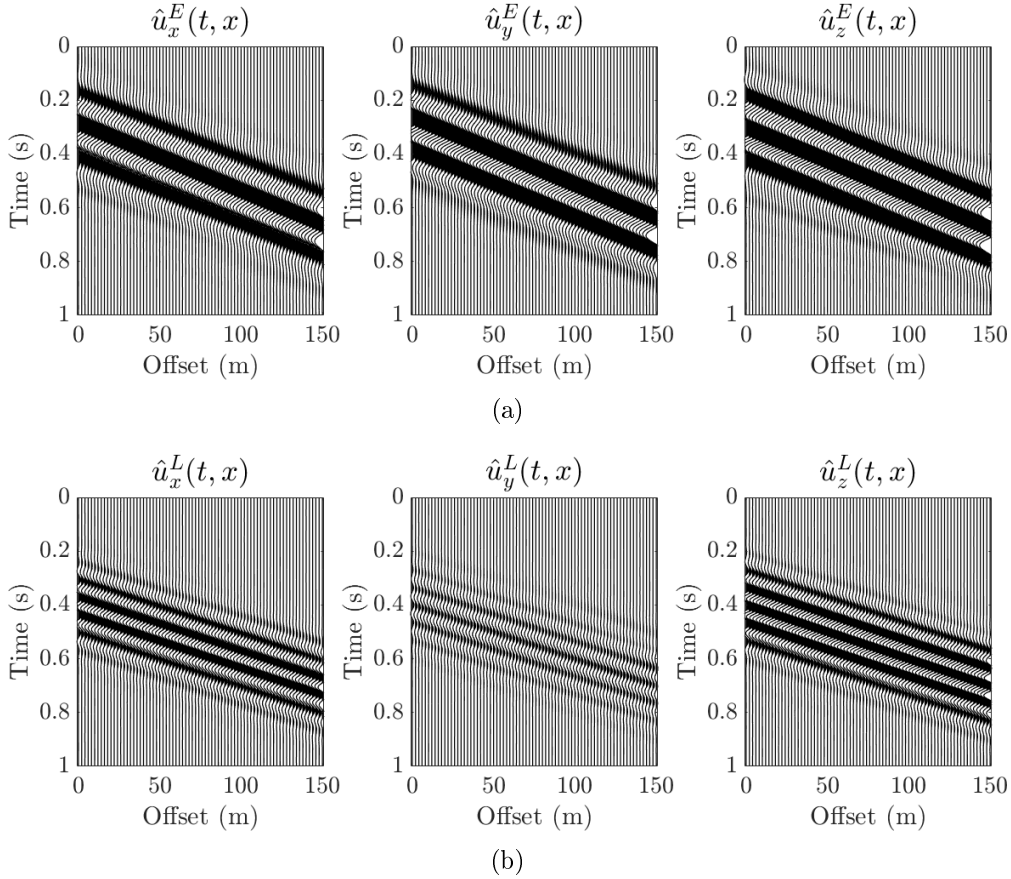

Figure 39. Multicomponent synthetic shot gather after filtering. (a) Elliptically polarized wavefield, extracted using 3C-FSPF, and (b) Linearly polarized wavefield, computed as the difference between the total wavefield in (Figure 35(c)) and the extracted polarized wavefield in (a).

$$G_i(\text{dB}) = 10\log_{10}\frac{\sum_{n=0}^{N_t-1}\sum_{j=0}^{N_x-1}\left[u_i^0(t_n,x_j)\right]^2}{\sum_{n=0}^{N_t-1}\sum_{j=0}^{N_x-1}\left[u_i^0(t_n,x_j)-\hat{u}_i(t_n,x_j)\right]^2} \tag{98}$$

The results in Table 8 shows the 3C-FSPF's performance in terms of prediction gains. Specifically, when predicting the elliptical wave type, the method achieved prediction gains exceeding 27 dB across all components, with a peak value of 33.46 dB registered in the

y-component. Meanwhile, in the case of predicting the linearly polarized wavefield, the 3C-FSPF managed to achieve prediction gains surpassing 17 dB for all components, though these gains receded to a minimum of 17.62 dB within the y-component.

Table 8
Prediction gains obtained after extraction of polarized wavefileds using 3C-FSPF.

Wavefield type	G_x (dB)	G_y (dB)	G_z (dB)
Elliptical	27.93	33.46	27.65
Linear	21.95	17.62	22.10

4.6.1. Analysis with spatial undersampling and noise. The proposed method was also evaluated under non-ideal conditions with irregular spatial sampling. The same wavefields were recreated as depicted in Figure 35(a), Figure 35(b), and Figure 35(c), but under the assumption that the inter-receiver distance, denoted as $\Delta x = x_{j+1} - x_j$, followed a normal distribution with a mean of 1 m and a standard deviation of 0.3 m. Furthermore, the traces were decimated by varying percentages, ranging from 0 % to 80 %, and at different Signal-to-Noise Ratio (SNR) levels of 1.0, 0.9, 0.8, and 0.5. The findings indicated that the prediction gain of the extraction of the elliptically polarized wave type, as derived using 3C-FSPF, is influenced by the presence of missing traces and the level of noise. More specifically, when SNR levels were less than 1.0, the prediction gain exhibited a slow decay as the level of decimation increased (Figure 40). Interestingly, in the scenario where SNR = 1.0, it was observed that the prediction gain on a shot gather with missing traces could exceed that of a full receivers shot gather. It's crucial to note, however, that in this analysis the computation of prediction gain with Equation 98 is only performed over

existing traces, excluding any missing traces.

Figure 41(a) presents an example of a noisy shot gather exhibiting irregular spatial sampling and missing traces. In this particular example, the data maintains a Signal-to-Noise Ratio (SNR) of 0.8 and has undergone 60 % trace decimation. Despite these challenges, the application of 3C-FSPF successfully isolated the elliptically polarized wave type. The filtered shot gather, displayed in Figure 41(c), demonstrates notable resemblance to the true elliptical wavefield (refer to Figure 41(b)). It is important to note that while the predicted data is largely free of noise, it may still contain artifacts to some extent.

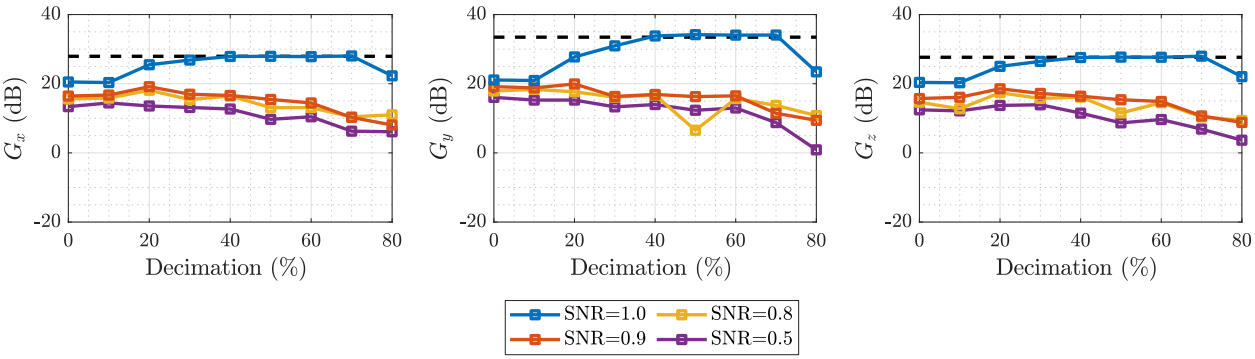

Figure 40. Prediction gains for reconstructed elliptically polarized wavefield in irregularly sampled synthetic data. The inter-receiver distance follows a normal distribution with a mean of 1 m and a standard deviation of 0.3 m. The gains G_x, G_y, and G_z were calculated under varying percentages of trace decimation and different Signal-to-Noise Ratio (SNR) levels. The dashed black line corresponds to the prediction gain from data with regular sampling and without the influence of noise.

4.7. Example 2: Separation of near-surface waves in a synthetic-modeled 3C shot gather.

In this second example, synthetic data was generated through elastic wave modeling, utilizing the rectangular finite-difference code introduce in chapter 2 to resolve the free-

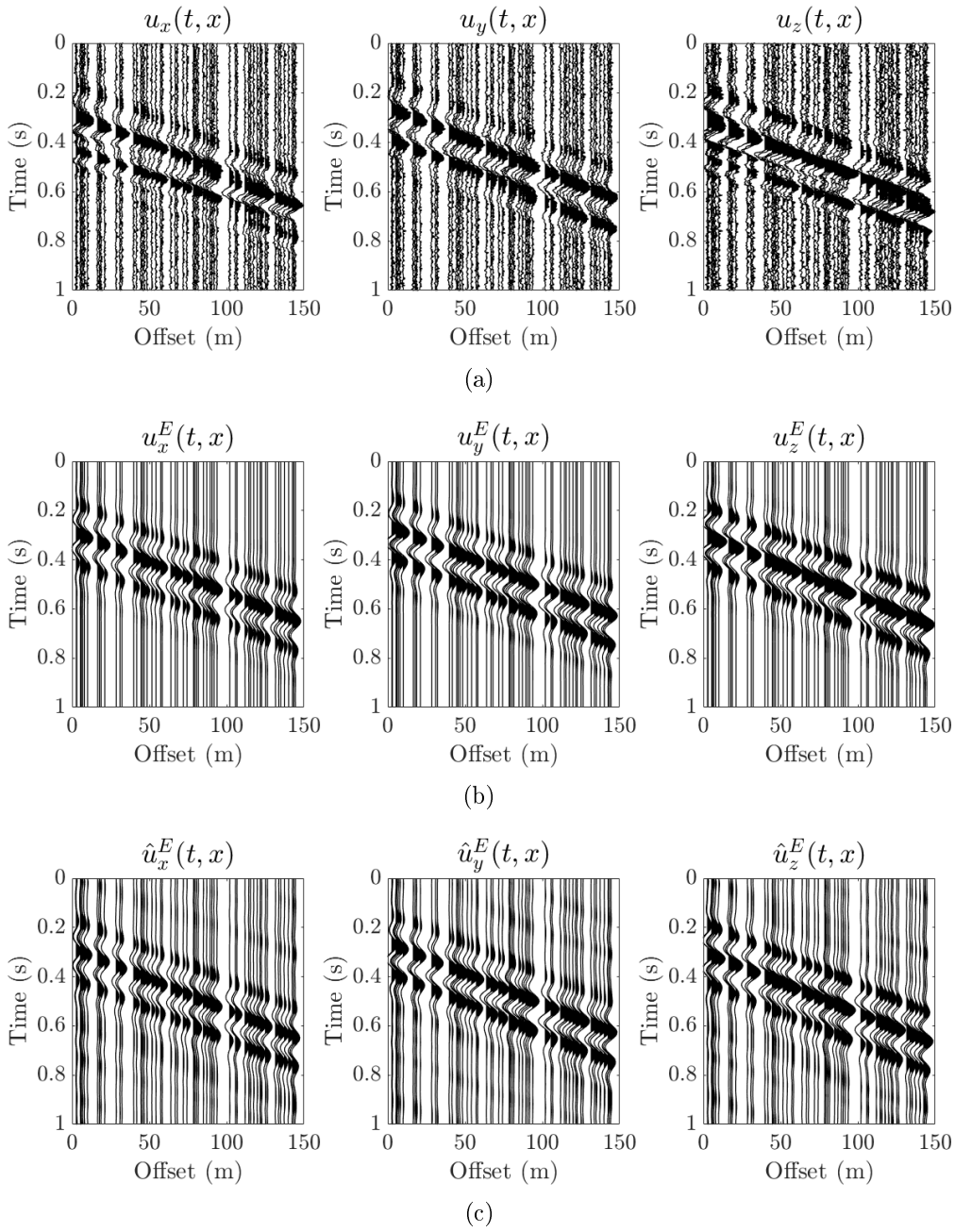

Figure 41. Example of a multicomponent shot gather of synthetic data irregularly sampled with SNR=0.8 and 60 % trace decimation. (a) Total wavefield, (b) True elliptical wavefield, and (c) Elliptical wavefield extracted by 3C-FSPF.

surface condition. A two-layered homogeneous model with a spherical heterogeneity was used, as depicted in Figure 42. Parameters for the medium in each layer, as well as for the heterogeneity, are specified in Table 18. The acquisition geometry was configured with an explosive source on the surface at $x = 0.5$ (km) and $y = 1$ (km). Additionally, a 3C vector sensor array was installed on the surface at y=1 (km), extending between x=0.5 (km) and x=3 (km), with an inter-receiver distance of 10 (m).

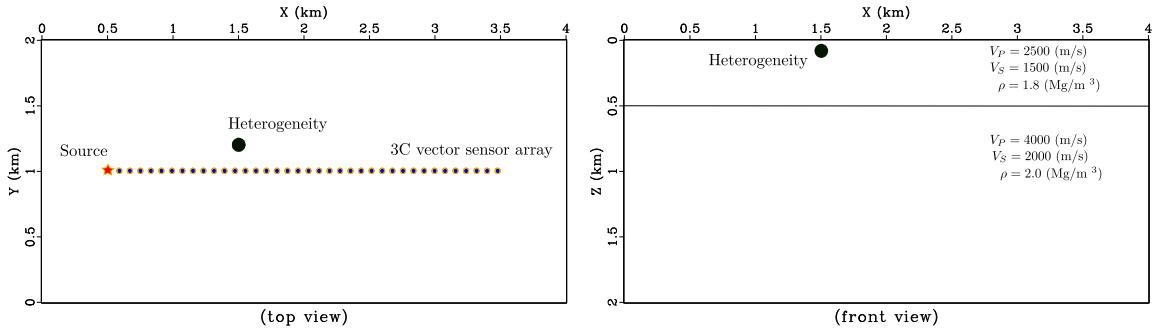

Figure 42. 2D-3C acquisition geometry for the modeled data of example 2. (a) Top view . (b) Front view. An spherical heterogeneity with radius 0.05 km is located in the top layer at $(1.5, 1.2, 0.1)$ km. The elastic medium parameters for each region of the model are specified in Table 9

Table 9
Elastic medium parameters for earth model in Figure 42

Region	Thickness (km)	V_P (m/s)	V_S (m/s)	Density ρ (Mg/m^3)
Layer 1	0.5	2500	1500	1.8
layer 2	∞	4000	2000	2.0
Heterogeneity	-	3750	2250	2.5

In the resulting shot gather, distinct wave types can be readily discerned. The Rayleigh wave, body wave reflections, and direct waves are exclusive to the $x-$ and $z-$ components.

In contrast, near-surface scattering can be detected across all three components: x, y, and z, as demonstrated in Figure 43. These specific wave types are also discernible in the (f, p) spectra of elliptical elements, as depicted in Figure 44. The spectra were obtained through the application of the HRLRT for each individual component, using parameters set at $p_0 = -2 \times 10^{-3}$ (s/m), $\Delta p = 1 \times 10^{-5}$ (s/m), and $N_p = 401$ samples.

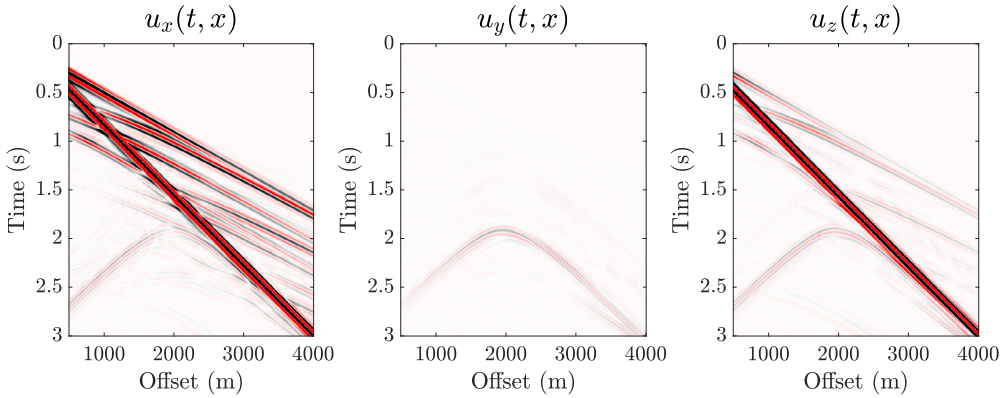

Figure 43. Multicomponent shot gather of modeled data acquired with the acquisition geometry in Figure 42.

In the (f, p) panels for both the semi-major axis (Figure 44(a)) and the semi-minor axis (Figure 44(a)), three distinct events (A, B, and C) can be identified. Event A corresponds to back-scattered waves, identifiable by its location in the region with negative slowness values. Event B, found in the area with slowness values ranging from 0 to 0.6 (s/m), is associated with body wave reflections. Lastly, event C is linked to Rayleigh waves due to its higher slowness values. Notably, it is observed that event C possesses a larger semi-minor axis compared to events A and B.

The inclination angle I within the region of event C displayed relative homogeneity, with values around $\pi/2$, as shown in Figure 44(c). On the other hand, the azimuth angle

Ω shows negative values in the region of event A and remains relatively constant around zero in the region of event C. This is consistent with theoretical expectations, considering that Rayleigh waves (event C) propagate along the source-receiver plane, while near-surface scattered waves (event A) approach the sensor array from outside this plane.

In the (f, p) panel of ellipticity (Figure 44(g)), smaller values occur in the region of body wave reflections (event B), indicating that energy in this region is predominantly linearly polarized. The back-scattered energy generated by the heterogeneity located proximate to the 3C vector sensor array (Figure 42(a)) exhibits lower amplitude compared to the waves related to events B and C (Figure 44(h)). This observation is attributed to the back-scattered waves being a product of the interaction of seismic waves with small-scale heterogeneities, which tend to scatter energy in multiple directions, consequently diminishing its amplitude.

Building on the polarization analysis conducted earlier, two filters were developed to separate the wave types in the 3C modeled data. The specific parameters for each filter are outlined in Table 10. The first filter, illustrated in Figure 45(a), is designed to isolate the Rayleigh wave by retaining the energy in the region of event C. This is achieved with parameters set as $e \geq 0.3$, $\Omega \sim 0$, and $I \sim 0$. The second filter, depicted in Figure 45(b), aims to predict near-surface scattered waves by preserving the energy associated with event A by rejecting the energy with $\Omega \sim 0$.

Upon applying the filters, it was found that the Rayleigh wave predicted by the 3C-FSPF (Figure 46(b)) closely aligns with the actual modeled Rayleigh wave (Figure 46(a)).

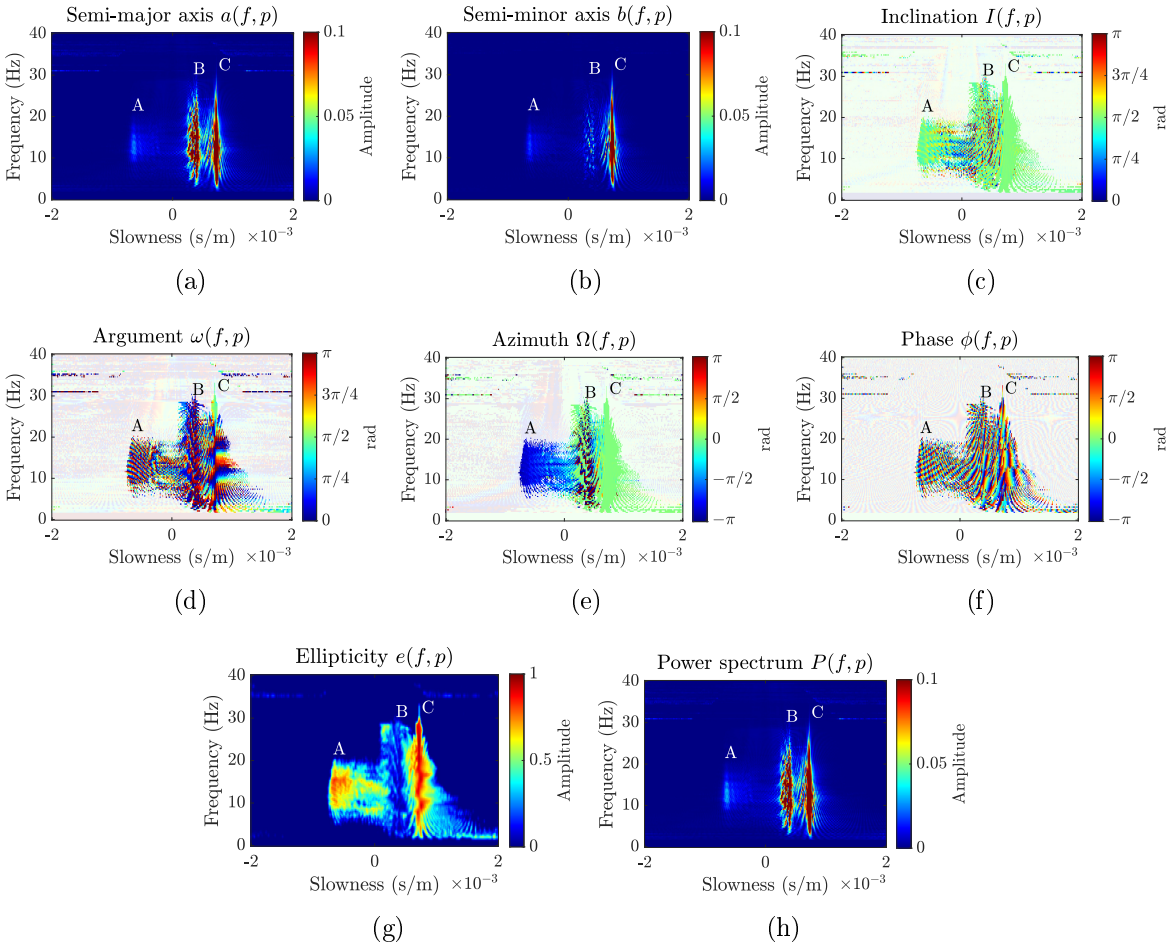

Figure 44. Spectra of elliptical elements in the (f,p) domain, derived via HRLRT from the synthetic data in Figure 43: (a) Semi-major axis a, (b) semi-minor axis b, (c) inclination I, (d) argument of pericentre ω, (e) azimuth of ascending node Ω, (f) phase ϕ, (g) ellipticity e, and (h) power spectrum P.

Table 10
Filter parameters of 3C-FSPF to separate the wave type from the 3C modeled data in Figure 43 .

Wave type	Filter mask	e_1	e_2	Ω_c	Ω_1	Ω_2	I_c	I_1	I_2
Rayleigh	$F_e F_\Omega F_I$	0.2	0.3	0	$\pi/10$	$\pi/5$	$\pi/2$	$\pi/10$	$\pi/5$
Near-surface scattered	$1 - F_\Omega$	0.2	0.3	0	$\pi/10$	$\pi/5$	-	-	-

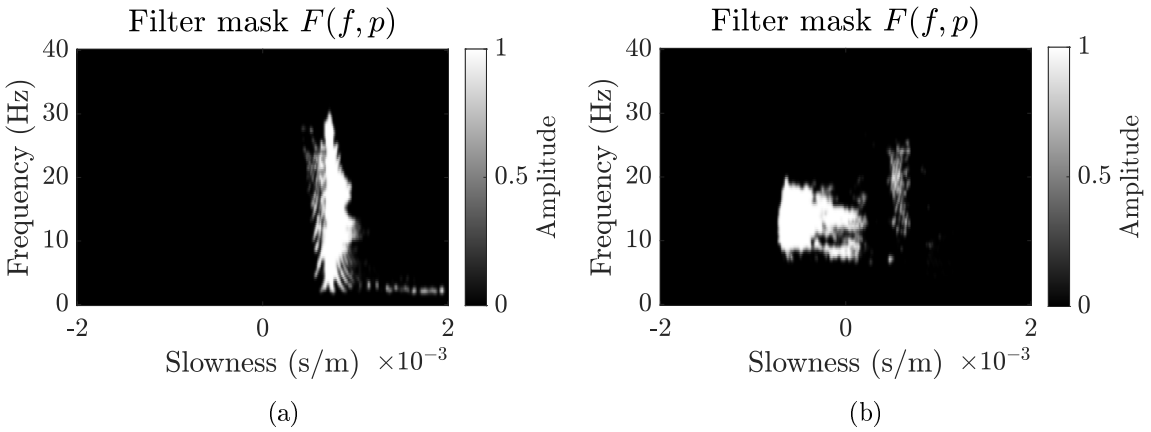

Figure 45. Design of 3C-FSPF masks in the (f,p) domain for wave type extraction from 3C modeled data displayed in Figure 12. These include: (a) a mask for Rayleigh wave extraction, and (b) a mask for near-surface scattered wave extraction. Corresponding parameters for each filter mask are detailed in Table 10.

Notably, some energy associated with the near-surface scattering persists in the $y-$ component.

Regarding the near-surface scattering, the observations indicate that the 3C-FSPF accurately predicts the portion of the energy with a negative slope, whereas the energy with a positive slope is less precisely predicted (see Figure 47(a) and Figure 47(b)).

Ultimately, the predicted wavefields were subtracted from the 3C modeled data to extract the body-wave reflections and direct wave, as displayed in Figure 48(a). Upon comparison with the true body-wave wavefield (Figure 48(b)), it is apparent that a significant majority of the energy was accurately predicted, although some residual energy from near-surface scattering remains.

The prediction gains obtained for each wave type in each component are presented in Table 11. It is notable that the prediction gain for the Rayleigh wave is substantially

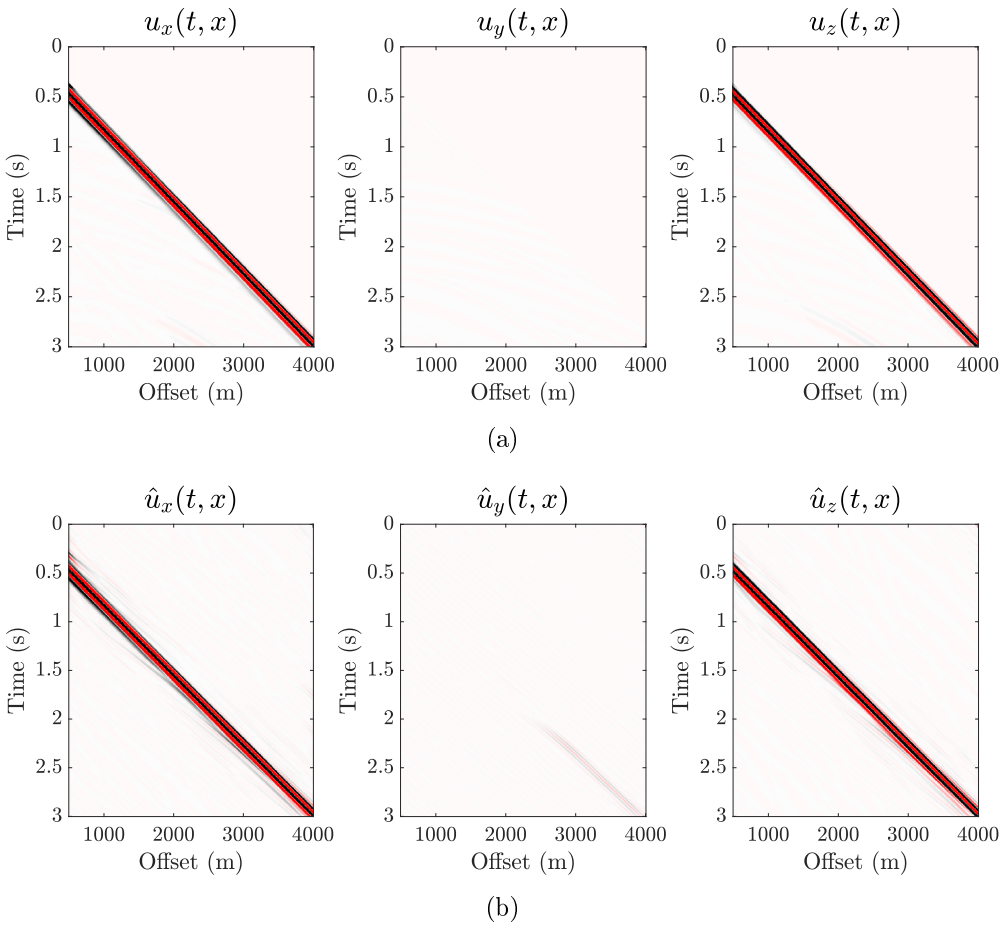

Figure 46. Extraction of Rayleigh wave from modeled data displayed in Figure 43. (a) True modeled Rayleigh wave. (b) The predicted Rayleigh wave obtained using the 3C-FSPF mask shown in Figure 45(a).

higher than for the other wave types (body waves and near-surface scattering). This could be attributed to the fact that a homogeneous layered velocity model is considered, resulting in a stable behavior of the Rayleigh wave that can be readily characterized in the (f, p) domain. On the other hand, the near-surface scattering was predicted with the lowest gain. This is because only the negative slope energy portion was extracted by the 3C-FSPF filter. It's also important to note that the prediction gain in the $y-$ component cannot be computed for the

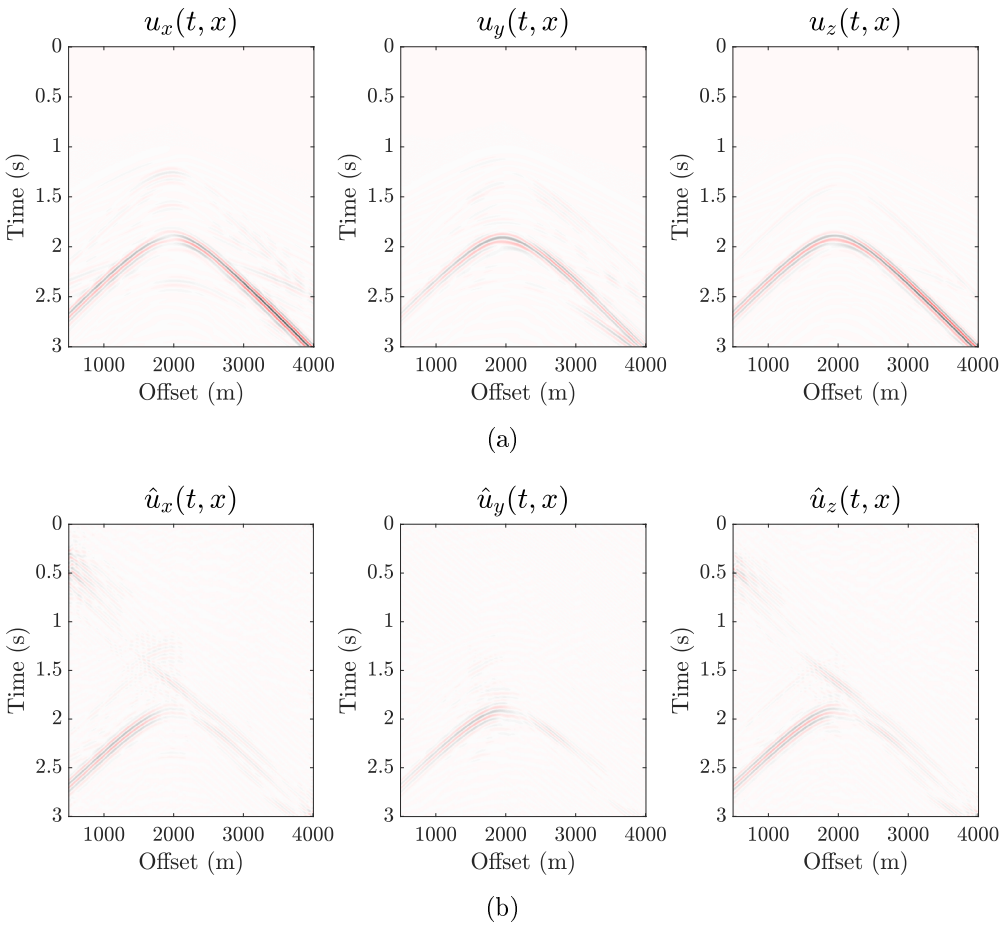

Figure 47. Extraction of near-surface scattered waves from modeled data displayed in Figure 43. (a) True modeled near-surface scattered waves. (b) The predicted near-surface scattered waves obtained using the 3C-FSPF mask shown in Figure 45(b).

Rayleigh wave and the body wave. This is due to the fact that the energy of the reference true wavefield in that component is zero.

4.7.1. Analysis with irregular spatial sampling and noise. In this example, the performance of the filter was also investigated under conditions of irregular spatial sampling and noise. Synthetic data was reacquired on the same earth model depicted in Figure 42. However, this time, the inter-receiver distance follows a normal distribution with

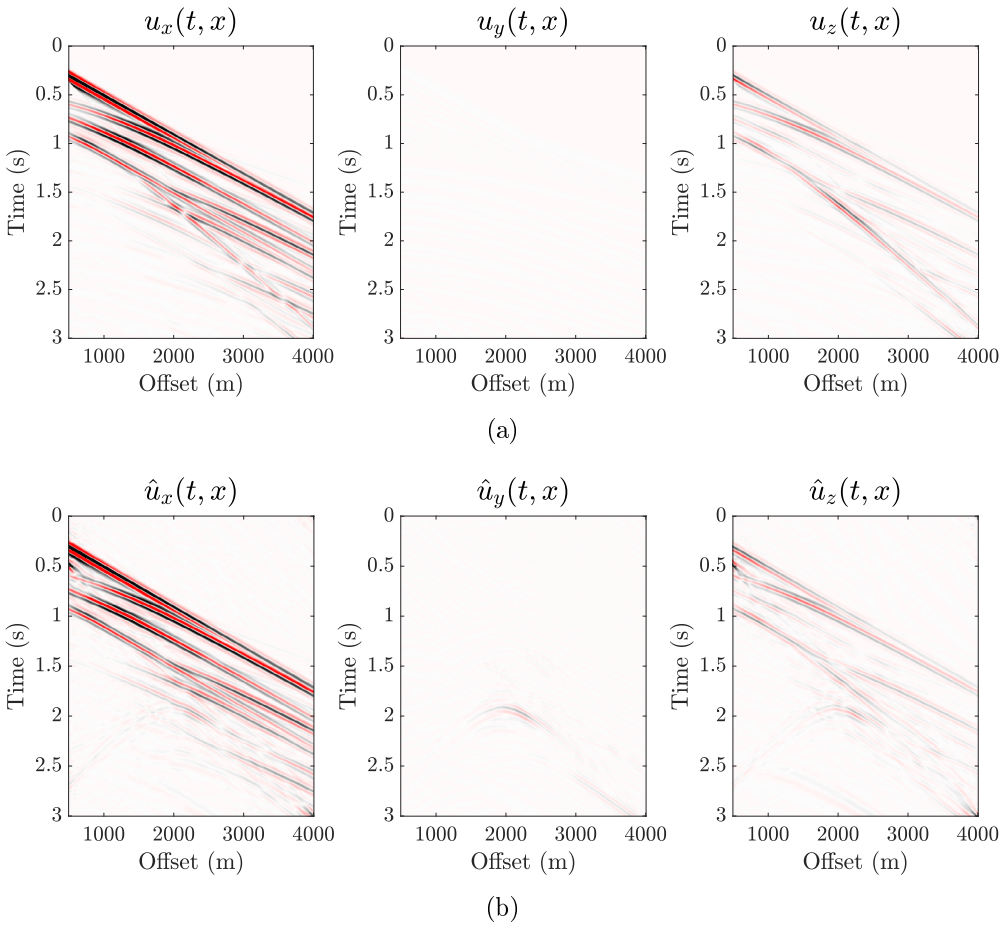

Figure 48. Extraction of body waves from modeled data. (a) True modeled body waves. (b) Resulting body waves reflections and direct wave obtained by subtracting the predicted Rayleigh wave (Figure 46(b)) and the near-surface scattered waves (Figure 47(b)) from the total modeled data in Figure 43.

Table 11
Prediction gains obtained after extraction of polarized wavefields using 3C-FSPF in example 2. Prediction gain G_y cannot be computed for the Rayleigh wave and the body wave since the energy of the reference true wavefield in the y-component is zero.

Wave type	G_x (dB)	G_y (dB)	G_z (dB)
Rayleigh wave	24.33	-	24.34
Near-surface scattering	1.19	3.02	1.43
Body waves	16.54	-	5.06

a mean of 10 m and a standard deviation of 3 m. Subsequently, the traces were decimated at percentages ranging from 0 % to 80 %. Lastly, varying levels of random noise were introduced to the data, with SNR values of 1.0, 0.9, 0.8, and 0.5. As shown in Figure 49, the prediction gains across all components begin to deteriorate as the percentage of decimation increases and the signal-to-noise ratio (SNR) decreases. This trend indicates that the effectiveness of the 3C-FSPF in predicting different wave types may be compromised under conditions of high data decimation and low SNR. However, even under these challenging conditions, the filter still offers certain advantages and may outperform traditional methods.

Figure 50 illustrates a shot gather example of wave type separation using the 3C-FSPF filter. In this shot gather, the data have an SNR of 0.8 and 50 % trace decimation. It is observed that the filter is capable of accurately predicting the different wave types presented in the shot gather, thereby validating its effectiveness under these conditions.

4.8. Example 3: Ground roll attenuation in a real 3C shot gather.

In this third example, the proposed polarization method was tested using a real 3C shot gather from seismic data acquired in the Middle Magdalena Valley in Colombia. The shot gather for the vertical, radial, and transverse components after a gain correction of t^2 is displayed in Figure 51. It is observed that the ground roll appears more complex for short offset than long offset. We interpret this as a result of the low-velocity and heterogeneous near-surface close to the source location, which produces back-scattering and reverberations that mask the body wave reflections from deeper structures.

To compute the Radon transform for each single component, we used $p_0 = -10 \times 10^{-3}$

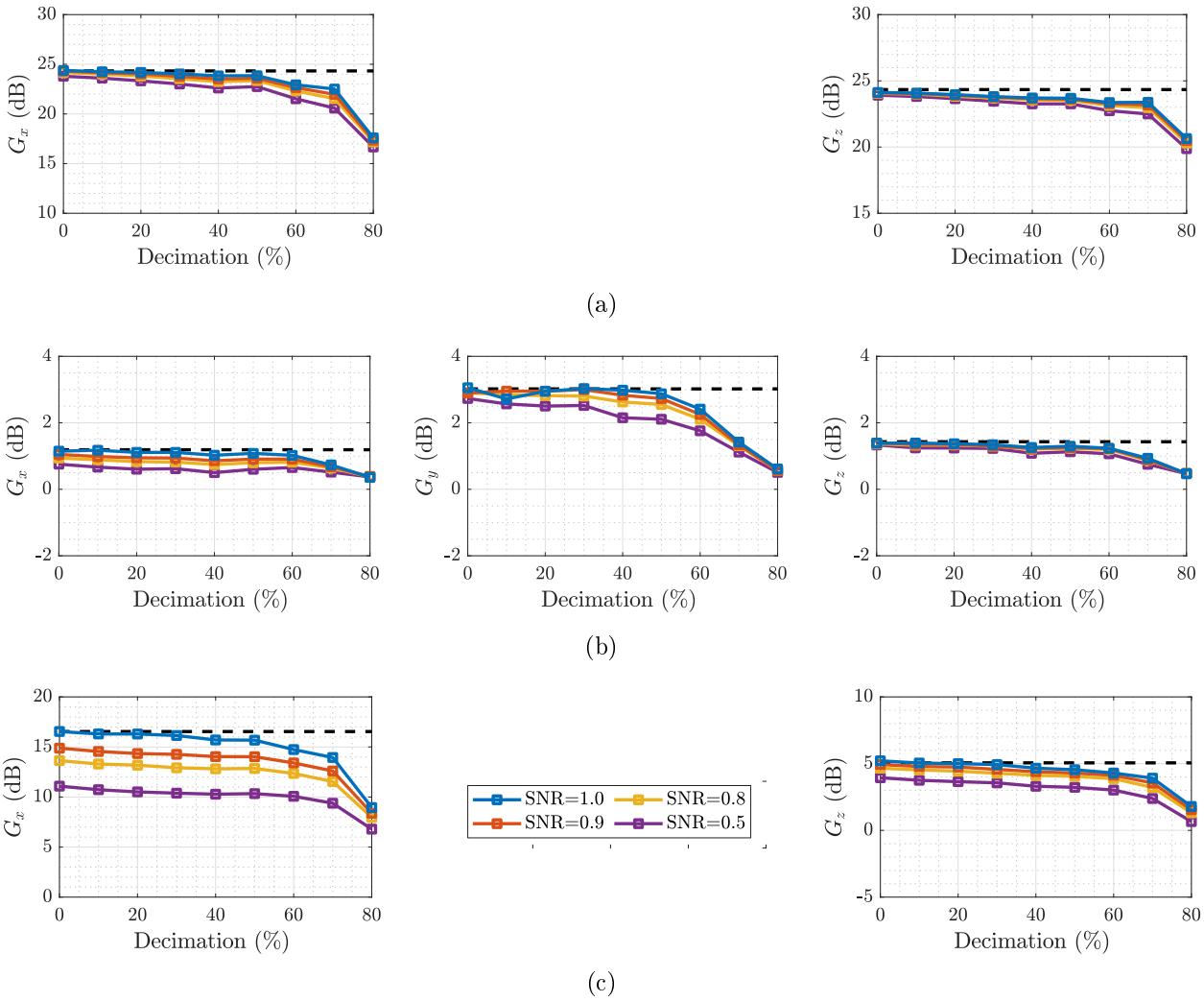

Figure 49. Prediction gains for reconstruction of (a) Rayleigh wave, (b) body waves (including direct wave, reflections and refractions), (c) near-surface scattering. In this example, the inter-receiver distance follows a normal distribution with a mean of 10 m and a standard deviation of 3 m. Gains G_x, G_y, and G_z were calculated under varying percentages of trace decimation and different Signal-to-Noise Ratio (SNR) levels. The dashed black line indicates to the prediction gain from data with regular sampling and without noise influence. For (a) and (c), the absence of G_y results is due to the impossibility of calculating equation 98 because there is no energy of u_y in the true modeled Rayleigh wave, as illustrated in Figure 46(a).

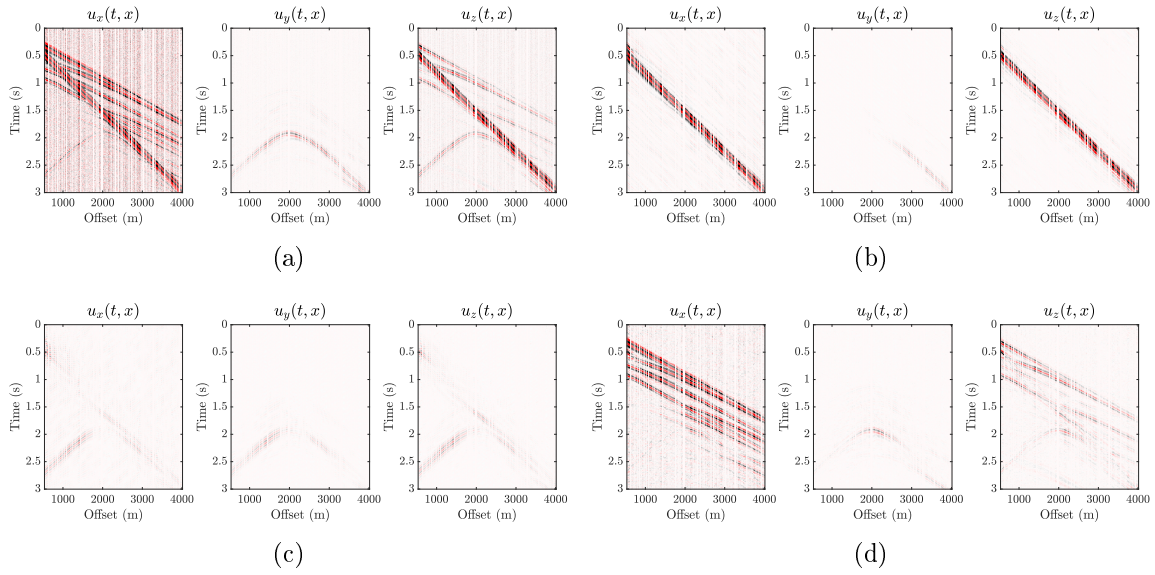

Figure 50. Example of wave types extraction from modeled data irregularly sampled. (a) Modeled data with SNR=0.8 and 50 % trace decimation. (b) Extracted Rayleigh waves. (c) Extracted near-surface scattered wave. (d) Extracted body waves (including direct wave, reflections and refractions.

(s/m), $\Delta p = 1.6 \times 10^{-5}$ (s/m), and $N_p = 1251$ samples.

Figure 52 shows the $f-p$ spectra of each elliptical element obtained from the HRLRT for each component of the real data. the HRLRT was computed with $p_0 = -10 \times 10^{-3}$ (s/m), $\Delta p = 1.6 \times 10^{-5}$ (s/m), and $N_p = 1251$ samples.

In Figure 52(a), which corresponds to the semi-major $a(f,p)$, and Figure 52(b), which corresponds to the semi-minor axis $b(f,p)$, we can identify the fundamental mode of the Rayleigh wave around $p = 0.005$ (s/m). Higher modes of Rayleigh waves are present even since approximately $p = 0.001$ (s/m). We also observe that most of the Radon model energy is scattered and bounded below 15 Hz. Additionally, the information in the negative values of p corresponds to linear events of the shot gather with negative slopes, which can be related

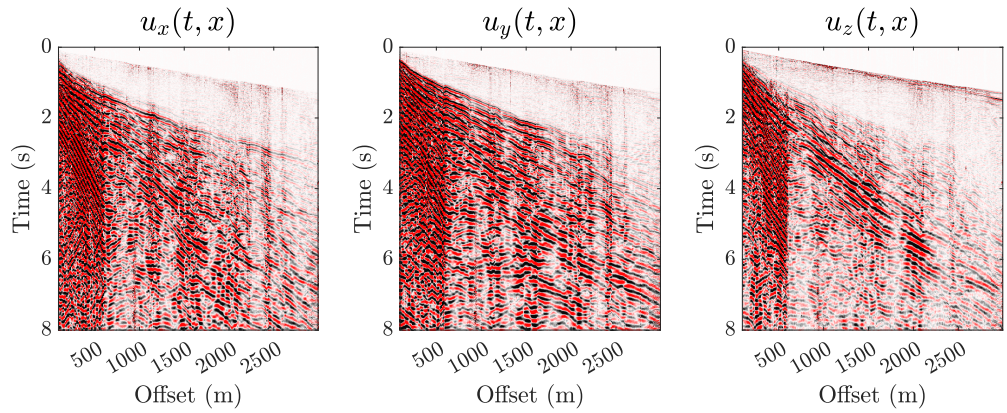

Figure 51. 2D-3C shot gather of real data acquired in the Middle Magdalena Valley, Colombia, after a t^2 gain correction.

to back-scattered waves.

To eliminate the ground roll from the seismic data, we designed a series of 3C-FSPFs, each specially configured to extract different wave types that constitute the ground roll. In this particular case, we identified three different wave types: the Rayleigh wave, scattered Rayleigh wave, and scattered body waves. The parameters for each filter were manually adjusted for each wave type, as detailed in Table 12. In this real data scenario, we refrained from using the incidence angle I due to unstable values resulting from interference from multiple wave types, as illustrated in Figure 52(c). Additionally, each filter mask was formulated to operate within a specific region in the (f, p) domain, constrained by the conditions $f_{\min} \leq f \leq f_{\max}$ and $1/v_{\max} \leq p \leq 1/v_{\min}$. These constraints ensure the targeted extraction of specific wave types, allowing for a more accurate ground roll elimination.

The filter masks for each wave type are displayed in Figure 53.

The resulting shot gathers after applying the 3C-FSPF to each type are shown in

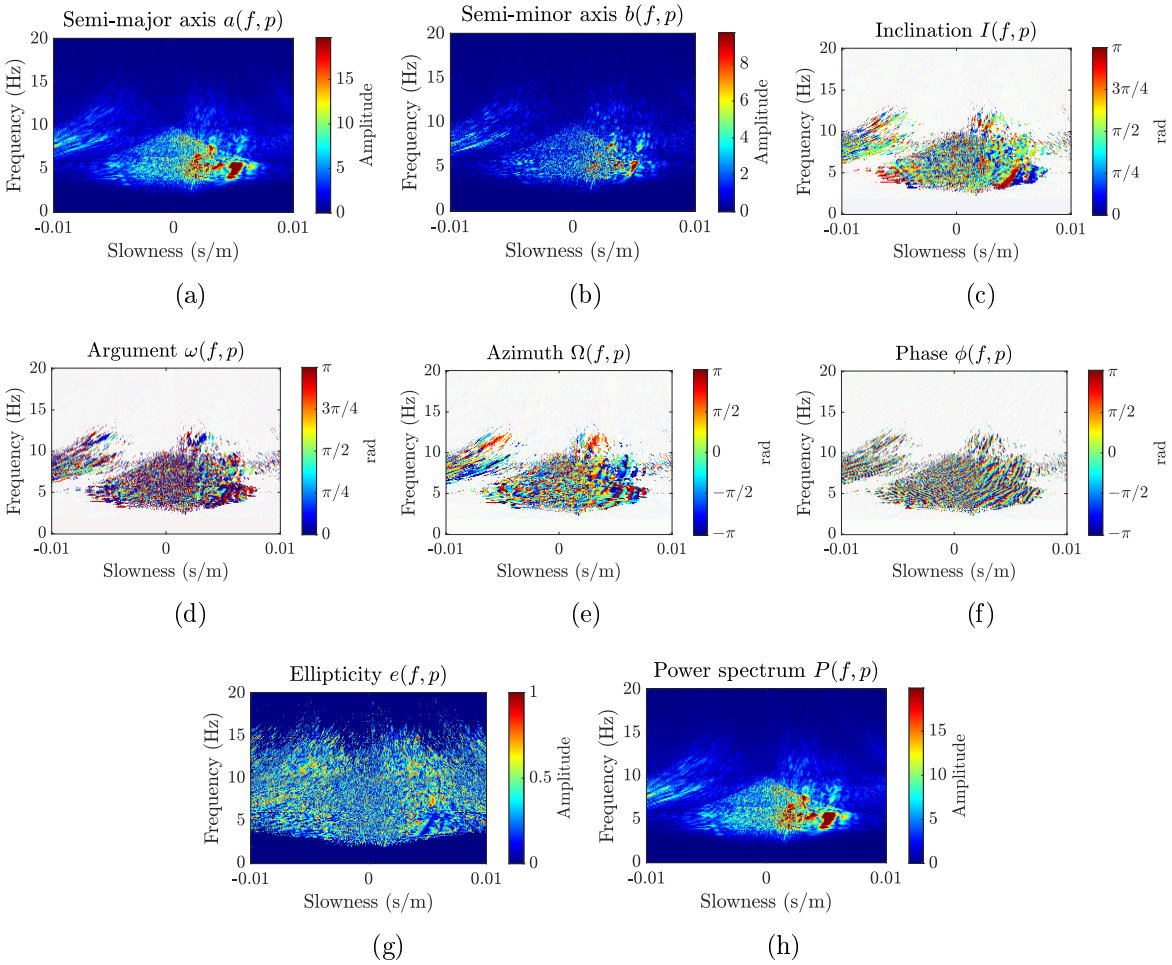

Figure 52. Spectra of elliptical elements in the (f,p) domain, derived via HRLRT from the real data in Figure 51: (a) Semi-major axis a, (b) semi-minor axis b, (c) inclination I, (d) argument of pericentre ω, (e) azimuth of ascending node Ω, (f) phase ϕ, (g) ellipticity e, and (h) power spectrum P.

Figure 54. By subtracting the predicted wave types from the raw data, we were able to obtain filtered data without ground roll.

In this real data example, we compared the performance of the 3C-FSPF in suppressing ground roll with the traditional velocity $f-k$ filter presented in Appendix B. This filter contains four parameters (v_1, v_2, v_3, and v_4) that specify the attenuation range. The

Table 12
Filter parameters of 3C-FSPF to separate the wave types from the 3C real data in Figure 51. For each wave type, the filter mask operates inside the region in the (f, p) domain limited by $f_{min} \leq f \leq f_{max}$ and $1/v_{max} \leq p \leq 1/v_{min}$.

Wave type	Filter mask	e_1	e_2	Ω_c	Ω_1	Ω_2	$f_{\min}$	$f_{\max}$	$v_{\min}$	$v_{\max}$
Rayleigh	$F_e F_\Omega$	0.2	0.3	0	$\pi/4$	$\pi/2$	2	15	100	1200
Scattered Rayleigh	$F_e(1 - F_\Omega)$	0.2	0.3	0	$\pi/4$	$\pi/2$	2	15	100	1200
Scattered body	$(1 - F_e)(1 - F_\Omega)$	0.2	0.3	0	$\pi/4$	$\pi/2$	2	15	100	800

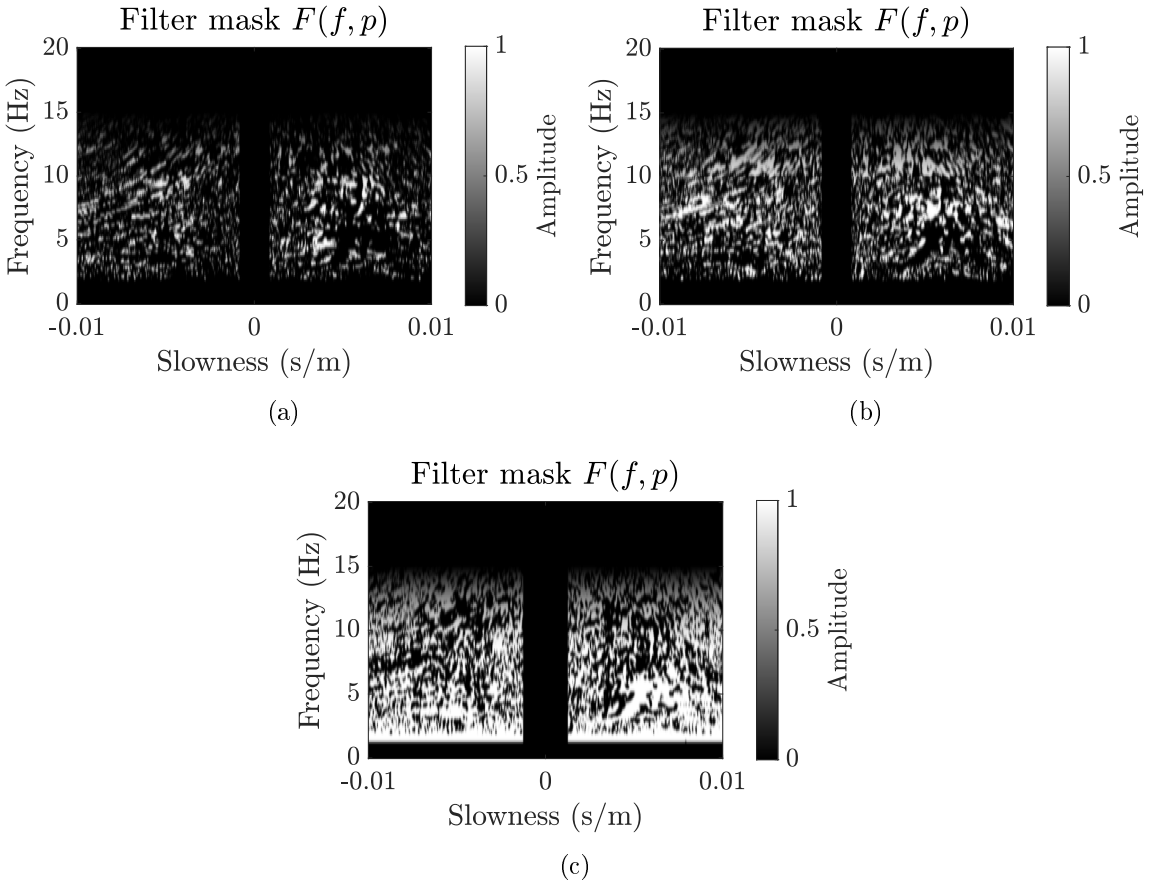

Figure 53. Filter masks used to separate the wave types that constitute the ground roll from the real 3C data in Figure 51. These include: (a) mask for Rayleigh wave extraction, (b) mask for scattered Rayleigh wave extraction, and (c) mask for scattered body wave extraction. Corresponding parameters for each filter mask are detailed in Table 12.

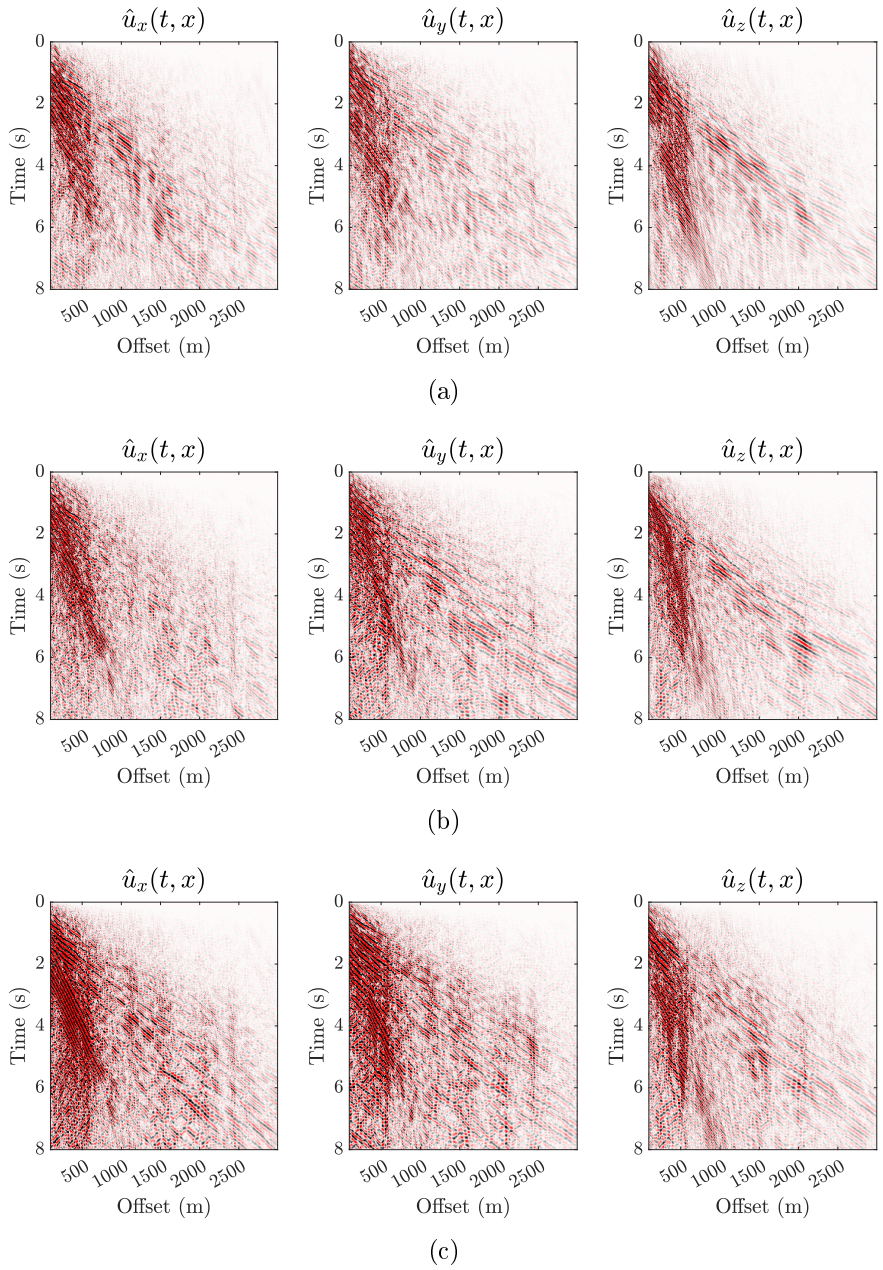

Figure 54. Separation of the types of waves that constitute the ground roll from the real 3C data in Figure 51 by using 3C-FSPF. (a) Rayleigh waves. (b) Scattered Rayleigh waves. (c) Scattered body-waves.

range between v_2 and v_3 is rejected, and the range below v_1 or above v_4 is preserved. In this example qe set the velocities $v_1 = 350$ (m/s), $v_2 = 450$ (m/s), $v_3 = 750$ (m/s), and $v_4 = 1000$

(m/s). Multicomponent shot gathers after $f-k$ filtering and 3C-FSPF are presented in Figure 55(a) and 55(b), respectively. While minor differences were observed between the resulting shot gathers from the $f-k$ filter and the 3C-FSPF, a more comprehensive comparison was carried out by analyzing the Fourier spectra of the filtered data to evaluate the influence of each filter in the frequency domain. The spectra for the vertical, radial, and transverse components are displayed in Figure 56.

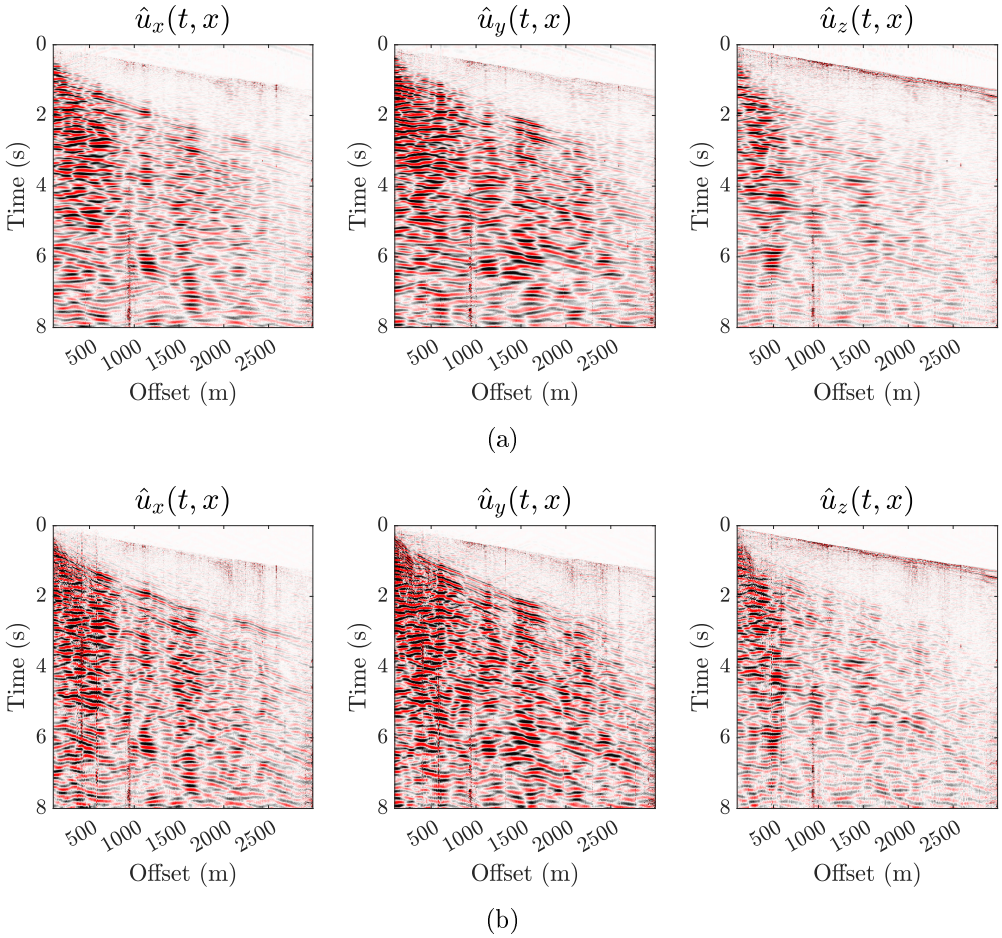

Figure 55. Ground roll attenuation of the 3C real data by using (a) FK filter and (b) 3C-FSPF. Result in (b) is obtained by subtracting the wavefields in Figure 54 from the total data in Figure 51.

It was observed that the 3C-FSPF preserved slightly more low-frequency energy (below 10 Hz) than the $f-k$ filter. This energy is associated with low-frequency reflections, as the polarization filter is designed to retain linear polarization and attenuate elliptical polarization motions. In the mid-frequency band, 10 Hz and 15 Hz, the 3C-FSPF appeared less aggressive than the $f-k$ filter, attenuating up to 5 dB less. This suggests that in this frequency band, the 3C-FSPF preserves certain body waves that are otherwise attenuated by the $f-k$ filter due to their approach along the source-receiver plane. Lastly, in the high frequency region, the 3C-FSPF maintains all the energy of the raw data as the filter masks were intentionally designed not to operate at frequencies higher than 15 Hz (see Table 12).

Finally, the performance of the 3C-FSPF is evaluated in the case of missing traces in the real data example. Prediction gains are computed with trace decimation percentages ranging between 10 % and 80 %, using the full receiver results as the reference wavefield. As depicted in Figure 57, it can be observed that the prediction gain decreases for all components as the percentage of trace decimation increases. This trend, again, indicates that the performance of the 3C-FSPF is sensitive to the availability of trace data, and it may not perform as effectively in cases of high trace decimation.

Figure 58 illustrates the result obtained with the real data example with 50 % trace decimation. here, it is observed that the 3C-FSPF can still predict the ground roll, even with a significant percentage of missing traces. This example underscores that even under such challenging conditions, the 3C-FSPF can be a valuable tool when dealing with poorly spatially sampled seismic data.

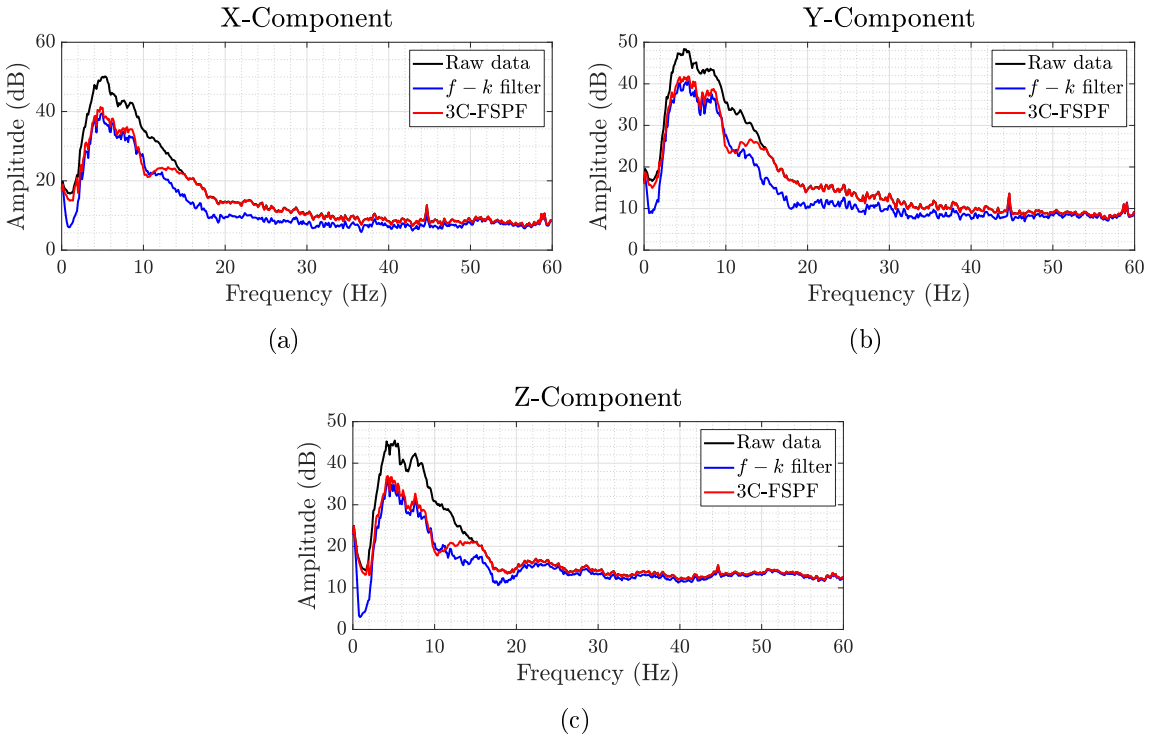

Figure 56. Separation of the types of waves that constitute the ground roll from the real 3C data in Figure 51 by using 3C-FSPF. (a) Rayleigh waves. (b) Scattered Rayleigh waves. (c) Scattered body-waves.

4.9. Discussion

The proposed 3C-FSPF is an efficient technique for discriminating types of waves with different polarization in the (f, p) domain. In this study, it was demonstrated that the 3C-FSPF can accurately separate the types of waves that compose ground roll, such as Rayleigh waves, near-surface scattered waves, and low-velocity body waves such as near-surface reflections and refractions.

One of the significant contributions of this study is the formulation of the 3C-FSPF through a combination of tailored activation functions for ellipticity, azimuth angle, and

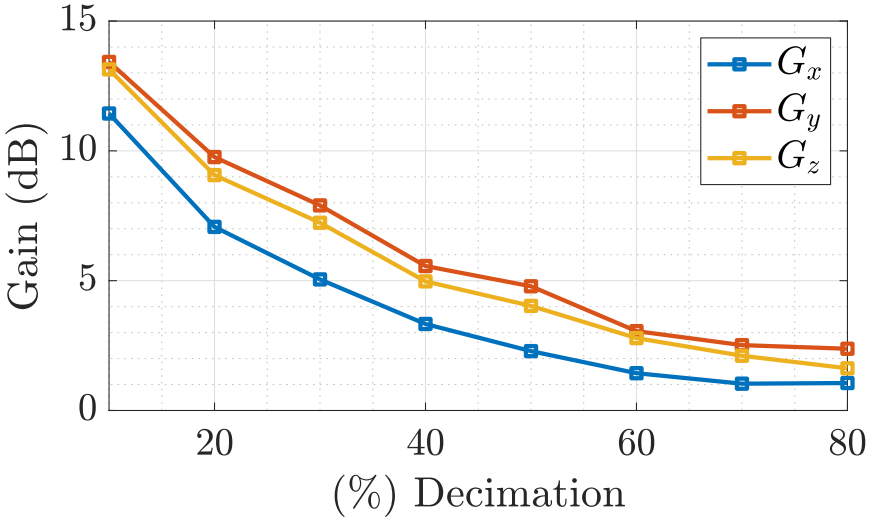

Figure 57. Prediction gains for reconstructed real data without ground roll under different levels of decimation of traces.

inclination angle. This contrasts with the fixed-parameter functions presented by Pinnegar (2006), which primarily attenuate the Rayleigh wave. The variable-parameter activation functions extend the scope of the 3C-FSPF, enabling the extraction of not just Rayleigh waves but also other wave types, thereby enhancing the adaptability and utility of this method. For instance, in Example 1, the 3C-FSPF was designed to specifically extract the elliptically polarized wave type, retaining the information with ellipticity higher than 0.3 (see Figure 39(a)). Similarly, in Example 2, the method was adapted to extract near-surface scattered waves by discarding the energy in the (f, p) domain where the azimuth was nearing zero (see Figure 47(b)).

The main advantage of the 3C-FSPF is its capacity to simultaneously process all traces within a shot gather. This represents a clear advancement over single-station methods, which are constrained by their inability to utilize velocity information for wave type discri-

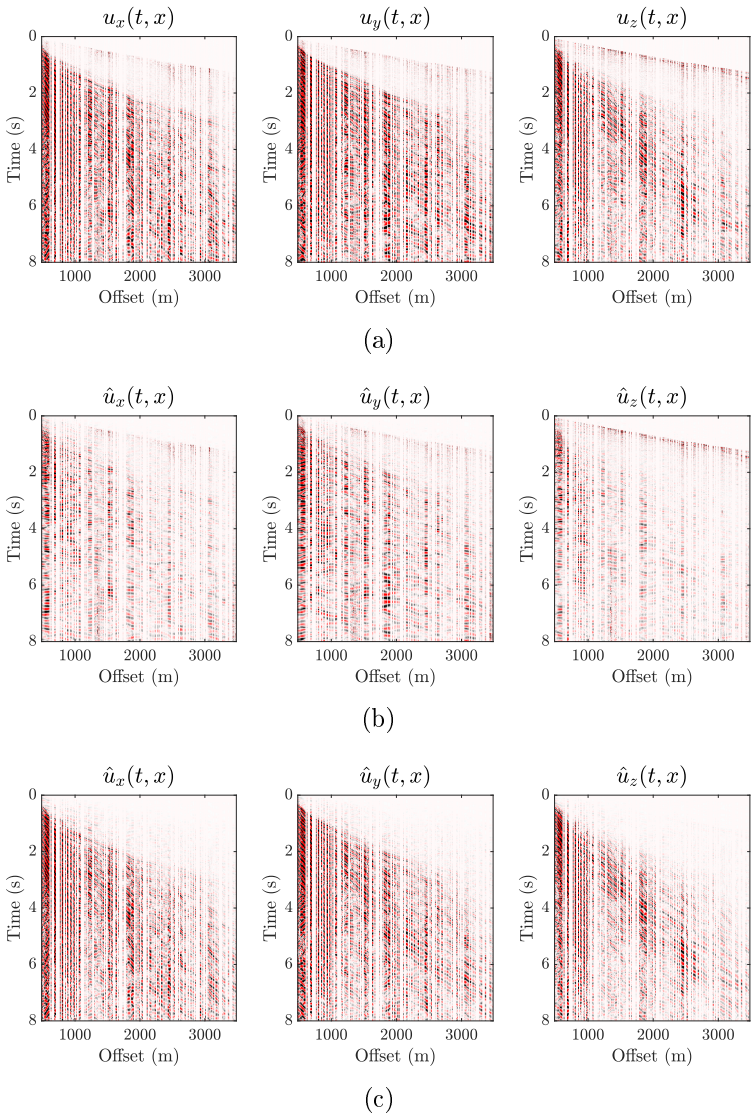

Figure 58. Ground roll attenuation on a multicomponent shot gather with missing traces. (a) Real data (shown in Figure 51) after 50 % decimation of traces. (b) Resulting shot gather after ground roll attenuation by 3C-FSPF. (c) The difference between (a) and (b).

mination. Furthermore, the 3C-FSPF can efficiently handle data with irregular and sparse spatial sampling, unlike multi-station techniques that necessitate regularly spaced data. This advantage is particularly relevant in areas with complex near-surface structures where traditional filters may not be able to effectively discriminate between different wave types. Results

from real data demonstrate the ability of the 3C-FSPF to successfully separate different types of waves in the ground roll, as depicted in Figure 54. Comparisons with the traditional $f-k$ filter reveal that the 3C-FSPF provides greater discrimination power, preserving more energy after filtering (Figure 56). Moreover, the 3C-FSPF is applicable even under conditions of poor spatial sampling, highlighting its robustness and versatility in enhancing the quality of seismic imaging in areas with complex near-surface structures.

One promising direction for future research involves the utilization of reconstruction algorithms on post-filtered traces. Traditional approaches usually attempt to reconstruct missing traces based on existing ones without prior filtering, which places a considerable demand on the reconstruction algorithm. This is due to the necessity of predicting all wave types present within the seismic data. However, with the introduction of 3C-FSPF, sparse traces can be processed prior to the application of the reconstruction algorithm. This preprocessing step has the potential to improve the accuracy of the reconstruction as it allows for the prediction of specific wave types. Therefore, employing 3C-FSPF in conjunction with reconstruction algorithms could yield more reliable and accurate seismic data, even in situations with substantial missing or irregularly sampled information.

Despite these notable advantages, further research is necessary to fully explore the capabilities and limitations of the 3C-FSPF. Its performance may vary depending on factors such as the geological setting, acquisition geometry, and the quality of seismic data. Additional studies are needed to validate the effectiveness of the 3C-FSPF across different areas and to optimize its parameters for specific applications. For future research, it is suggested

to implement a machine learning workflow to design 3C-FSPF masks, using (f, p) domain panels of elliptical elements as inputs. This approach could potentially enhance the method's adaptability to various data types, reducing the time spent fine-tuning filter parameters and improving the total efficiency of the process. Overall, the 3C-FSPF represents a significant advancement in the field of seismic imaging, promising to improve the performance of of multicomponent data filtering.

4.10. Conclusions

A novel two-step polarization method has been introduced in this chapter, with the main objective of discriminating and separating wave-types in under-sampled 3C seismic data. This approach was devised to overcome the limitations of single-station filters, which are unable to utilize velocity information for wave-type discrimination, and multi-station approaches that necessitate regularly spatially sampled data. The initial phase of the proposed method involves the polarization analysis of the 3C shot gather. This is achieved by computing elliptical elements in the frequency-slowness (f, p) domain using the HRLRT applied to each individual component. Subsequently, the second phase employs the 3C-FSPF to isolate distinct polarized waves. This is executed by constructing a filter mask within the (f, p) domain using activation functions, the parameters of which are determined by the polarization analysis. The effectiveness of the method was validated through results obtained from both synthetic and real data, demonstrating its capability in extracting polarized wave types. Furthermore, tests conducted under conditions of irregular and sparse spatial sampling along with noise underscored the method's potential for enhancing the quality of seismic data, par-

ticularly those acquired in complex land regions such as foothills. Therefore, this innovative method opens a new approach in improving seismic data analysis and interpretation, even under challenging conditions. For future research, it is proposed to broaden the application of this method across diverse geological contexts. Additionally, integrating machine learning algorithms could enhance the design of the mask filter, enabling an adaptive, data-driven approach.

CHAPTER 5. Attenuation of near-surface seismic scattering with autoencoders

5.1. Abstract

The 3C-FSPF polarization filter introduced in Chapter 4 can separate polarized wave events in 3C seismic data. The filter leverages variable-parameter activation functions, which require careful tuning to create a mask that extracts specific polarized energy. However, this tuning process must be performed manually for each wave type and dataset independently, making the process tedious and susceptible to human bias. To address this, two Machine Learning (ML) workflows are proposed to train neural network models that can identify NSS patterns and effectively attenuate them. The first ML workflow uses the Partitioned Domain Method (PDM), detailed in Chapter 3, to generate 3C seismic data with and without Near-surface Seismic Scattering (NSS). These data, processed with the polarization analysis method presented in Chapter 4, serve as inputs and labels to train a UNET autoencoder that predicts the filter mask in the (f, p) domain. The second machine learning workflow extends the first by including an additional UNET autoencoder that refines the filtered 3C seismic data in the (t, h) domain. The ML workflows were tested using synthetic datasets generated with the SEAM Foothills Phase II model and the finite-difference method solver (PMFD3D-GPU) described in Chapter 2. The results demonstrate that the trained autoencoders can significantly reduce NSS noise, thereby enhancing the quality of deeper reflections in 3C seismic data. Future work should focus on testing the trained autoencoders with real data and incorporating a more varied range of training datasets to mitigate model overfitting.

5.2. Introduction

Filtering in signal processing is a critical operation due to its ability to enhance signal quality, separate distinct signals, and attenuate noise. Real-world signals often contain unwanted noise or interference, and filters can efficiently minimize these distortions, ensuring the signal's information is correctly interpreted. In the context of seismic exploration, filtering can help separate different wave type components of the seismic signals, which can correspond to different depths or types of geological formations. One such type of signal is the Near-Surface Seismic Scattering (NSS), which provides information about near-surface structures. While NSS can be valuable in some contexts, for seismic imaging, the primary interest lies in detecting body-wave reflections from deeper structures that can provide insights about subsurface geology and potential hydrocarbon reservoirs. Unfortunately, these deeper signals are often masked by the NSS noise.

In Chapter 4, a polarization filter (3C-FSPF) was introduced to separate Near-Surface Scattering (NSS) in 3C seismic data. While the filter was able to achieve excellent results on various examples with synthetic and real data, the process of manually tuning the parameters proved to be a demanding task. This process can be laborious and time-consuming as it often necessitates iterative trial-and-error adjustments. Moreover, this task demands a high degree of expertise and understanding of both the filtering technique and the nature of the seismic data to make appropriate decisions on parameter settings. It also introduces a degree of subjectivity into the process, as different operators might choose different parameters for the

same data, potentially leading to inconsistent results. Furthermore, manual tuning does not always scale well with large datasets, and it might not account effectively for variability in seismic signals across different regions or depths, leading to suboptimal filtering outcomes.

Machine learning emerges as a powerful solution to address these challenges associated with manual tuning in seismic signal processing. Machine learning models can learn from large volumes of data, identifying patterns that may not be easily discernible to human operators. Once trained, these models can automatically adjust filter parameters to eliminate the need for labor-intensive manual tuning. This also removes the subjectivity involved in manual tuning, which leads to more consistent and repeatable results. Moreover, machine learning can handle the complexity and variability in seismic data more effectively as these models can be trained on diverse datasets with different geological conditions. Their ability to learn and generalize from training data means they can adapt to new data potentially providing robust performance even when the seismic signals are unfamiliar or change over time.

Over the past decade, the use of machine learning algorithms in geophysical applications has rapidly increased. These algorithms can automatically find patterns within example datasets. They are numerous applications in geophysics, including seismic facies classification (Zhao et al. 2015; Wrona et al. 2018; Puzyrev and Elders 2022), fault detection (Wu et al. 2019; Wang et al. 2020b; An et al. 2021), geophysical inversion (Zheng et al. 2019; Russell 2019; Chen and Schuster 2020), first arrival picking (Hu et al. 2019; Tsai et al. 2019), and seismic trace interpolation (Mandelli et al. 2018; Wang et al. 2020a), among others.

In this work, two machine learning workflows are proposed to attenuate Near-Surface Scattering (NSS) in 3C seismic data. The first workflow uses a U-net autoencoder to predict a filter mask in the (f, p) domain, which is used to clean the seismic data by removing most of the NSS noise. The second workflow aims to refine the filtered data with first machine learning workflow, using an additional U-net autoencoder operating in the (t, h) domain to highlight the signal of interest. The machine learning workflows were trained on synthetic datasets obtained through elastic wave modeling in the SEAM Foothills Phase II model using the PMFD3D-GPU solver. The results over these datasets reveal that the autoencoders can learn to identify NSS patterns to attenuate them effectively.

5.3. UNET autoencoder

U-net stands as an influential innovation in the field of image segmentation. This architecture represents a specific kind of Convolutional Neural Networks (CNNs), a subset of Artificial Neural Networks (ANNs) mainly utilized in image and video processing applications. CNNs can create feature maps from the input image using convolutional kernels. These feature maps are then subjected to pooling to decrease their dimensions, yielding compact representations that feed into a fully connected ANN. This allows CNNs to extract and select representative features directly from raw images.

One notable form of CNNs is the Convolutional Autoencoder, which excels at learning dense representations of input data (Géron, 2022). These autoencoders are split into two components: an encoder and a decoder. The encoder uses convolutional and pooling layers to convert the input data into a smaller, latent representation. The decoder, on the other hand,

recreates an output from this representation, which closely resembles the input data.This process enables the autoencoder to determine an internal representation that includes the most significant features of the input data.

U-net, as a specific form of Convolutional Autoencoder, was initially designed for biomedical segmentation applications (Ronneberger et al., 2015). It differentiates itself through its unique approach in the decoder part. After upsampling layers, feature maps created by the encoder are integrated, allowing for the propagation of contextual information to higher-resolution layers. Additionally, before data is input into the network, a tiling strategy is applied. This strategy enables the training of large images by creating patches of smaller dimensions. As a result, UNET can provide precise segmentation with a limited number of training images, as the number of patches significantly outnumbers the number of training images.

In this study, the U-net architecture is utilized to detect Near-Surface Scattering (NSS) patterns in both the (f, p) and (t, h) domains. The architecture implemented in this study is depicted in Figure 59. The input must be a $64 \times 64 \times N_c$ 3D data array, where N_c is the number of channels. The data cube is encoded in four levels, which include five 3×3 convolutional layers and four 2×2 max-pooling layers. The latent representation is decoded by five 3×3 convolutional layers and four 2×2 up-pooling layers. In the decoding process, the output of each decoding level is duplicated and cropped at each level of decoding. The resultant image is passed through a 1×1 convolutional layer with a tanh activation function.

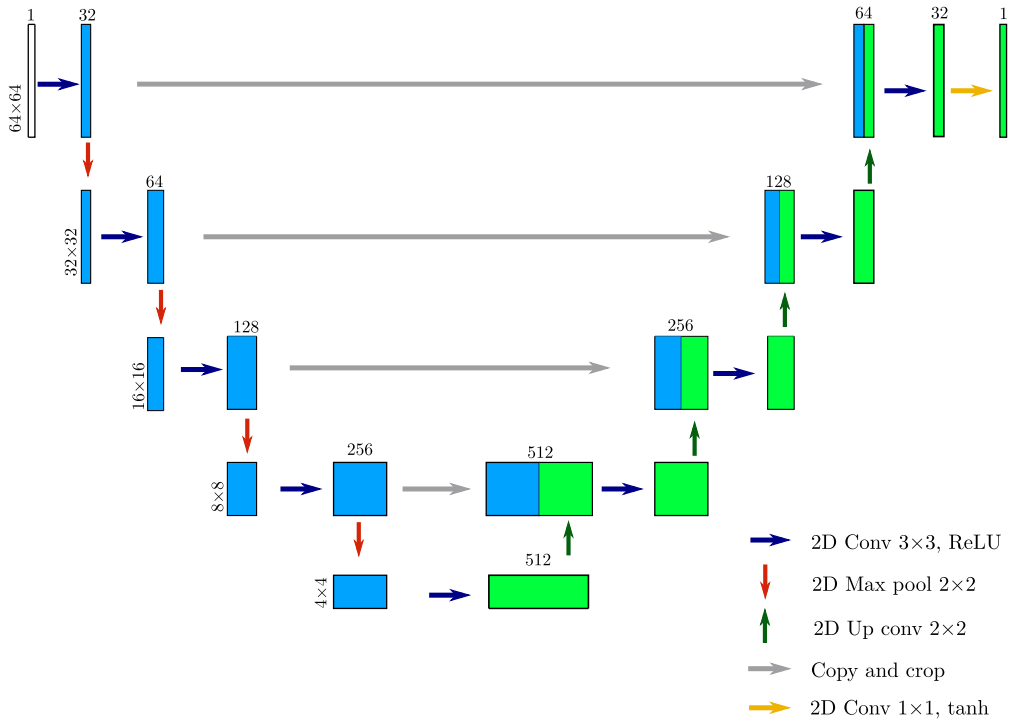

Figure 59. Implementation of a UNET architecture for NSS attenuation. The architecture utilizes four coding levels to derive a latent representation of a $64 \times 64 \times N_c$ 3D data array. N_c denotes the number of channels.

5.3.1. Image patching. To comply with the 64×64 size requirement, seismic data need to be split into smaller segments or patches. This image patching approach offers several computational advantages. Firstly, it ensures efficient memory usage, as instead of storing the whole image in memory, only the current patch is stored (Sharif Razavian et al., 2014). Secondly, it can drastically decrease the computation time for training. Training on patches is faster because it diminishes the number of parameters in the network and simplifies the complexity of the optimization (Alzubaidi et al., 2021).

As discussed in section 4.3, the shot gather dimensions in the (t, h) domain are $(N_t \times N_h)$, and in the (f, p) domain, they are $(N_f \times N_p)$. In this study, overlapping patching is

applied to create (64×64) patches with 50 % overlap (i.e., 32 points). All processing is performed on patches, so an image reconstruction is needed to assemble the patches back together in their original order to recreate the image in its original dimension. When the data dimension is not a multiple of 64, a mirror padding technique is used to extend the data by creating a mirrored or reflected version of the data at its boundaries, maintaining the continuity of features at the edges of the data.

5.4. Label generation

Labels play a crucial role in training neural networks as they serve as a form of ground truth that the network can learn from. In supervised learning, the most common training approach for neural networks, the network is given input data along with corresponding labels. These labels represent the desired results that the neural network needs to learn and predict accurately.

In this study, the main objective is to predict 3C seismic data without Near-Surface Scattering (NSS). However, performing this task directly in the (t, h) domain may produce unsatisfactory results since the higher amplitudes of NSS noise can often mask the weak body-wave reflections. Therefore, the transformed (f, p) domain is utilized for processing, utilizing the spectra elliptical elements as discussed in section 4.4 to create labels of the filter mask in the (f, p) domain. The label $P_L(f, p)$ is generated using the power spectrum attribute and is defined as follows:

$$P_L(f,p) = \begin{cases} \dfrac{P_{DW}(f,p)}{P_{TW}(f,p)} & \text{if } P_{TW}(f,p) > \epsilon \\ 0 & \text{otherwise} \end{cases}. \tag{99}$$

Here, P_{TW} and P_{DW} denote the power spectra for the total and deep wavefields, respectively, calculated using the PDM presented in chapter 3. The value ϵ is a small positive constant introduced to avoid division by zero.

The label calculated with equation (99) produces a filter mask. The values within this mask are lower in regions with presence of NSS and higher in regions where NSS is absent.

5.5. Machine Learning workflows

5.5.1. ML workflow in the frequency-slowness domain. The primary aim of this machine learning (ML) workflow is to predict a filter mask that can attenuate NSS in the (f,p) domain. The training phase of this workflow comprises four key steps, as shown in Figure 60(a). The first step involves computing synthetic data both with and without NSS by applying the PDM, which generates the total and deep wavefields. These data undergo a polarization analysis to derive the spectra of elliptical elements in the (f,p) domain. These elements serve as inputs and attributes to generate labels for training the UNET model architecture. Label generation utilizes equation (99), while inputs consist of the (f,p) panels of semi-major axis a, semi-minor axis b, and azimuth of the ascending node Ω. These elements were chosen due to their superior performance, as reported in Chapter 4. The UNET architecture, depicted in Figure 59, is then employed to predict the filter mask

in the (f, p) domain.

The testing phase of the ML workflow consists of three steps, as illustrated in Figure 60(b). The input is 3C seismic data, which is processed by polarization analysis to compute the spectra of elliptical elements. The elements (a, b, Ω) are subsequently fed into the trained UNET model, which predicts the filter mask. This mask is then used to attenuate the NSS noise, yielding filtered 3C data. In this final phase, it is necessary to apply steps 4 and 5 of the procedure outlined in section 4.5.1 for polarization filtering.

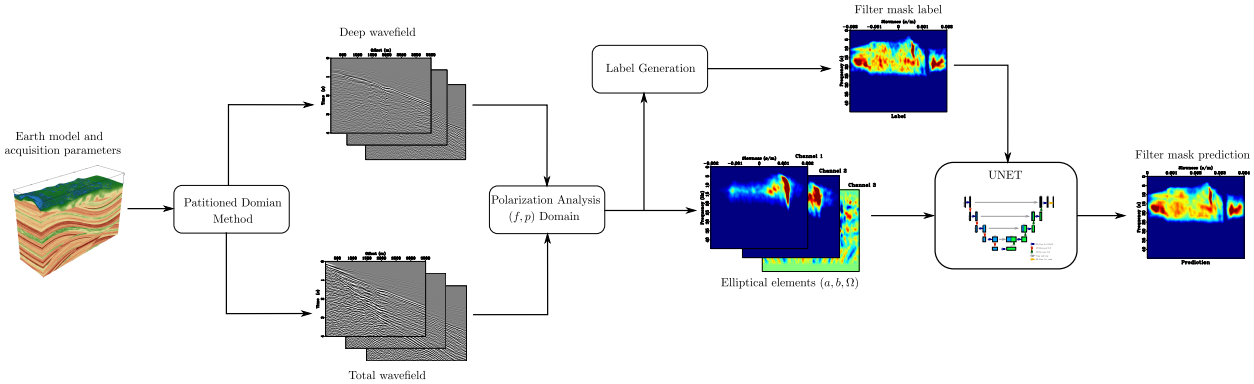

(a)

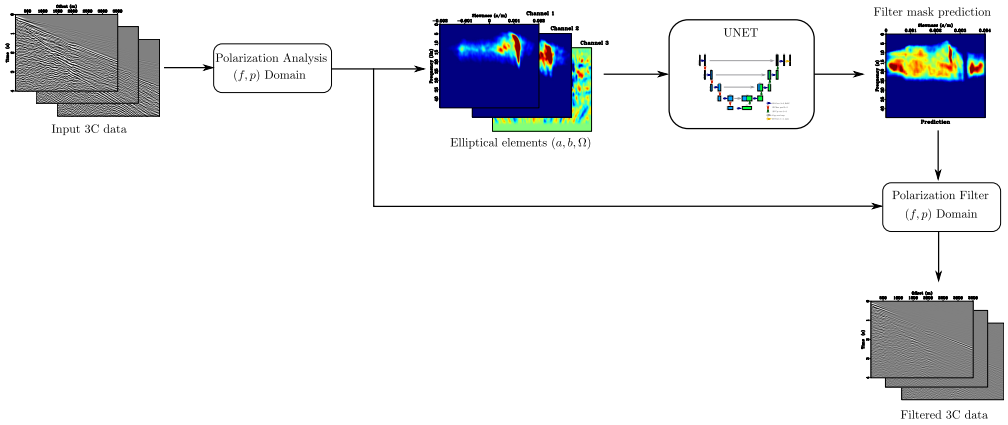

(b)

Figure 60. ML workflow for NSS attenuation. (a) ML training workflow designed to predict the 3C filter mask in the (f, p) domain. (b) ML testing and filtering workflow

5.5.2. Nested ML workflow. A nested ML workflow is proposed to enhance the results obtained from filtering in the (f, p) domain. This refined workflow, as depicted in Figure 61, combines the previously discussed ML workflow with an additional UNET auto-encoder. The 3C data filtered by the initial workflow is refined by using the total wavefield as a second channel input and the deep wavefield as label. This new step is performed in the (t, h) domain to highligh the body-waves reflections that may be attenuated by the filtering in the (f, p) domain. This nested ML workflow is devised with the aim to enhance the quality of the final output data.

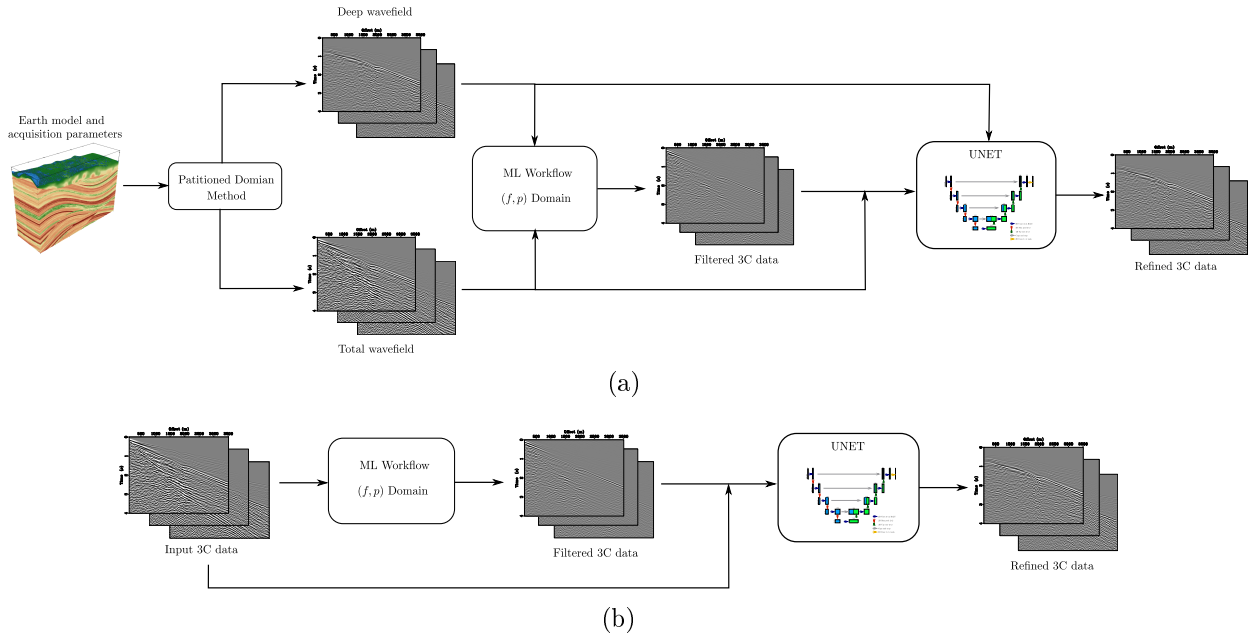

Figure 61. Two-stage nested ML workflow for NSS attenuation. The first stage applies the ML workflow from Figure 60 to filter the 3C data in the (f, p) domain. Subsequently, a UNET refines the filtered data in the (t, h) domain. (a) Training nested ML workflow. (b) Testing nested ML workflow.

5.6. Numerical Test

The proposed machine learning (ML) workflows were trained and tested using synthetic datasets. These datasets consisted of 100 multicomponent shot gathers, generated using a section of the SEAM Foothills Phase II model whose topographic variation map shown in Figure 62. The acquisition geometry for each shot gather was consistent, with receiver lines placed along the x-axis from 500 to 5500 m, using an inter-receiver distance of 10 meters. The source was placed at x = 2000 m and z = 12 m. We produced 100 shot gathers by moving the acquisition geometry from y =500 to y =1500 in 10 m steps (Figure 62).

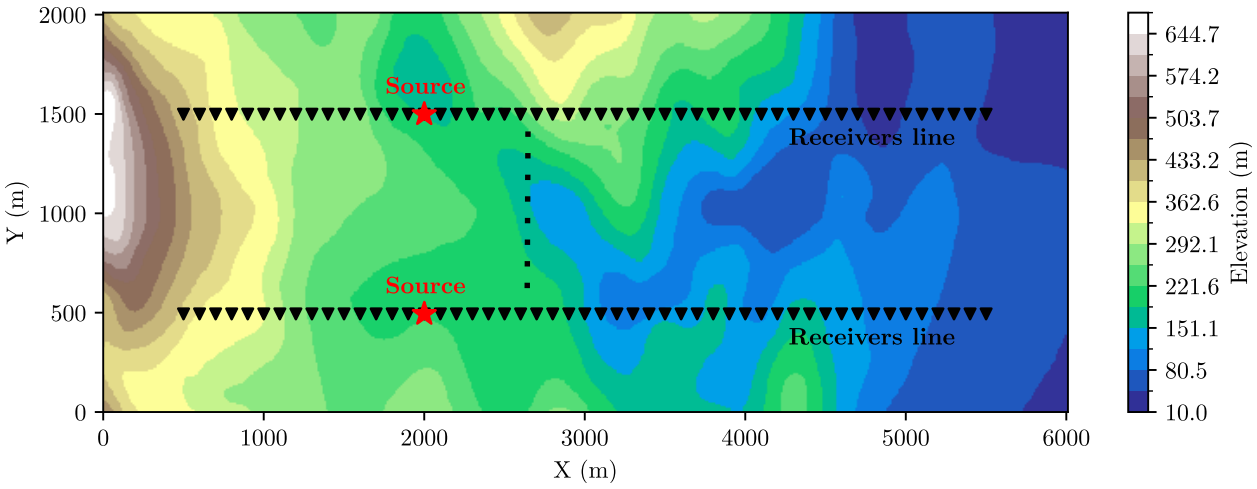

Figure 62. Elevation map and acquisition geometry for the portion of the SEAM model. The source is positioned at x =500 m, with a depth of 12 m. 3C receivers are aligned on the surface line from 500 to 5500 m with an inter-receiver spacing of 10 m. This acquisition geometry is repeated 100 times from y =500 to y =1500 with steps of 10 m.

Synthetic data were generated with and without NSS by applying the PDM, and these data were fed into the ML workflows. During processing, the spectra of elliptical elements were computed to produce the UNET model's inputs and labels. The inputs corresponded

to the (f, p) panels of the semi-major, semi-minor, and azimuth of the ascending node, each serving as a channel input. An example of the three channels for a specific shot gather is presented in Figure 63. Conversely, the labels for the (f, p) domain filter mask were produced using the power spectrum relation between data with and without NSS, as defined in equation (99).

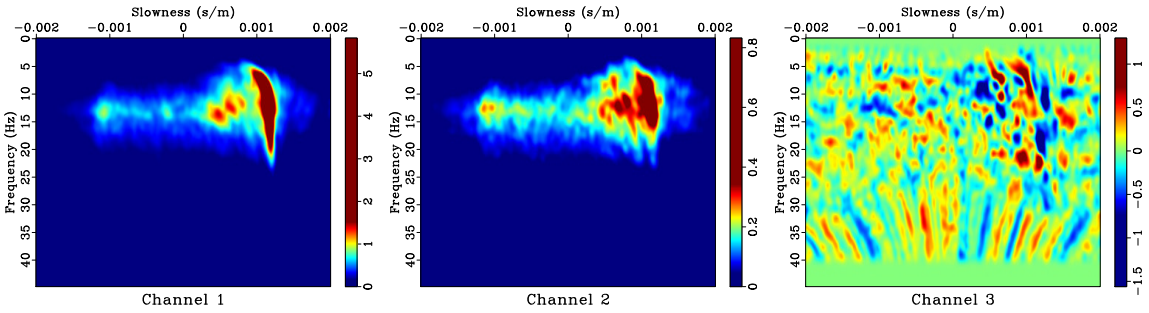

(a) (b) (c)

Figure 63. Input channels for UNET in the ML workflow in Figure 61. (a) Semi-major axis $a(p, f)$ as channel 1. (b) Semi-minor axis $b(p, f)$ as channel 2. (c) Longitude of ascending node $\Omega(p, f)$ channel 2.

The above-mentioned outputs and inputs served to train the ML workflow designed to predict the (f, p) domain filter mask. The training process utilized 80 % of the dataset, with the remaining 20 % used for validation. Figure 64 displays the UNET learning curve for both training and validation over 40 epochs. Notably, the Mean Square Error (MSE) for training decreased significantly during the initial epochs, demonstrating a knee effect between epochs 5 and 10. Similarly, the validation MSE experienced a decrease during the initial epochs, fluctuating within the same value range after 5 epochs.

Figure 65 illustrates an example of a predicted filter mask. The label for this example

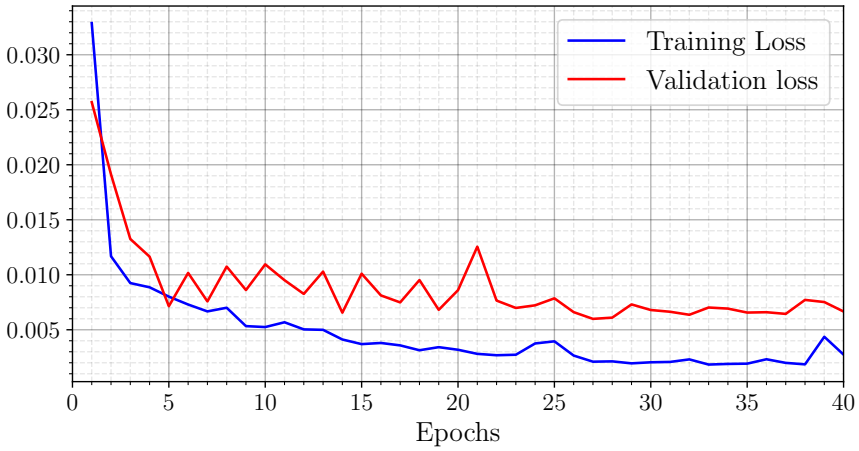

Figure 64. Training and validation loss using MSE for ML workflow in the (f, p) domain.

was generated using the shot gather associated with the total wavefield and deep wavefield, as shown in Figures 66(a) and 66(b), respectively. After the predicted filter mask was applied, most of the NSS was attenuated (see Figure 66(c)). However, the body-wave reflections remained weak. The application of the nested ML workflow enhanced the body-wave reflections, resulting in a greater visual similarity between the final output and the labeled deep wavefield (see Figure 66(d)), particularly for far offset.

5.7. Discussion and Conclusions

This study underscores the significant benefits of implementing ML workflows for attenuating NSS in 3C seismic data. In Chapter 4, the 3C-FSPF was developed as a polarization filter utilizing variable-parameter activation functions. However, the manual tuning of these functions is time-consuming and prone to human bias. Conversely, the proposed ML-based approach addresses these issues, offering a more efficient and objective method for the extraction of specific polarized energy.

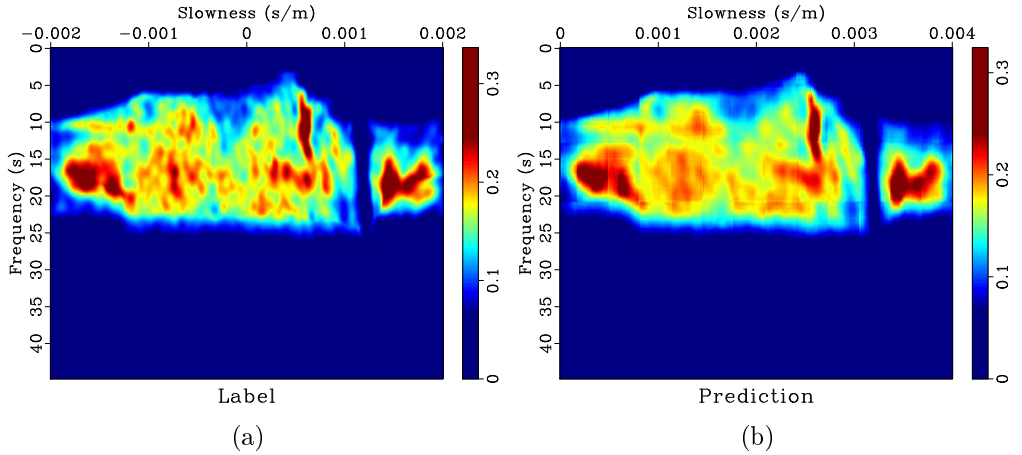

Figure 65. Polarization filter mask generation with ML workflow 1. (a) Label data for UNET training. (b) Predicted data by the trained UNET.

The numerical experiment with synthetic datasets showed that the UNET autoencoder, trained with the PDM generated data, can accurately predict filter masks in the (f, p) domain. The ML workflow also includes a second autoencoder, further refining the filtered 3C seismic data in the (t, h) domain, thus demonstrating the feasibility of this approach in reducing NSS noise and enhancing the quality of deeper reflections.

The ML workflows showed significant noise attenuation, thus enhancing the signal quality of the deeper reflections. This reveals the robustness of ML algorithms in processing 3C seismic data and their potential to identify NSS patterns. However, it's important to note that the current study is based on synthetic datasets modeled using the SEAM Foothills Phase II model and the finite-difference method solver (PMFD3D-GPU). We only used shot gathers generated from the SEAM model for training, which limited the generalization capability of the model for real data applications. Thus, while the initial results are encouraging,

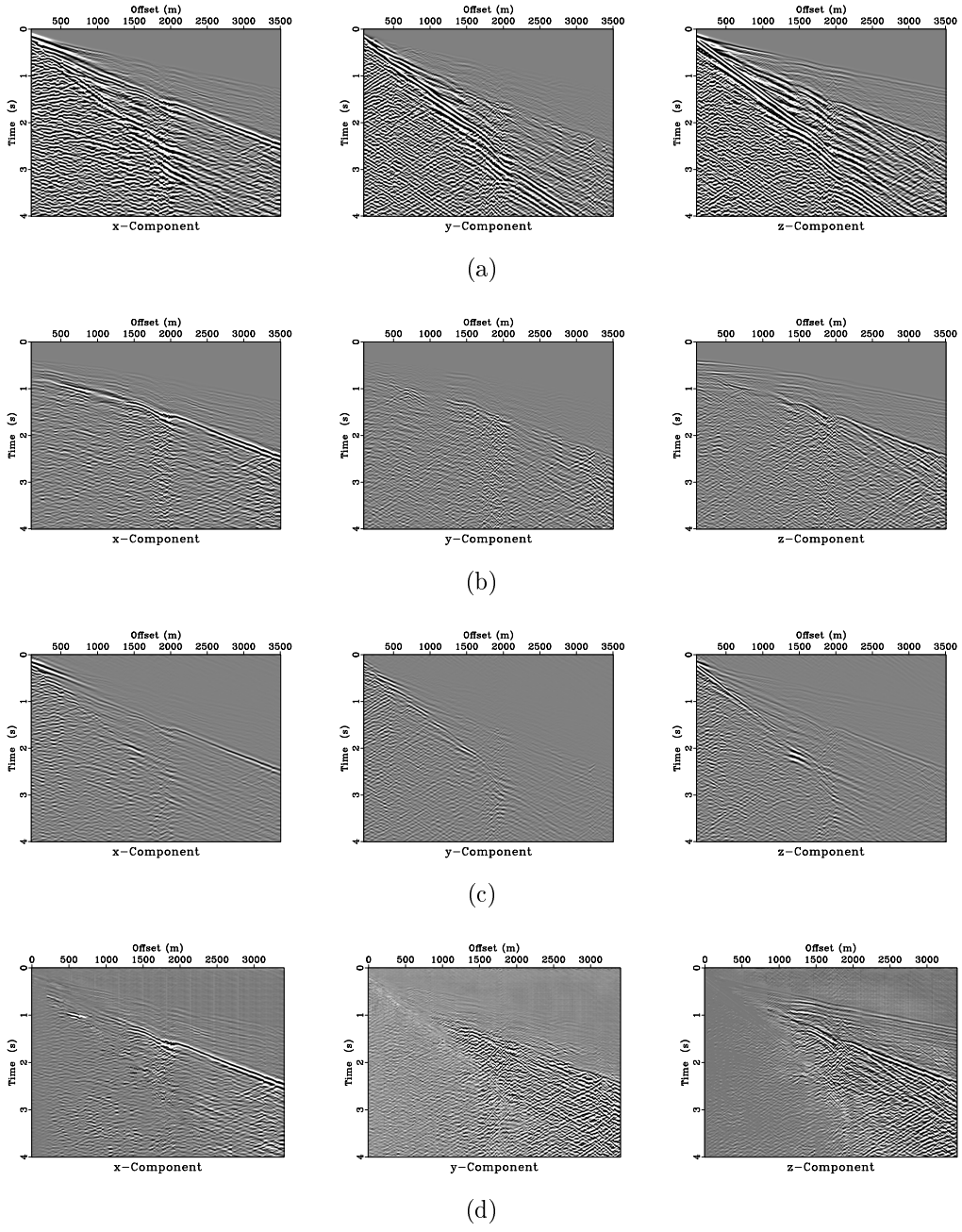

Figure 66. Multicomponent shot gather inputs and outputs in machine learning workflows. (a) Input data exhibiting total wavefield, which comprises reflections, surface waves, and NSS. (b) Labeled deep wavefield data including reflections but devoid of surface waves and most of NSS. (c) Data filtered by ML workflow in Figure 60. (d) Data filtered and refined by nested ML workflow in Figure 61.

further validation using real-world data is recommended. Incorporating a broader range of training datasets may prevent model overfitting, and provide insights into the performance of the ML workflows under various geological settings and noise conditions.

In conclusion, this study presented ML workflows as a promising new approach for attenuating NSS noise in 3C seismic data, offering substantial improvements over manual tunning approaches. While further research is needed to validate and optimize these workflows, the current results suggest a significant step forward in enhancing the quality and interpretability of 3C seismic data.

CHAPTER 6. Conclusions and future work

This doctoral thesis has investigated methods to improve the quality of seismic images contaminated with near-surface scattering noise. The research has been guided by a principal question: How can the quality of seismic images be improved when data are contaminated with near-surface scattering noise? To answer this question, three objectives were addressed:

Objective 1, aimed at modeling 3D elastic wave propagation numerically in complex near-surface models to generate synthetic seismic data with realistic scattering, was addressed in Chapters 1, 2, and 3.

In Chapter 1, an approach to reproducing the complex ground roll energy cone seen in synthetic seismic data on mountainous onshore areas was presented. It was found that scattering energy is more pronounced for higher impedance contrasts and when the size of the heterogeneity is near the Rayleigh wavelength. Therefore, the inclusion of a low-velocity layer and small-scale distributed heterogeneities in the near-surface of the SEAM model is essential for producing synthetic data that can realistically mimic scattered surface wave energy. Future work may involve refining the modeling process with different ACFs of the near-surface heterogeneities to achieve more realistic data and examining the impact on the scattering energy.

Chapter 2 presented PMFD3D-GPU, a finite-difference solver for 3D elastic wave modeling in heterogeneous models with irregular topography. The solver demonstrated improved computational efficiency and generated realistic seismic synthetic data. However,

potential improvements exist in applying Perfectly Matched Layers (PMLs) to improve the Absorbing Boundary Conditions (ABCs) and utilizing a shared memory strategy to further reduce computational execution time. The extension of the GPU implementation strategy to finite-difference method (FDM) solvers designed for curved domains is suggested as a future research direction, potentially enhancing accuracy while reducing execution time since require fewer points per wavelength than rectangular domains (de la Puente et al., 2014).

Chapter 3 introduced the Partitioned Domain Method (PDM) for modeling Near-Surface Scattering (NSS) in complex overburden scenarios. Despite its limitations, including incomplete isolation of NSS and the requirement for manual calibration of the domain partition, the PDM generates valuable synthetic wavefields. Future research should focus on enhancing the PDM, addressing its limitations, and expanding its applicability in the field of near-surface scattering modeling.

Objectives 2 and 3, which involved designing a workflow based on polarization filtering and machine learning to remove scattering noise from multicomponent seismic shot gathers and evaluating the performance of this workflow on synthetic and real seismic data, were addressed in Chapters 4 and 5.

Chapter 4 introduced a novel two-step polarization method for discriminating and separating wave-types in under-sampled 3C seismic data. This method was validated on both synthetic and real data, demonstrating its potential to enhance the quality of seismic data, particularly those acquired in complex land regions. For future research, it is proposed to broaden the application of this method across diverse geological contexts. Moreover, inte-

grating machine learning algorithms could enhance the design of the mask filter, providing an adaptive, data-driven approach.

Chapter 5 presented machine learning workflows, particularly autoencoders, as a promising new approach for attenuating NSS noise in 3C seismic data. These ML workflows have shown substantial improvements over manual tuning approaches. In Chapter 5, full real data application was not included because machine learning workflows require a diverse range of data to prevent overfitting and to ensure the trained model can generalize to real-world scenarios. Unfortunately, the experiments were constrained by the availability of training data. We only used shot gathers generated from the SEAM model for training, which limited the model's generalization capability for real data applications. Future work should focus on refining these ML workflows, validating them on a wider range of datasets, and integrating them into the broader seismic data processing pipeline to provide end-to-end improvement of the data quality.

In conclusion, the thesis has made significant strides in improving the quality of seismic images contaminated with near-surface scattering noise. It presents promising advancements in the modeling and processing of near-surface seismic scattering, and provides a robust foundation for future work. The next steps include the continuous refinement of these methods, aiming to overcome current limitations and expand their applicability, with the ultimate goal of integrating these advances into land seismic data processing workflows.

References

Abdelkhalek, R., Calandra, H., Coulaud, O., Roman, J., and Latu, G. (2009). Fast seismic modeling and reverse time migration on a gpu cluster. In *2009 International Conference on High Performance Computing & Simulation*, pages 36–43. IEEE.

Afanasiev, M., Boehm, C., van Driel, M., Krischer, L., Rietmann, M., May, D. A., Knepley, M. G., and Fichtner, A. (2019). Modular and flexible spectral-element waveform modelling in two and three dimensions. *Geophysical Journal International*, 216(3):1675–1692.

Aki, K. and Chouet, B. (1975). Origin of coda waves: source, attenuation, and scattering effects. *Journal of geophysical research*, 80(23):3322–3342.

Al-Hasanat, A., Mesleh, A., Krishan, M., Sharadqh, A., Al-Qaisi, A., Woo, W. L., and Dlay, S. S. (2017). Blind separation of multicomponent seismic wavefield using svd of reduced dimension spectral matrix. *Journal of King Saud University-Computer and Information Sciences*, 29(1):39–53.

Alkhimenkov, Y., Räss, L., Khakimova, L., Quintal, B., and Podladchikov, Y. (2021). Resolving wave propagation in anisotropic poroelastic media using graphical processing units (gpus). *Journal of Geophysical Research: Solid Earth*, page e2020JB021175.

Almuhaidib, A. M. and Toksöz, M. N. (2014). Numerical modeling of elastic-wave scattering by near-surface heterogeneities. *Geophysics*, 79(4):T199–T217.

Alzubaidi, L., Zhang, J., Humaidi, A. J., Al-Dujaili, A., Duan, Y., Al-Shamma, O., Santamaría, J., Fadhel, M. A., Al-Amidie, M., and Farhan, L. (2021). Review of deep learning: Concepts, cnn architectures, challenges, applications, future directions. *Journal of big Data*, 8:1–74.

An, Y., Guo, J., Ye, Q., Childs, C., Walsh, J., and Dong, R. (2021). Deep convolutional neural network for automatic fault recognition from 3d seismic datasets. *Computers & Geosciences*, 153:104776.

Bale, R., Marchand, T., Wilkinson, K., Wikel, K., and Kendall, R. (2013). The signature of shear-wave splitting: Theory and observations on heavy oil data. *The Leading Edge*, 32(1):14–24.

Bathe, K.-J. (2006). *Finite element procedures*. Klaus-Jurgen Bathe.

Berenger, J.-P. (1994). A perfectly matched layer for the absorption of electromagnetic waves. *Journal of computational physics*, 114(2):185–200.

Beylkin, G. and Burridge, R. (1990). Linearized inverse scattering problems in acoustics and elasticity. *Wave motion*, 12(1):15–52.

Birch, F. (1961). The velocity of compressional waves in rocks to 10 kilobars: 2. *Journal of Geophysical Research*, 66(7):2199–2224.

Blonk, B. and Herman, G. C. (1994). Inverse scattering of surface waves; a new look at surface consistency. *Geophysics*, 59(6):963–972.

Bohlen, T. and Saenger, E. H. (2006). Accuracy of heterogeneous staggered-grid finite-difference modeling of Rayleigh waves. *Geophysics*, 71(4):T109–T115.

Breuer, A., Heinecke, A., and Bader, M. (2016). Petascale local time stepping for the ader-dg finite element method. In *2016 IEEE international parallel and distributed processing symposium (IPDPS)*, pages 854–863. IEEE.

Campman, X. and Dwi Riyanti, C. (2007). Non-linear inversion of scattered seismic surface waves. *Geophysical Journal International*, 171(3):1118–1125.

Cao, J. and Chen, J.-B. (2018). A parameter-modified method for implementing surface topography in elastic-wave finite-difference modeling. *Geophysics*, 83(6):T313–T332.

Capdeville, Y., Gung, Y., and Romanowicz, B. (2005). Towards global earth tomography using the spectral element method: a technique based on source stacking. *Geophysical Journal International*, 162(2):541–554.

Cerjan, C., Kosloff, D., Kosloff, R., and Reshef, M. (1985). A nonreflecting boundary condition for discrete acoustic and elastic wave equations. *Geophysics*, 50(4):705–708.

Chen, Y. and Schuster, G. T. (2020). Seismic inversion by newtonian machine learning. *Geophysics*, 85(4):WA185–WA200.

Cheng, J., Grossman, M., and McKercher, T. (2014). *Professional CUDA c programming*. John Wiley & Sons.

Christoffersson, A., Husebye, E., and Ingate, S. (1988). Wavefield decomposition using ml-probabilities in modelling single-site 3-component records. *Geophysical Journal International*, 93(2):197–213.

Clayton, R. and Engquist, B. (1977). Absorbing boundary conditions for acoustic and elastic wave equations. *Bulletin of the seismological society of America*, 67(6):1529–1540.

Collino, F. and Tsogka, C. (2001). Application of the perfectly matched absorbing layer model to the linear elastodynamic problem in anisotropic heterogeneous media. *Geophysics*, 66(1):294–307.

De Franco, R. y Musacchio, G. (2001). Polarization filter with singular value decomposition. *Geophysics*, 66:932–938.

de la Puente, J., Ferrer, M., Hanzich, M., Castillo, J. E., and Cela, J. M. (2014). Mimetic seismic wave modeling including topography on deformed staggered grids. *Geophysics*, 79(3):T125–T141.

De Meersman, K. (2008). Ground roll polarization filtering with spatial smoothness constraints. In *2008 SEG Annual Meeting*. Society of Exploration Geophysicists.

de Meersman, K. and Kendall, R. (2005). A complex svd-polarization filter for ground roll attenuation on multi-component data. In *67th EAGE Conference & Exhibition*.

Diallo, M., Kulesh, M., Holschneider, M., and Scherbaum, F. (2005). Instantaneous pola-

rization attributes in the time–frequency domain and wavefield separation. *Geophysical Prospecting*, 53(5):723–731.

Diallo, M. S., Kulesh, M., Holschneider, M., Kurennaya, K., and Scherbaum, F. (2006a). Instantaneous polarization attributes based on an adaptive approximate covariance method. *Geophysics*, 71(5):V99–V104.

Diallo, M. S., Kulesh, M., Holschneider, M., Scherbaum, F., and Adler, F. (2006b). Characterization of polarization attributes of seismic waves using continuous wavelet transforms. *Geophysics*, 71(3):V67–V77.

Du, Z., Foulger, G. R., and Mao, W. (2000). Noise reduction for broad-band, three-component seismograms using data-adaptive polarization filters. *Geophysical Journal International*, 141(3):820–828.

Dumbser, M. and Käser, M. (2006). An arbitrary high-order discontinuous galerkin method for elastic waves on unstructured meshes-ii. the three-dimensional isotropic case. *Geophysical Journal International*, 167(1):319–336.

Durran, D. R. (2013). *Numerical methods for wave equations in geophysical fluid dynamics*, volume 32. Springer Science & Business Media.

Engquist, B. and Majda, A. (1977). Absorbing boundary conditions for numerical simulation of waves. *Proceedings of the National Academy of Sciences*, 74(5):1765–1766.

Fabien-Ouellet, G., Gloaguen, E., and Giroux, B. (2017). Time-domain seismic modeling in viscoelastic media for full waveform inversion on heterogeneous computing platforms with opencl. *Computers & Geosciences*, 100:142–155.

Filnn, E. A. (1965). Signal analysis using rectilinearity and direction of particle. In *Proceedings of the IEEE*, number 53, pages 1874–1876, 10.1109/PROC.1965.4462.

Géron, A. (2022). *Hands-on machine learning with Scikit-Learn, Keras, and TensorFlow*. .°'Reilly Media, Inc.".

Geuzaine, C. and Remacle, J.-F. (2009). Gmsh: A 3-d finite element mesh generator with built-in pre-and post-processing facilities. *International journal for numerical methods in engineering*, 79(11):1309–1331.

Hayashi, K., Burns, D. R., and TokosÌˆz, M. N. (2001). Discontinuous-grid finite-difference seismic modeling including surface topography. *Bulletin of the Seismological Society of America*, 91(6):1750–1764.

Hestholm, S. and Ruud, B. (1998). 3-d finite-difference elastic wave modeling including surface topography. *Geophysics*, 63(2):613–622.

Hobiger, M., Cornou, C., Bard, P.-Y., and Le Bihan, N. (2011). Musique: A quaternion-based array processing technique for surface wave polarization analysis. In *2011 IEEE Statistical Signal Processing Workshop (SSP)*, pages 5–8. IEEE.

Hobiger, M., Le Bihan, N., Cornou, C., and Bard, P.-Y. (2012). Multicomponent signal processing for rayleigh wave ellipticity estimation: application to seismic hazard assessment. *IEEE Signal Processing Magazine*, 29(3):29–39.

Hu, L., Zheng, X., Duan, Y., Yan, X., Hu, Y., and Zhang, X. (2019). First-arrival picking with a u-net convolutional network. *Geophysics*, 84(6):U45–U57.

Hu, Y., Wang, L., Cheng, F., Luo, Y., Shen, C., and Mi, B. (2016). Ground-roll noise extraction and suppression using high-resolution linear radon transform. *Journal of Applied Geophysics*, 128:8–17.

Hudson, J. (1967). Scattered surface waves from a surface obstacle. *Geophysical Journal International*, 13(4):441–458.

Hughes, T. J. (2012). *The finite element method: linear static and dynamic finite element analysis*. Courier Corporation.

Irving, J., Scholer, M., and Holliger, K. (2010). Inversion for the stochastic structure of subsurface velocity heterogeneity from surface-based geophysical reflection images. *Advances in Near-Surface Seismology and Ground-Penetrating Radar*.

Jackson, G. M., Mason, I. M., and Greenhalgh, S. A. (1991). Principal component transforms of triaxial recordings by singular value decomposition. *Geophysics*, 56:528–533.

Jin, S. and Ronen, S. (2005). Ground roll detection and attenuation by 3C polarization analysis. In *67th EAGE Conference & Exhibition*.

Jurkevics, A. (1988). Polarization analysis of three-component array data. *Bulletin of the Seismological Society of America*, 78(5):1725–1743.

Käser, M. and Dumbser, M. (2006). An arbitrary high-order discontinuous galerkin method for elastic waves on unstructured meshes i. the two dimensional isotropic case with external source terms. *Geophysical Journal International*, 166(2):855–877.

Käser, M., Dumbser, M., De La Puente, J., and Igel, H. (2007). An arbitrary high-order discontinuous galerkin method for elastic waves on unstructured meshes-iii. viscoelastic attenuation. *Geophysical Journal International*, 168(1):224–242.

Kazemnia Kakhki, M., Mansur, W. J., and Peters, F. C. (2020). Rayleigh wave separation using high-resolution time-frequency polarization filter. *Geophysical Prospecting*, 68(7):2104–2118.

Kendall, R., Jin, S., Ronen, S., and De Meersman, K. (2005a). An svd-polarization filter for ground roll attenuation on multicomponent data. In *EAGE/SEG Research Workshop-Multicomponent Seismic-Past, Present and Future.*

Kendall, R., Jin, S., Ronen, S., and De Meersman, K. (2005b). An svd-polarization filter for ground roll attenuation on multicomponent data. In *SEG Technical Program Expanded Abstracts 2005*, pages 928–931. Society of Exploration Geophysicists.

Komatitsch, D., Erlebacher, G., Göddeke, D., and Michéa, D. (2010). High-order finite-

element seismic wave propagation modeling with mpi on a large gpu cluster. *Journal of computational physics*, 229(20):7692–7714.

Komatitsch, D. and Martin, R. (2007). An unsplit convolutional perfectly matched layer improved at grazing incidence for the seismic wave equation. *Geophysics*, 72(5):SM155–SM167.

Komatitsch, D. and Tromp, J. (1999). Introduction to the spectral element method for three-dimensional seismic wave propagation. *Geophysical journal international*, 139(3):806–822.

Komatitsch, D. and Tromp, J. (2002). Spectral-element simulations of global seismic wave propagation-i. validation. *Geophysical Journal International*, 149(2):390–412.

Komatitsch, D., Vilotte, J.-P., Vai, R., Castillo-Covarrubias, J. M., and SÃ¡nchez-Sesma, F. J. (1999). The spectral element method for elastic wave equations-application to 2-d and 3-d seismic problems. *International Journal for numerical methods in engineering*, 45(9):1139–1164.

Kulesh, M., Diallo, M. S., Holschneider, M., Kurennaya, K., KrÃ¼ger, F., Ohrnberger, M., and Scherbaum, F. (2007). Polarization analysis in the wavelet domain based on the adaptive covariance method. *Geophysical Journal International*, 170(2):667–678.

Le Bihan, N. and Mars, J. (2004). Singular value decomposition of quaternion matrices: a new tool for vector-sensor signal processing. *Signal processing*, 84(7):1177–1199.

Le Bihan, N., Sangwine, S. J., and Ell, T. A. (2014). Instantaneous frequency and amplitude of orthocomplex modulated signals based on quaternion fourier transform. *Signal Processing*, 94:308–318.

Levander, A. R. (1988). Fourth-order finite-difference P-SV seismograms. *Geophysics*, 53(11):1425–1436.

LeVeque, R. J. (2007). *Finite difference methods for ordinary and partial differential equations: steady-state and time-dependent problems*. SIAM.

Lines, L. R., Slawinski, R., and Bording, R. P. (1999). A recipe for stability of finite-difference wave-equation computations. *Geophysics*, 64(3):967–969.

Liu, J., Zeng, X., Xia, J., and Mao, M. (2012). The separation of p-and s-wave components from three-component crosswell seismic data. *Journal of applied geophysics*, 82:163–170.

Liu, X., Chen, J., Lan, H., and Zhao, Z. (2018). Seismic wavefield simulation with irregular surface topography and graphic processing unit (gpu) implementation. *Journal of Seismic Exploration*, 27:445–472.

Lu, J., Wang, Y., and Yang, C.-Y. (2010). Instantaneous polarization filtering focused on suppression of surface waves. *Applied Geophysics*, 7(1):88–97.

Luo, Y., Xia, J., Liu, J., Liu, Q., and Xu, S. (2007). Joint inversion of high-frequency surface waves with fundamental and higher modes. *Journal of Applied Geophysics*, 62(4):375–384.

Luo, Y., Xia, J., Miller, R. D., Xu, Y., Liu, J., and Liu, Q. (2008). Rayleigh-wave dispersive energy imaging using a high-resolution linear radon transform. *Pure and Applied Geophysics*, 165(5):903–922.

Luo, Y., Xia, J., Miller, R. D., Xu, Y., Liu, J., and Liu, Q. (2009a). Rayleigh-wave mode separation by high-resolution linear radon transform. *Geophysical Journal International*, 179(1):254–264.

Luo, Y., Xia, J., Miller, R. D., Xu, Y., Liu, J., and Liu, Q. (2009b). Rayleigh-wave mode separation by high-resolution linear radon transform. *Geophysical Journal International*, 179(1):254–264.

Maeda, T., Sato, H., and Nishimura, T. (2008). Synthesis of coda wave envelopes in randomly inhomogeneous elastic media in a half-space: single scattering model including rayleigh waves. *Geophysical Journal International*, 172(1):130–154.

Mandelli, S., Borra, F., Lipari, V., Bestagini, P., Sarti, A., and Tubaro, S. (2018). Seismic data interpolation through convolutional autoencoder. In *SEG Technical Program Expanded Abstracts 2018*, pages 4101–4105. Society of Exploration Geophysicists.

Martin, R., Komatitsch, D., Blitz, C., and Le Goff, N. (2008). Simulation of seismic wave propagation in an asteroid based upon an unstructured mpi spectral-element method: blocking and non-blocking communication strategies. In *High Performance Computing for*

Computational Science-VECPAR 2008: 8th International Conference, Toulouse, France, June 24-27, 2008. Revised Selected Papers 8, pages 350–363. Springer.

Martin, R., Komatitsch, D., Gedney, S. D., and Bruthiaux, E. (2010). A high-order time and space formulation of the unsplit perfectly matched layer for the seismic wave equation using Auxiliary Differential Equations (ADE-PML). *Computer Modeling in Engineering and Sciences*, 56(1):17–42.

Michéa, D. and Komatitsch, D. (2010). Accelerating a three-dimensional finite-difference wave propagation code using gpu graphics cards. *Geophysical Journal International*, 182(1):389–402.

Micikevicius, P. (2009). 3d finite difference computation on gpus using cuda. In *Proceedings of 2nd workshop on general purpose processing on graphics processing units*, pages 79–84.

Mittet, R. (2002). Free-surface boundary conditions for elastic staggered-grid modeling schemes. *Geophysics*, 67(5):1616–1623.

Moczo, P., Kristek, J., and GÃ¡lis, M. (2014). *The finite-difference modelling of earthquake motions: Waves and ruptures*. Cambridge University Press.

Moczo, P., Kristek, J., Vavryčuk, V., Archuleta, R. J., and Halada, L. (2002). 3d heterogeneous staggered-grid finite-difference modeling of seismic motion with volume harmonic and arithmetic averaging of elastic moduli and densities. *Bulletin of the Seismological Society of America*, 92(8):3042–3066.

Monk, P. and Richter, G. R. (2005). A discontinuous galerkin method for linear symmetric hyperbolic systems in inhomogeneous media. *Journal of Scientific Computing*, 22(1):443–477.

Montalbetti, J. F. and Kanasewich, E. R. (1970). Enhancement of teleseismic body phases with a polarization filter. *Geophysical Journal International*, 21(2):119–129.

Morozov, I. B. and Smithson, S. B. (1996). Instantaneous polarization attributes and directional filtering. *Geophysics*, 61(3):872–881.

Murray, C. D. and Dermott, S. F. (1999). *Solar system dynamics*. Cambridge university press.

Nakata, N., Tsuji, T., and Matsuoka, T. (2011). Acceleration of computation speed for elastic wave simulation using a graphic processing unit. *Exploration Geophysics*, 42(1):98–104.

Nasr, M., Giroux, B., and Dupuis, J. C. (2021). A novel time-domain polarization filter based on a correlation matrix analysis. *Geophysics*, 86(2):V91–V106.

Oristaglio, M. (2013). Seam update: Seam phase ii: The foothills model-seismic exploration in mountainous regions. *The Leading Edge*, 32(9):1020–1024.

Páez, A., Sánchez, I., and Ramírez, A. (2020). Computational strategies for implementation of 2d elastic wave modeling in gpu. *Entre Ciencia e Ingeniería*, 14(28):52–58.

Paulus, C., Mars, J., and Gounon, P. (2005). Wideband spectral matrix filtering for multi-component sensors array. *Signal processing*, 85(9):1723–1743.

Paulus, C. and Mars, J. I. (2006). New multicomponent filters for geophysical data processing. *IEEE transactions on geoscience and remote sensing*, 44(8):2260–2270.

Perelberg, A. I. and Hornbostel, S. C. (1994). Applications of seismic polarization analysis. *Geophysics*, 59(1):119–130.

Peter, D., Komatitsch, D., Luo, Y., Martin, R., Le Goff, N., Casarotti, E., Le Loher, P., Magnoni, F., Liu, Q., Blitz, C., et al. (2011). Forward and adjoint simulations of seismic wave propagation on fully unstructured hexahedral meshes. *Geophysical Journal International*, 186(2):721–739.

Pinnegar, C. (2006). Polarization analysis and polarization filtering of three component signals with the time-frequency S transform. *Geophysical Journal International*, 165(2):596–606.

Puzyrev, V. and Elders, C. (2022). Unsupervised seismic facies classification using deep convolutional autoencoder. *Geophysics*, 87(4):1–39.

Regone, C., Stefani, J., Wang, P., Gerea, C., Gonzalez, G., and Oristaglio, M. (2017). Geologic model building in seam phase ii-land seismic challenges. *The Leading Edge*, 36(9):738–749.

Rene, R., Fitter, J., Forsyth, P., Kim, K., Murray, D., Walters, J., and Westerman, J. (1986). Multicomponent seismic studies using complex trace analysis. *Geophysics*, 51(6):1235–1251.

Ricker, N. (1953). The form and laws of propagation of seismic wavelets. *Geophysics*, 18(1):10–40.

Riyanti, C. D. and Herman, G. C. (2005). Three-dimensional elastic scattering by near-surface heterogeneities. *Geophysical Journal International*, 160(2):609–620.

Robertsson, J. O. (1996). A numerical free-surface condition for elastic/viscoelastic finite-difference modeling in the presence of topography. *Geophysics*, 61(6):1921–1934.

Robertsson, J. O. and Chapman, C. H. (2000). An efficient method for calculating finite-difference seismograms after model alterations. *Geophysics*, 65(3):907–918.

Ronneberger, O., Fischer, P., and Brox, T. (2015). U-net: Convolutional networks for biomedical image segmentation. In *International Conference on Medical image computing and computer-assisted intervention*, pages 234–241. Springer.

Roueff, A., Chanussot, J., and Mars, J. I. (2006). Estimation of polarization parameters using time-frequency representations and its application to waves separation. *Signal Processing*, 86(12):3714–3731. Special Section: Multimodal Human-Computer Interfaces.

Rubio, F., Hanzich, M., Farrés, A., de la Puente, J., and Cela, J. M. (2014). Finite-difference

staggered grids in gpus for anisotropic elastic wave propagation simulation. *Computers & geosciences*, 70:181–189.

Russell, B. (2019). Machine learning and geophysical inversionâ€"a numerical study. *The Leading Edge*, 38(7):512–519.

Sajeva, A. and Menanno, G. (2017). Characterisation and extraction of a rayleigh-wave mode in vertically heterogeneous media using quaternion svd. *Signal Processing*, 136:43–58.

Samson, J. (1977). Matrix and stokes vector representations of detectors for polarized waveforms: theory, with some applications to teleseismic waves. *Geophysical Journal International*, 51(3):583–603.

Samson, J. and Olson, J. (1981). Data-adaptive polarization filters for multichannel geophysical data. *Geophysics*, 46(10):1423–1431.

Sánchez-Galvis, I., Villa, Y., Duarte, C., Sierra, D., and Agudelo, W. (2017). Seismic attribute selection and clustering to detect and classify surface waves in multicomponent seismic data by using k-means algorithm. *The Leading Edge*, 36(3):23–248.

Sánchez-Galvis, I. J., Serrano, J., Sierra, D. A., and Agudelo, W. (2021). Simulation of scattered seismic surface waves on mountainous onshore areas: Understanding the "ground roll energy cone". *The Leading Edge*, 40(8):601–609.

Sánchez-Galvis, I.-J., Serrano-Luna, J.-O., Niño-Niño, C.-A., Sierra, D.-A., and Agudelo-

Zambrano, W.-M. (2016). Svd polarization filter taking into account the planarity of ground roll energy. *CT&F-Ciencia, Tecnología y Futuro*, 6(3):5–24.

Sato, H., Fehler, M. C., and Maeda, T. (2012). *Seismic wave propagation and scattering in the heterogeneous earth*. Springer Science and Business Media.

Sharif Razavian, A., Azizpour, H., Sullivan, J., and Carlsson, S. (2014). Cnn features off-the-shelf: an astounding baseline for recognition. In *Proceedings of the IEEE conference on computer vision and pattern recognition workshops*, pages 806–813.

Shearer, P. (2009). *Introduction to Seismology*. Cambridge University Press, second edition.

Sheriff, R. E. (2002). Encyclopedic dictionary of applied geophysics.

Snieder, R. (1986). 3-d linearized scattering of surface waves and a formalism for surface wave holography. *Geophysical Journal International*, 84(3):581–605.

Socco, L. and Strobbia, C. (2004). Surface-wave method for near-surface characterization: a tutorial. *Near Surface Geophysics*, 2(4):165–185.

Solano, C. P., Donno, D., and Chauris, H. (2016). Finite-difference strategy for elastic wave modelling on curved staggered grids. *Computational Geosciences*, 20(1):245–264.

Stork, C. (2020). How does the thin near surface of the earth produce 10–100 times more noise on land seismic data than on marine data? *First Break*, 38(8):67–75.

Sun, Y.-C., Ren, H., Zheng, X.-Z., Li, N., Zhang, W., Huang, Q., and Chen, X. (2019). 2-d poroelastic wave modelling with a topographic free surface by the curvilinear grid finite-difference method. *Geophysical Journal International*, 218(3):1961–1982.

Tan, Y.-Y., He, C., Wang, Y.-D., and Zhao, Z. (2013). Ground roll attenuation using a time frequency dependent polarization filter based on the S transform. *Applied Geophysics*, 10(3):279–294.

Tessmer, E. and Kosloff, D. (1994). 3-d elastic modeling with surface topography by a chebychev spectral method. *Geophysics*, 59(3):464–473.

Tiapkina, O., Landrø, M., Tyapkin, Y., and Link, B. (2012). Single-station SVD-based polarization filtering of ground roll: Perfection and investigation of limitations and pitfalls. *Geophysics*, 77(2):V41–V59.

Trad, D., Ulrych, T., and Sacchi, M. (2003). Latest views of the sparse radon transform. *Geophysics*, 68(1):386–399.

Trefethen, L. N. (1996). Finite difference and spectral methods for ordinary and partial differential equations.

Tsai, K. C., Hu, W., Wu, X., Chen, J., and Han, Z. (2019). Automatic first arrival picking via deep learning with human interactive learning. *IEEE Transactions on Geoscience and Remote Sensing*, 58(2):1380–1391.

Vidale, J. E. (1986). Complex polarization analysis of particle motion. *Bulletin of the Seismological society of America*, 76(5):1393–1405.

Virieux, J. (1986). P-SV wave propagation in heterogeneous media: Velocity-stress finite-difference method. *Geophysics*, 51(4):889–901.

Wang, C. and Wang, Y. (2017). Ground roll attenuation using polarization analysis in the tfk domain. *Geophysical Journal International*, 210(1):240–254.

Wang, Y., Wang, B., Tu, N., and Geng, J. (2020a). Seismic trace interpolation for irregularly spatial sampled data using convolutional autoencoder. *Geophysics*, 85(2):V119–V130.

Wang, Z., Li, B., Liu, N., Wu, B., and Zhu, X. (2020b). Distilling knowledge from an ensemble of convolutional neural networks for seismic fault detection. *IEEE Geoscience and Remote Sensing Letters*.

Weiss, R. M. and Shragge, J. (2013). Solving 3d anisotropic elastic wave equations on parallel gpu devices. *Geophysics*, 78(2):F7–F15.

Wrona, T., Pan, I., Gawthorpe, R. L., and Fossen, H. (2018). Seismic facies analysis using machine learning. *Geophysics*, 83(5):O83–O95.

Wu, R.-S. (1989). The perturbation method in elastic wave scattering. In *Scattering and Attenuation of Seismic Waves, Part II*, pages 605–637. Springer.

Wu, R.-S. and Aki, K. (1985). Scattering characteristics of elastic waves by an elastic heterogeneity. *Geophysics*, 50(4):582–595.

Wu, X., Liang, L., Shi, Y., and Fomel, S. (2019). Faultseg3d: Using synthetic data sets to train an end-to-end convolutional neural network for 3d seismic fault segmentation. *Geophysics*, 84(3):IM35–IM45.

Xia, J., Miller, R. D., and Park, C. B. (1999). Estimation of near-surface shear-wave velocity by inversion of rayleigh waves. *Geophysics*, 64(3):691–700.

Xia, K., Hilterman, F., and Hu, H. (2018). Unsupervised machine learning algorithm for detecting and outlining surface waves on seismic shot gathers. *Journal of Applied Geophysics*, 157:73–86.

Xu, Y., Xia, J., and Miller, R. D. (2007). Numerical investigation of implementation of air-earth boundary by acoustic-elastic boundary approach. *Geophysics*, 72(5):SM147–SM153.

Yang, P. (2014). A numerical tour of wave propagation. *Madagascar*, 2(4):1–34.

Yilmaz, O. (2001). *Seismic Data Analysis: Processing, Inversion, and Interpretation of Seismic Data*, volume 2. Society Exploration Geophysicists.

Yilmaz, Ö. (2015). *Engineering seismology with applications to geotechnical engineering*. Society of Exploration Geophysicists.

Zahradník, J. í., Moczo, P., and Hron, F. e. (1993). Testing four elastic finite-difference

schemes for behavior at discontinuities. *Bulletin of the Seismological Society of America*, 83(1):107–129.

Zeng, C., Xia, J., Miller, R. D., and Tsoflias, G. P. (2012). An improved vacuum formulation for 2d finite-difference modeling of rayleigh waves including surface topography and internal discontinuities. *Geophysics*, 77(1):T1–T9.

Zhao, T., Jayaram, V., Roy, A., and Marfurt, K. J. (2015). A comparison of classification techniques for seismic facies recognition. *Interpretation*, 3(4):SAE29–SAE58.

Zheng, Y., Zhang, Q., Yusifov, A., and Shi, Y. (2019). Applications of supervised deep learning for seismic interpretation and inversion. *The Leading Edge*, 38(7):526–533.

Appendices

APPENDIX A. Computation of the HRLRT

The computation of HRLRT is performed by applying Iterative Reweighed Least Square (IRLS) to solve equation (76). The method requires the iterative computation of weighted matrices for both residual vector $\mathbf{r} = \mathbf{d} - \mathbf{Lm}$ and model vector $\mathbf{m}$ as follows:

$$\operatorname{diag}(\mathbf{W}_r)_i = \begin{cases} |r_i|^{-1/2}, & |r_i| > \epsilon \\ \epsilon, & |r_i| \leq \epsilon \end{cases} \tag{A.1}$$

and

$$\operatorname{diag}(\mathbf{W}_m)_i = |m_i|^{1/2} \tag{A.2}$$

where ϵ is a damping parameter whose value corresponds to a small percentile of residual data. In this work we typically set ϵ as 2 percentile.

We utilized the CG method algorithm in A.1 for IRLS solution. The **condition 1** refers to the maximum external loop iterations or until the convergence tolerance while **condition 2** refers to the maximum iterations for inner loop. The functions where f($\mathbf{r}$) and g($\mathbf{m}$) represent the functions for matrix of diagonal weights of residual and model described in Equation (A.1) and Equation (A.2), respectively.

Algorithm A.1 CG method for IRLS solution

$\mathbf{m} \leftarrow \mathbf{L}^{\mathrm{H}}\mathbf{d}$
$\mathbf{r} \leftarrow \mathbf{d} - \mathbf{L}\mathbf{m}$
while condition 1 **do**
  $\mathrm{diag}(\mathbf{W}_r) \leftarrow \mathrm{f}(\mathbf{r})$
  $\mathrm{diag}(\mathbf{W}_m) \leftarrow \mathrm{g}(\mathbf{m})$
  $\mathbf{r} \leftarrow \mathbf{W}_r(\mathbf{d} - \mathbf{L}\mathbf{W}_m\mathbf{m})$
  $\boldsymbol{\Delta}\mathbf{m} \leftarrow \mathbf{W}_m^{\mathrm{H}}\mathbf{L}^{\mathrm{H}}\mathbf{W}_r^{\mathrm{H}}\mathbf{r}$
  $\boldsymbol{\Delta}\mathbf{s} \leftarrow \boldsymbol{\Delta}\mathbf{m}$
  $\gamma_1 \leftarrow \boldsymbol{\Delta}\mathbf{m}^{\mathrm{H}}\boldsymbol{\Delta}\mathbf{m}$
  while condition 2 **do**
    $\boldsymbol{\Delta}\mathbf{r} \leftarrow \mathbf{W}_r\mathbf{L}\mathbf{W}_m\boldsymbol{\Delta}\mathbf{m}$
    $\alpha \leftarrow \dfrac{(\boldsymbol{\Delta}\mathbf{s}^{\mathrm{H}}\boldsymbol{\Delta}\mathbf{m} + \boldsymbol{\Delta}\mathbf{m}^{\mathrm{H}}\boldsymbol{\Delta}\mathbf{s})}{2\boldsymbol{\Delta}\mathbf{r}^{\mathrm{H}}\boldsymbol{\Delta}\mathbf{r}}$
    $\mathbf{m} \leftarrow \mathbf{m} + \alpha\boldsymbol{\Delta}\mathbf{m}$
    $\mathbf{r} \leftarrow \mathbf{r} - \alpha\boldsymbol{\Delta}\mathbf{r}$
    $\boldsymbol{\Delta}\mathbf{m} \leftarrow \mathbf{W}_m^{\mathrm{H}}\mathbf{L}^{\mathrm{H}}\mathbf{W}_r^{\mathrm{H}}\mathbf{r}$
    $\gamma_2 \leftarrow \boldsymbol{\Delta}\mathbf{m}^{\mathrm{H}}\boldsymbol{\Delta}\mathbf{m}$
    $\beta \leftarrow \dfrac{\gamma_2}{\gamma_1}$
    $\boldsymbol{\Delta}\mathbf{s} \leftarrow \boldsymbol{\Delta}\mathbf{m} + \beta\boldsymbol{\Delta}\mathbf{s}$
    $\gamma_1 \leftarrow \gamma_2$
  end while
  $\mathbf{m} \leftarrow \mathbf{W}_m\mathbf{m}$
end while

APPENDIX B. Velocity $f-k$ filter

The $f-k$ velocity filter is designed to selectively pass or suppress signals that propagate at certain velocities, which are equivalently represented by specific dips or angles in the (f,k) domain (Yilmaz, 2001). In this domain, the dip of a signal correlates to its velocity. Therefore, slower propagating signals, such as the noise caused by ground roll, will manifest at higher dip angles due to their slower speed compared to the primary reflected seismic waves of interest.

The successful implementation of a velocity filter that suppresses the high-dip or slow-velocity signals can effectively reduce the ground roll in the seismic data. The (f,k) domain representation of the filtered data, denoted as $\hat{U}(f,k)$, is obtained by element-wise multiplication of the original transformed data $U(f,k)$ and the filter mask $M(f,k)$. The operation can be represented mathematically as:

$$\hat{U}(f,k) = M(f,k)U(f,k) \tag{B.1}$$

When applying the $f-k$ velocity filter, the filter mask $M(f,k)$ is typically designed around four key velocities that demarcate the zones of signal attenuation in the filter as follows:

$$M(f,k;v_1,v_2,v_3,v_4) = \begin{cases} 1-\sin\left(\frac{\pi}{2}\frac{(f/k-v_2)}{(v_1-v_2)}\right) & \text{if } v_1 < \left|\frac{f}{k}\right| < v_2 \\ 0 & \text{if } v_2 \leq \left|\frac{f}{k}\right| \leq v_3 \\ 1-\sin\left(\frac{\pi}{2}\frac{(f/k-v_3)}{(v_4-v_3)}\right) & \text{if } v_3 < \left|\frac{f}{k}\right| < v_4 \\ 1 & \text{otherwise} \end{cases} \tag{B.2}$$

where (v_1, v_2, v_3, v_4) are the parameters of the filters that specify the attenuation zone. The range between v_2 and v_3 is rejected, and the range below v_1 or above v_4 is preserved. To smoothly transition between regions of full signal suppression and full signal pass-through, sine taper functions are often employed. These functions help to create a gentle roll-off at the edges of the filter mask, which can prevent the introduction of artifacts in the filtered data.

Implementing an (f,k) Dip Filter involves the following steps:

Step 1: Apply a 2D Fourier Transform to the seismic data to convert it to the (f,k) domain.

Step 2: Design a filter mask in the (f,k) domain that suppresses or passes signals by setting the parameters as detailed in equation (B.2).

Step 3: Apply the filter to the data in the (f,k) domain (B.1).

Step 4: Apply an inverse 2D Fourier Transform to the filtered data, converting it back to the time-space domain.

The resulting data will have the desired signals enhanced and the undesired signals suppressed, improving the quality of subsequent seismic processing and interpretation.